UNIVERSITÀ DEGLI STUDI DI NAPOLI FEDERICO II

SCUOLA POLITECNICA E DELLE SCIENZE DI BASE

Dipartimento di Ingegneria Chimica, dei Materiali e
della Produzione Industriale

Dottorato di Ricerca in
“Ingegneria dei Prodotti e dei Processi Industriali”
XXXII ciclo

MODELLING AND EXPERIMENTAL CHARACTERIZATION OF UNSATURATED FLOW IN ABSORBENT AND SWELLING POROUS MEDIA

Supervisor:
Prof. Piero Salatino
Scientific Committee:
Ing. Ph.D. Roberto Solimene
Ing. Gilberto Aprea

Candidate:
Tommaso Santagata

ACKNOWLEDGMENTS

"If you want a happy ending, that depends, of course,
on where you stop your story."
Orson Welles

For the past three years, I have spent the most of my time asking questions, about almost everything. In this thesis, some of the answers are collected. In doing this, I have received many valuable helps from people to whom I am truly grateful.

First and foremost, I wish to show my gratitude to Prof. Piero Salatino, who initiated me as a Chemical Engineer and guided me along the way. His constant scientific support and his boundless trust in my possibilities have been a source of pride and a burden of responsibility, which I hope I managed to correspond. Secondly, I would thank Roberto for his daily help. His support was fundamental in making my speculations concrete and selecting the best ideas. Then, I am grateful to Gilberto and his team for his competence in experimental activities. His communication skills certainly facilitated the path of my PhD. I have been lucky and proud to have worked with them all.

Next, I wish to express my gratitude to Majid Hassanizadeh and Thomas Sweijen, who welcomed me into the Department of Earth Sciences of the Utrecht University in my second year of PhD. They have represented for me a shining example of dedication and humanity to follow. Thomas' doctoral Thesis was my ideal reference during the whole writing of mine. Their advice has accompanied me until the last version of the manuscript, and I am truly grateful.

Furthermore, I wish to thank the people of the National Research Council in Napoli, at via Metastasio. First among all, the unbreakable Antonio Cammarota, who has supported me in setting up most of the experimental procedures. Then, the "senior" researchers Antonio, Ernesto, Francesco, Giancarlo, Giovanna, Paola, Rino, who have shared with me their long experience. Finally, the "junior" researchers Carla, Claudio, Francesca, Giuseppe, Marco, Maurizio, with whom I enjoyed spending several coffee breaks.

In addition, I wish to express my gratitude and my love to my family, who supported me throughout my studies. Now at the end of my academic studies and my boyhood, I understand how lucky I have been to grow up in such a warm and open-minded home.

Finally, despite the perpetual turbulence in my affections, some friends have remained from my side. So, I wish to thank Andrea, Carlo, Cristina, Giacomo, Giovanni, Greta and Roberta for the advices and the time spent together.

Tommaso

INDEX

LIST OF SYMBOLS

ROMAN LETTERS

a, swelling rate parameter, LT^{-1}

a^{sl}, saturation-dependent fraction of the solid-liquid interface area, 1

$\bar{C}$, bulk concentration, ML^{-3}

D, constant diffusion coefficient, $\mathrm{L}^2\mathrm{T}^{-1}$

d, diameter of the sample, L

d^s, volumetric solid strain, 1

E, elastic modulus, $\mathrm{ML}^{-1}\mathrm{T}^{-2}$

$\boldsymbol{e} = -\frac{\boldsymbol{g}}{|\boldsymbol{g}|}$, gravitational unit vector, 1

$\boldsymbol{F}$, force, MLT^{-2}

G, shear modulus, $\mathrm{ML}^{-1}\mathrm{T}^{-2}$

$\boldsymbol{g}$, gravity vector, LT^{-2}

h, thickness of the sample, L

J^s, volume dilatation function, 1

$\boldsymbol{K}$, hydraulic conductivity tensor, LT^{-1}

K, scalar hydraulic conductivity, LT^{-1}

$\boldsymbol{k}$, permeability tensor, L^2

k_r, relative permeability, 1

k^n, contact stiffness in normal direction, $\mathrm{ML}^{-1/2}\mathrm{T}^{-2}$

k^t, contact stiffness in tangential direction, MT^2

L, size of the sample, L

L_i, size of the sample in the i dimension, L

l, size of SAP particles, L

m_2^s, SAP liquid uptake, 1

n, van Genuchten curve fitting parameter, 1

p, pressure, $\mathrm{ML}^{-1}\mathrm{T}^{-2}$

$\mathrm{PDF}(l)$, probability density function on size of SAP particles, 1

R, radius of a SAP particle, L

r, radial coordinate, L

r_t, swelling rate parameter, T^{-1}

$\mathrm{ramp}(t)$, ramp function in time, 1

s, saturation, 1

s_{FL}, interaction among fibres, 1

sgn, sign function, 1

$\mathrm{step(t)}$, step function in time, 1

t, time, T

$\boldsymbol{u}$, solid displacement vector, L

$\boldsymbol{v}$, velocity vector, LT^{-1}

v, scalar velocity, LT^{-1}

W, weight of the sample, M

$\boldsymbol{X}$, Lagrangian spatial coordinates, L

$\boldsymbol{x}$, Eulerian spatial coordinates, L

z, elevation, L

GREEK LETTERS

α, van Genuchten curve fitting parameter, L^{-1}

β, elastic parameter, $\mathrm{ML}^{-1}\mathrm{T}^{-2}$

$\boldsymbol{\Delta F}$, force variation, MLT^{-2}

Δt, time interval, T

ΔW, weight loss, M

$\Delta\psi^{l}$, pressure head loss, L

δ, exponential fitting parameter, 1

δ^{n}, normal displacement in contact between particles, L

ε, porosity, 1

η, void fraction of granular pack, 1

θ, absorption capacity of SAP, 1

λ_{d}, numerical damping factor, 1

μ, dynamic viscosity, $\mathrm{ML}^{-1}\mathrm{T}^{-1}$

ν, Poisson ratio, 1

ξ, correlation length, L

ρ, density, ML^{-3}

$\pi \approx 3.14$, mathematical constant, 1

Σ, conductivity, LT^{-1}

τ, characteristic reaction time, T

ϕ, hydraulic head, L

ϕ_{fr}, internal friction angle

ψ^l, pressure head of liquid phase, L

Ω^s, control space of porous solid domain, L^3

$\boldsymbol{\nabla}$, nabla (vector) operator (=grad), L^{-1}

SUBSCRIPTS

abs, SAP absorbed liquid

$bound$, boundary

c, capillarity

d, drainage

e, effective or equilibrium

eq, equivalent

f, relative to the cellulose fibre

FL, fluff component

i, spatial dimension indicator, index of summation addend, step of an experimental procedure or particle indicator

j, particle indicator

max, maximum available value for the referring quantity

min, minimum available value for the referring quantity

r, relative

SAP, SAP component

t, current time in a formula or in an experimental procedure

w, wetting

x, x-dimension

y, y-dimension

0, reference, initial or dry

1,2,3, model parameter indexes or measured quantities indexes of an experimental procedure

SUPERSCRIPTS

g, gas phase

l, liquid phase

s, solid phase

α, phase indicator

ν, power-law exponent, 1

°, current timestep

$-$, previous timestep

ABBREVIATION

AHP, absorbent hygiene product

ALE, Arbitrary Lagrangian-Eulerian

acq, acquisition

CFD, computational fluid dynamic

CPU, central processing unit

DEM, discrete element method

FCC, face centred cubic

FEM, finite element method

N-S, Navier-Stokes

PDE, partial differential equation

PDF, probability density function

RAM, random access memory

RCM, reduced continua model

REA, representative elementary area

REV, representative elementary volume

SAP, super absorbent polymer

SFR, SAP/fluff ratio

U.f., unbalanced force

1. INTRODUCTION

The fluid dynamics inside porous media, in all the various forms in which it arises, play an essential role in the definition of a wide range of investigations, driven by industrial interests or purely scientific. In 1856 the study of the engineer Henry Darcy aimed at the understanding of flow in aquifers [1], setting the bases of modern hydrogeology and petrophysics. Nowadays the same principles of averaged flow in a porous medium find application in food production or textile processing, in the oil industry or in the production of composite materials. It is therefore not surprising that in recent decades there have been numerous publications and mathematical models proposed by the scientific community in the field of porous media.

Porous medium systems can span length scales that range from millimetres to hundreds of kilometres in processes including energy generation in hydrogen fuel cells, geologic carbon storage, petroleum recovery, waste remediation, oxygen transport in lungs, and water supply. Besides the inherent issue of defining length scales, the issue of separation of those scales is important. Separation of scales means that one scale of observation is separated from another by orders of magnitude [2]. The introduction of new imaging technologies and the growing computing capacity provided by modern information technologies make a multi-scale approach recently possible, able to combine, in principle, macroscopic effects with physical principles on a pore scale.

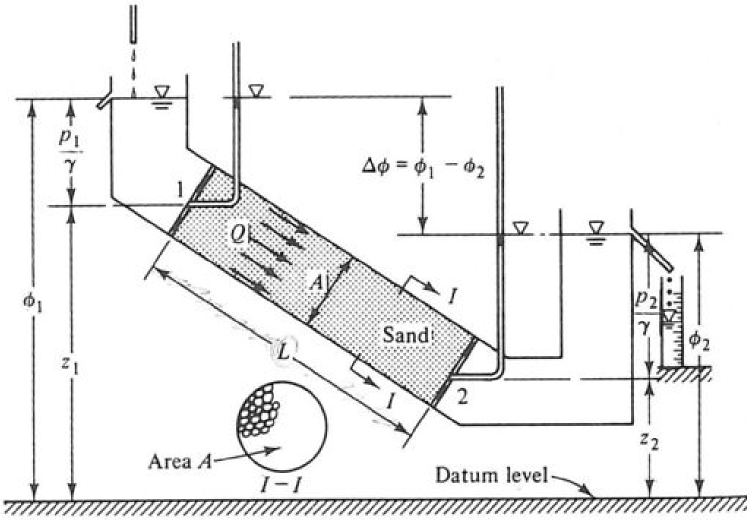

Figure 1.1. The Darcy's experiment [3].

The porous media studied by Darcy were homogeneous sand beds (i.e. granular porous media) with a well-defined granulometry. A sketch of the Darcy's experiment is provided in Figure

1-1, in which the investigated porous medium is a sand bed. The liquid flow is driven by the gradient of the hydraulic head (ϕ), defined as the sum of the elevation respect to a datum level (z) and the liquid pressure (p). In this system, preferential flow directions cannot be recognized. In other words, any set of Cartesian axes represents the main directions of the medium, in every point of the considered domain. It is useful to define immediately the concept of material or physical points. For a fluid, the denomination material point refers to the smallest volume within which it is possible to neglect the molecular effects. In this way a material consisting of a set of molecules is treated as a continuous that fills the entire space. In the case of a porous medium, in order to treat the medium as a continuum, as considered by Darcy, it is necessary to pass to a coarser mean level, the macroscopic level, and introduce the concept of Representative Elementary Volume (REV) (see for example Bear, 2013 [2]). Similar to what was said for the material points, this volume is the smallest domain within which a sufficient number of pores is contained to allow a sensible statistical mean, necessary for the concept of continuum. Consequently, the characteristic length of the REV must be at least one order of magnitude greater than the characteristic length of the pore or granule (for a dissertation of the magnitude scales in porous systems, see for example Gray & Miller, 2014). Related to the concept of REV is the volumetric porosity, or the ratio between the volume of the pores contained in a reference volume and the reference volume itself. The REV is therefore defined as the smallest reference volume within which it is possible to measure the porosity independent of scale, as represented in Figure 1-2.

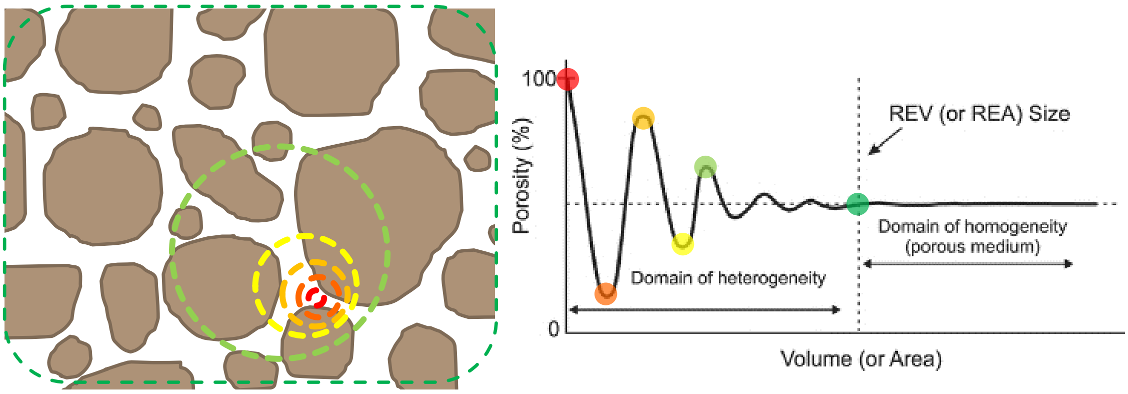

Figure 1.2. A 2D illustration of the concept of REV (or REA for areas) related to the value of porosity, for a porous granular sample [3]. *A value of porosity is associated for every area considered in the dashed circles.*

The approximation of the continuum was the first method used to describe flows in porous media [2]. It is possible to derive it considering simply geometry patterns, for example comparing the porous system to a set of a straight capillary tubes (see for example [4]). In this way, it is possible to relate the permeability to geometrical features, such as the cross-areas of the tubes and their tortuosity. On the other hand, it is also possible solve mass and momentum balance equations of fluid, inside a realistic geometry. To this end it is necessary to understand in detail the investigated porous structure, monitoring the connection and the arrangement of the pores inside the structure, as well as their dimensions. There are numerous imaging techniques developed in order to obtain this information (e.g., the different variants of confocal microscopy, computerized tomography, magnetic resonance) and in the same way great must be the power of the computers that handle an ever-increasing amount of information. Once a realistic representation of the porous system is obtained, having the theory of fluid mechanics available, in principle it is possible to derive the details of the flow domain. For instance, it is possible to use the Navier–Stokes equations for the flow of a viscous fluid in order to determine the velocity distribution in the empty space, satisfying specific boundary conditions on all interfaces between the fluid and solid phase (see for example Narsilio, Buzzi, Fityus, Yun, & Smith, 2009).

Between the resolution of the Navier–Stokes equations on a porous scale and the implementation of balance equations of quantities averaged on a macroscopic scale, a plethora of models are developed that reproduce the phenomenon satisfying different levels of detail (e.g., Thermodynamically Constrained Averaging Theory [2], Pore Network [6], Lattice Boltzmann [7], Full Morphology [8,9]). These models may be based on statistics or a precise knowledge of the porous structure, assisted by an accurate scan of the structure of the studied porous medium.

This interest of the scientific community in the phenomena of transport in porous media is certainly driven by a strong industrial need. InterPore (www.interpore.org) is, by way of example, one of the world's largest scientific organizations in this field and is massively sponsored by large industrial groups. In addition to areas historically linked to these issues, such as hydrogeology and the extraction of oil from underground deposits, the understanding of physical phenomena on a porous scale of complex systems such as food, composite materials or fabrics, turns out to be decisive for the design of finished products with unusual properties. These certainly include absorbent hygiene products (e.g., diapers, absorbents, pads), which are often multi-layered composite materials, consisting of a fibrous matrix (fluff) in which particles of Super-Absorbent Polymer (SAP) can be dispersed, amplifying the absorbing power of the final product. They belong to the class of porous absorbent media, together with some types of clays and foods, and incur substantial structural modifications due to the absorption of the liquid, modifying the flow pattern of it.

In this thesis, samples of composite absorbents were used, in which a significant amount of SAP particles is dispersed in a matrix of cellulose fluff fibres. Optimal formulation and manufacturing of the final product may greatly benefit from modelling of unsaturated flows within and across the layers that compose the AHP. The aim of the Thesis is to describe and propose constitutive relations for this complex matter, with the view of modelling swelling particles and fluff across scales.

1.1. MATERIAL DESCRIPTION

Modern absorbency products are made up of a fluff fibre matrix in which Super-Absorbent Polymer particles are dispersed.

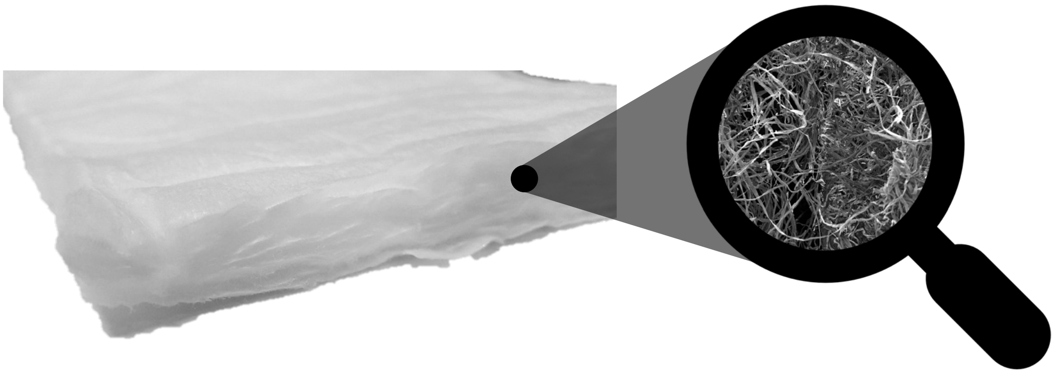

Figure 1.3. The core layer of an AHP, with a magnified representation of the fibres matrix (fluff).

i. SUPER ABSORBENT POLYMER

SAP particles are used in many applications, both for absorbing huge amount of liquid water and for guarantee a minimum value of porosity at low confining pressure, in a wide range of porous matrix. They are hydrophilic polymers, usually polyelectrolytes such as sodium polyacrylates or polyacrylamides [10]. The hydrophilic chains are connected through cross-linker polymer chains, in order to prevent loosening of the porous matrix and to stabilize the particle shape upon absorption [10]. Due to the presence of ions on the polymer chains, saline concentration of the absorbed solution influences the absorption equilibrium, due to osmotic effects [11]. The chemical composition and the content of the cross-linker chains influence the swelling kinetics and the final swelling ratio, i.e. the mass of liquid absorbed per unit mass of SAP. The stiffness of the particles, that at a dry state have a sugar-like appearance with white/yellow colour [10], strongly depends on the extent of swelling and chemical composition and preparation.

Figure 1.4. Dry SAP particles (left) and swollen SAP particles (right).

The particles used for industrial purposes are usually the result of a coarse grinding of an SAP block and consequently have quite different shapes and sizes, as it results from Figure 1-4 and Figure 1-5. The shape and the size of the particles also influence the rate and the maximum extent of the swelling process. Small particles are characterized by larger surface area to volume ratio, hence, larger initial absorption rate [12]. Similarly, angular particles have a larger surface area to volume ratio compared to spherical particles, a feature that enhances initial absorption rate.

The production of porous SAP particles is recent. Due to the inner channels, they maintain a high ratio between the surface and the volume even for high degrees of absorption [10]. The shear modulus of SAP decreases with increasing swelling ratio [13]. High levels of cross-linker increase particle porosity and absorption rate, at the expenses of absorption capacity, and bring enhanced stiffness and low sensitivity to the change of salinity [14].

Several experimental protocols for determining the properties of SAP are described in [10]. Since the forces acting on the surface of the particles definitely modify the swelling equilibrium [11], the experimental equipment allows to control the load on the samples. The easiest data to acquire is the free-absorbency capacity, related to the amount of liquid absorbable in the absence of loads. In these experiments, SAP particles freely swell in a distilled or saline bath for a considerably long time, generally 1 hour. Reached the equilibrium, the bunch of particles is dried and weighted, to measure the amount of water absorbed. At this point, three methods are described:

- the teabag method, in which the particles were originally placed in a teabag and the excess of water is removed by hanging the bag until no liquid is dropped off;
- the centrifuge method, in which the water in the bag is removed by a centrifugal separator;
- the sieve method, in which the bunch of particles is first filtered with a wire gauze, then it is dewatered carefully and rapidly using a piece of soft open-cell polyurethane foam until the gel no longer slips from the sieve when it is held vertical.

Among them, the centrifuge method is certainly the most feasible one, because of the small amount of SAP needed for the measurement and for the fast and secure dewatering.

The absorbency under load (AUL) is usually given in the patent literature and technical data sheets by industrial SAP manufacturers [10]. In this experiment, the SAP sample is in a saline bath, usually $0.9\%_w$ of NaCl solution, with a weight upon it. The applied loads are conventionally measured in bar. The most used values are 0.3, 0.6 and 0.9 bar.

Regarding the swelling kinetics, the vortex method is the most rapid and simple way to evaluate SAP swelling rate and it is often employed in R&D and technical laboratories [10]. For this experiment, the sample is put in stirred baker poured with water or a saline solution, at a controlled temperature. The time elapsing from the addition of SAP into the fluid to the disappearance of vortex is measured and the swelling rate is calculated from this value. In order to have a profile of swelling against time, it is necessary to have repeated measurements of swelling at consecutive time intervals [10]. The reported swelling-time profile of the SAP particles in a distilled water bath is usually interpreted with the Voigt-based viscoelastic model [15]. In this study, an indicative maximum capacity of SAP of 240 g of distilled water per gram of SAP was provided. The kinetics itself is considered linear and the proposed swelling-time profile fits reasonably with the assumptions. The kinetic reaction is described as follows:

$$\theta_t = \theta_e \left[1 - \exp\left(-\frac{t}{r_t}\right)\right], \tag{1.1}$$

where θ_t is the degree of swelling as the ratio of mass of absorbed liquid per mass of SAP at any moment, θ_e, the equilibrium swelling, is swelling at infinite time or maximum water holding capacity, t is the swelling time and r_t, the rate parameter, is the time required to reach 63% of the equilibrium swelling. This equation is based on Fick’s second law of diffusion and it is applicable at individual particles with varying diameter [16]. The same kinetics is obtained by Diersch et al., 2010 [17], assuming that every active site of SAP may react and it is accessible to the liquid.

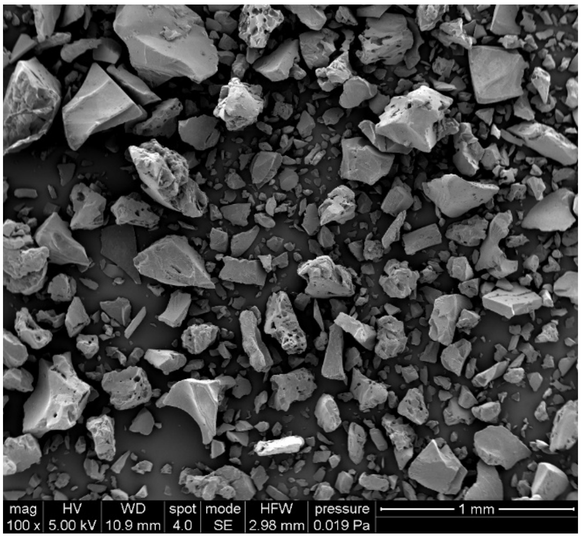

Figure 1.5. An image at SEM of the SAP particles which are blended with the fluff inside the investigated products.

The stiffness of the SAP particles, in their dry or swollen state, is crucial form a practical viewpoint. Zohuriaan-Mehr and Kabiri [10] have proposed rheological measurements to describe the mechanical properties of a swollen gel. It is possible to perform measurements with a rotational rheometer in the linear viscoelastic (LVE) range, where the elastic modulus (G') and the viscous modulus (G'') are independent of the strain amplitude. To set the experiment, the LVE regime must be determined using a swollen sample at equilibrium, drained from the interstitial water. The rheometric measurement are then evaluated at constant frequency, with strain values in the LVE range.

Sweijen et al. (2017) [9,18–20] recently investigated the changes on fluid dynamic properties of a bed made of SAP particles, because of the swelling. They used several modelling techniques to assemble packing of spheres and to measure the change in properties during the swelling of SAP particles. They were able to obtain macroscopic measurements from a grain-scale study, in which Discret Element Method (DEM) simulations were widely used. This method allows to simulate the movement of individual particles in a porous granular medium [21] and is applied in multiple fields, from the study of soils and rocks to the study of industrial granular flows. The virtually generated grains may move in four different ways: sliding, rolling, spinning and twisting.

ii. *Fluff*

In the AHPs, fibres are used to create both non-woven sheets and absorbent layers. As regards the core and absorbent layer, cellulose fluff pulp is commonly used. It is a chemical pulp made from long fibre softwood and it shows high levels of absorbance. It has been used for diapers since the 20s of the twentieth century, even though recently the advent of the SAP has changed its role inside the product: if in the past fluff fibres were the absorbent material, now their role is to give the products enough structure, both in a dry or in a wet state. The words "chemical pulp" designate the product of the process which separates the wood fibres (i.e. lignin, hemi-cellulose, cellulose) with the aid of a chemical solvent. The most employed chemical process is the Kraft process, used in the paper manufacturing [22]. A study on the mechanical properties of a cellulose fibre fluff can be found in Heyden (2000) [23] where stresses and contacts among the fibres of the cellulose fluff are measured through FEM simulations on computer-generated 2D or 3D fibres network.

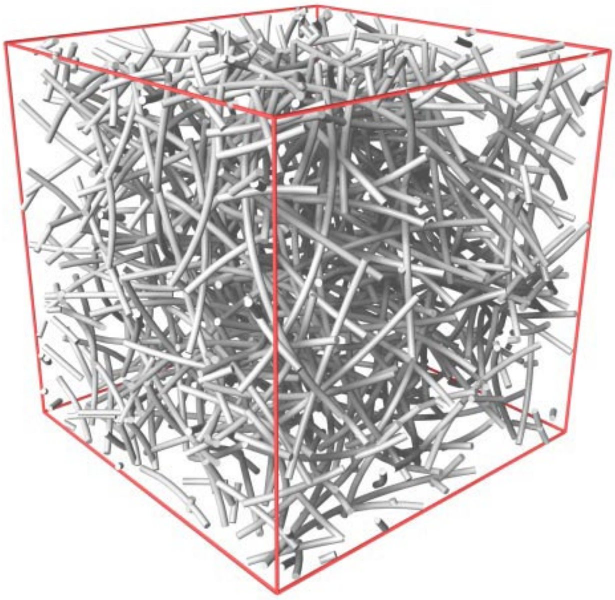

Figure 1.6. The periodic cell of cellulose fibre fluff investigated by Heyden (2000) [23] *in her FEM study.*

In modern AHPs, SAP particles absorb most of the liquid and undergo swelling and morphological modifications extended to the entire structure. The presence of fibres is essential to avoid blocking effects inside the storage layer due to the swelling of the SAP particles. Altogether, the optimum design of these products is established through a careful balance of many physical and economic variables, adding extreme complexity to their characterization and manufacturing.

1.2. PREVIOUS MODELLING APPROACHES

For materials with a known pore structure, computational fluid dynamics (CFD) is an essential predictive tool, which can effectively forecast very detailed flow patterns. The algorithms used to solve the PDEs system numerically in time and space domain are numerous and many examples can be found in the literature (e.g. Hirsch (2007) [24]). One of the most widespread and in some way endearing challenge is CFD in porous system [4,25,26]. Since the very first studies carried out by Darcy (1856) [1], the modelling of saturated and unsaturated flows has been uninterruptedly developed and has found its applicability in both industrial and scientific fields.

Even though it is always possible to solve the momentum balance equations, usually Navier-Stokes' (N-S) equations, in a realistic porous domain, the application of volume or surface averaging procedures is often necessary in order to obtain the most accurate result with a poor knowledge of the porous system morphology at the small length scales. Then, to reduce the computational effort of numerical simulations, porous media are often considered as continua. In this case, a well-sized simulation domain should contain several REVs, to be representative of the entire system (e.g. Bear (2013) [3]). In the case of AHP, the smallest dimension is the thickness. The thickness of a diaper core is around 1 cm, at its dry state, whilst the fibres and the SAP particles sizes hardly overcome 1 mm. Along the on-plane directions, the sizes of the AHP are of the order of tens of centimetres. Thus, the thickness is the only direction in which the presence of multiple layers of REV is not assured.

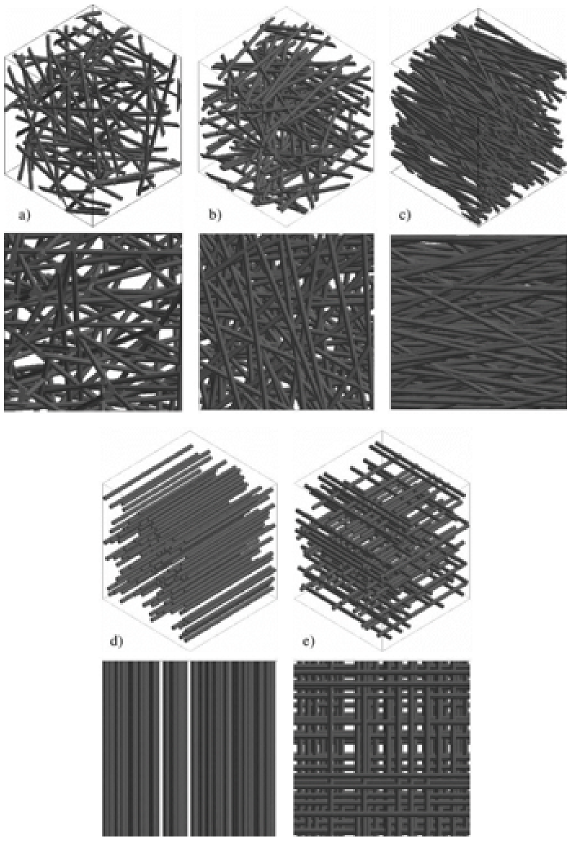

Figure 1.7. The different representations of a fibre porous medium investigated in Tahir and Vahedi Tafreshi (2009) [27].

Topological microstructural and flow properties of fibrous materials have been widely studied in literature, through generation of digital images of 2D and 3D fibrous microstructures [27–30], image analysis of real fibrous matrixes (see for example Aslannejad and Hassanizadeh (2017) [31]) or modelling liquid infiltration at a macro-scale [32–35]. As a way of example, in Tahir and Vahedi Tafreshi (2009) [27] the effect on permeability tensor and relative permeability of different orientations of fibres were investigated, as it is shown in Figure 1-7. In this work, N-S equations in the creeping flow regime were solved for each of the virtual geometry developed, in the void space between fibres. Form the evaluated pressure drops, Tahir and Vahedi Tafreshi (2009) [27] were able to estimate the permeability by applying the Darcy equation.

A different approach is applied in Ashari and Vahedi Tafreshi (2009) [28], in which a full-morphology is conducted. After the generation of the fibre model of the structure of a fibrous sheet, the pore morphology model was applied, in order to numerically obtain the capillary pressure – saturation curves of the material. Based on the Young-Laplace equation, the algorithm gradually introduces liquid from the wet boundary, in the form of spheres of decreasing diameter, in order to mimic the increasing capillary pressure. Through this method, it is possible to produce capillary pressure – saturation curves of the investigated ensemble.

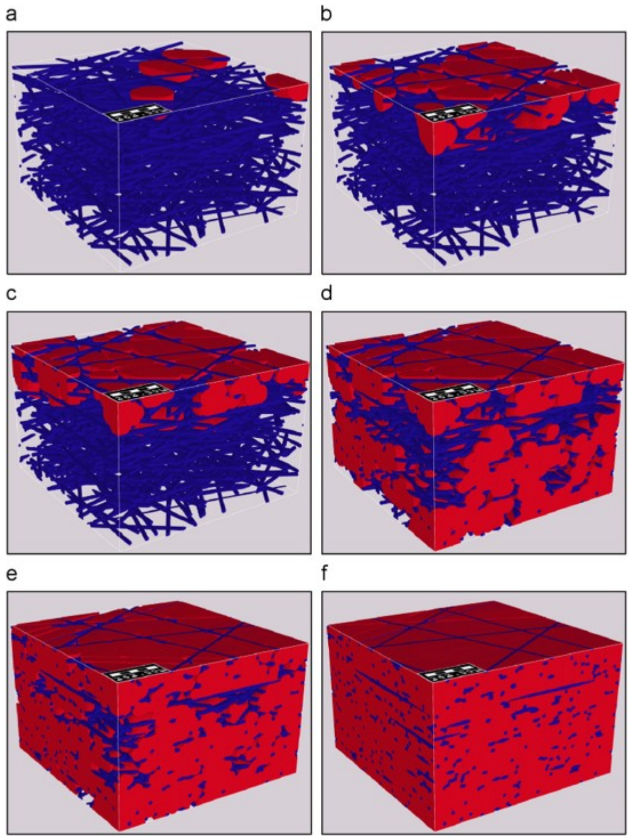

Figure 1.8. A visualization of the full-morphology method applied for fibrous sheets by Ashari and Vahedi Tafreshi (2009) [28].

The use of continuum assumption to model porous media requires to identify a representative elementary volume (REV) in which it can be considered space-averaged properties. To reduce statistical errors associated with the size of the fibrous porous domain, Clague and Phillips (1997) [36] proposed to use the permeability measurement to estimate the minimum size of the REV.

Among fibrous porous systems, fibres sheets are commonly treated as thin porous layers. A porous layer could be defined "thin" in two cases: when its dimensions do not fulfil the REV requirements (physically thin) or when its thickness is much smaller than the planar directions, even if the layer dimensions satisfy the REV requirements (geometrically thin) [35,37,38]. The applicability of continuum balance equations for physically thin porous media has been argued, due to the inexistence of an REV for these materials. Qin and Hassanizadeh (2014) [37] proposed a model for this kind of porous media in which all the properties are averaged along the thickness of the layer (RCM, Reduced Continua Model). The main advantages of this model are the rigorous thermodynamic formulation, the usage of layer-thickness-averaged material properties which are usually easily measurable and the reduction of computational efforts due to the 2D nature of the resulting models. In the case of AHP, the thickness is not lower than 3 mm, whilst the particles and the fibres that compose it have dimensions in the order of hundreds of micrometres. Thus, these composite materials, belonging to the category of geometrically thin layers, can be treated with a continuous approach.

As regards the wicking of paper-like swelling porous media, Masoodi and Pillai (2012) [39] proposed a single-phase flow model, in which a sharp interface is considered between liquid and gas phases. In the porous domain filled with liquid the Darcy's law is used while the interface is moving at the liquid velocity. The applicability of the model is related to appearance of a sharp interface between the phases, so to the position on the phase diagram proposed by Lenormand (1988) [40] of the specific investigated fluid dynamic problem. Consequently, many details of the porous matrix are necessary in order to evaluate the two dimensionless numbers, Reynolds and Capillarity numbers, which are the input variables of that diagram.

Models formulated using the discrete element method (DEM) avoid any uncertainties due to REV averaging (for an insight on DEM see for example Cundall and Strack (1979) [21]). Sweijen et al. (2017) [9,18] studied the absorption dynamics of a granular pack of swelling SAP particles using a DEM-based modelling approach. The size of the pack considered is more than a REV, in order to reduce the statistical errors. The particles considered could be spherical or irregular shaped, made of clumps of regular spheres, i.e. a set of overlapping spheres, bounded together, which mimics the shape of an irregular SAP particle [41]. The swelling kinetics affects the stiffness and the size of the particles, inducing changes in interactions among them. Evaluation of macroscopic quantities (e.g. size of the pack, porosity, permeability, pressure–saturation scanning curves) may be accomplished once the forces acting on the packed granular bed are at equilibrium. Kunhappan et al. (2017) [42] developed a numerical model in which discrete element method and finite volume method are coupled to study the behaviour of flexible fibres under inertial flows. Fibres are considered as chains of straight cylinders, each one bonded at the edges and with spherical ends. The momentum balance equation considers contacts with other objects and the exchange between fluid and fibres. It has been validated for different experimental studies, making it a powerful tool for the comprehension of similar systems. On the other hand, the very high computational effort needed to process a simulation with many disordered fibres reduces its applicability and represents a major drawback of this approach for extensive application.

Once a realistic configuration of the porous system has been obtained, by computerized scanning of the sample or DEM modeling, it is possible to define its characteristic dimensions on a pore scale. In this case, DEM provides an artificial packing that can be used for establishing hydraulic properties whilst maintaining a physical packing based on a contact mechanics. Based on the pore network modeling, it is possible to distinguish two types of empty space: the actual pores and the channels that join them. The first ones can be considered small reservoirs in which the fluids coming from the throats accumulate, while the throats are the actual channels within which the fluids flow. Referring to the Young–Laplace law, the pressure difference between the two phases and the diameter of the channels are the variables that govern the movement of fluids in this system. Through this simplification it is possible to considerably reduce the computational times for the simulation of a liquid intake or a drainage within the porous system. Consequently, it is possible to reconstruct the imbibition and drainage curves for a specific porous system once the dimensions of the throats and pores and their connections are known.

To this end, it is worth mentioning the Pore Unit Assembly and the Pore Morphology Method, whose performances were compared in the study of Sweijen et al. (2017) for different classes of granular glass beds [9]. In implementing these methods, the definition of the form of the liquid–gas interface that can be semi-spherical or having a more complex representation is decisive, as in the case of the Mayer and Stowe–Prince model, in which the shape of the interface surface is elongated.

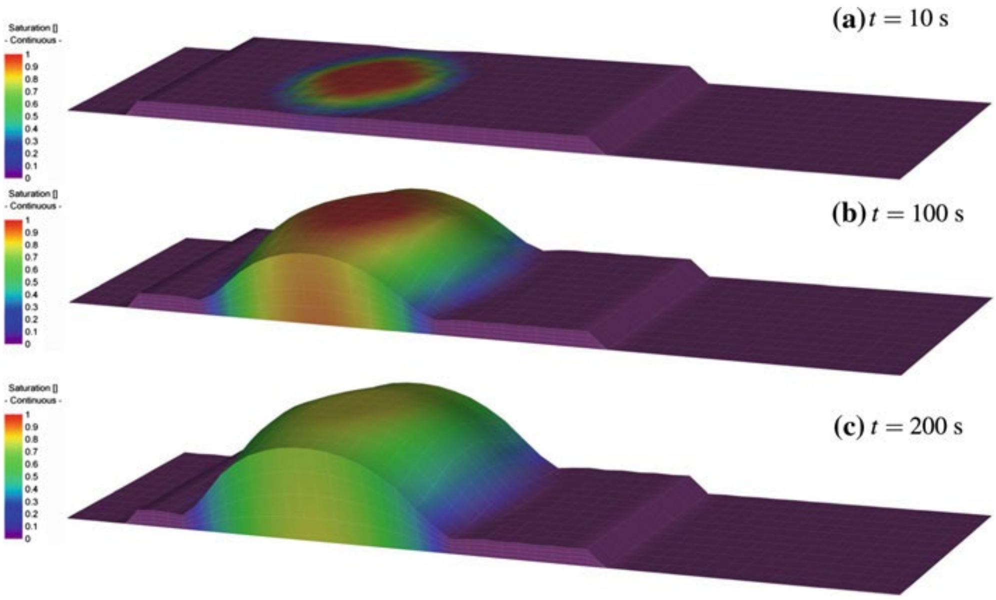

Figure 1.9. Snapshots of FeFlow simulations, from Diersch et al. (2011) [43].

Despite the difficulties related to define an averaged domain, continuum-scale models have proven to be quite effective to simulate complex processes in porous materials as in the case of swelling of partially saturated granular materials. A mathematical model based on Richards' equation has been developed to relate fluid-dynamic properties and swelling dynamics for this kind of porous media [17,43]. Moving from mass and momentum balance equations for a multiphase isothermal system, Diersch et al. developed a model consisting of a system of nonlinear partial differential equations (PDEs) and proposed alternative forms of closure equations. Numerical simulation of the equations was accomplished using the Galerkin FEM [43,44].

1.3. OUTLINE OF THE THESIS

The present study aims at characterizing relevant morphological and hydraulic properties of AHP, consisting of storage layers made of fluff fibres and SAP particles, with different SAP/fluff ratio (SFR). The dependencies of these properties (e.g. porosity and hydraulic conductivity) on the absorption extent of the SAP particles has to be clearly acknowledged, in order to properly model with continuous assumptions this particular porous system.

In the second chapter, a detailed description of the model adopted from literature [17] is provided. The numerous variables and equations are described. A focus is given to the various closure equations and sub-models implemented in the main model.

In the third chapter, a comprehensive tailored experimental protocol is presented for the characterization of properties and constitutive parameters relevant to AHP performance. The protocol is based on a combination of mutually complementary experimental methods for the characterization of the composite medium: absorption rate, porosity, hydraulic conductivity, retention model, swelling. An effort has been made to develop experimental methods tailored to the peculiar nature of AHP to overcome some limitations and drawbacks of general-purpose characterization methods. The experimental protocol has been used to test a set of AHP materials, characterized by different values of SAP/fluff ratio (SFR). The results have been directed to set the closure equations and constitutive parameters of multiphase flow models in which the porous media is treated as a continuum [17] aimed at the dynamical simulation of AHP performance under realistic imbibition/drainage conditions.

The fourth chapter aims at characterizing by CFD modelling the behaviour of composite materials during imbibition and drainage cycles. The performances of the composite materials have been characterized in terms of absorption time and absorbed fluid spatial distribution upon iterated imbibition/drainage cycles. The comparison of the experimental results with CFD modelling simulations aims at model validation and fully understanding of the mechanisms of hydrodynamics of unsaturated flows in swelling porous media.

In the fifth chapter, a numerical study based on the discrete element method (DEM) is presented for the characterization of morphological properties of the investigated materials. The model was developed in YADE, an open source software focused on DEM (see Appendix C for a brief description of the method implemented in the software). The simulations reproduce the samples as they were granular beds. The code allows an easily tuning of relevant numerical and physical parameters. A series of preliminary estimations have been necessary to faithfully represent a realistic AHP sample. The results of the DEM computational experiments have been compared to the values obtained from the experimental campaign described in the second chapter.

At the end of the thesis, conclusions and perspectives on multi-scale modelling of swelling granular materials is given and an outline for future research is provided.

2. THE MATHEMATICAL MODEL

The model aims at predicting liquid flow and absorption in a deformable porous system [17,43]. Although the porous materials are characterized by a pronounced inhomogeneity, the porous matrix has been modelled as a continuum with averaged properties, following the approach proposed by Diersch and co-workers. Accordingly, a Representative Elementary Volume (REV) is defined at first, as the minimum volume of the composite matrix in which it is possible to average properties, measuring consistent values without significant deviations [2,3]. In the following, all the volume balances are referred to a REV. In the material frame, where every material point is labelled with coordinates of its initial space position, the REV domain remains constant. Otherwise, in the spatial frame, coordinates of particles change, and REV could swell or shrink.

2.1. GENERAL ASSUMPTIONS

Three phases (solid, liquid and gas) coexist in the porous medium. Mass and momentum transfer may take place among the phases, whereas interphase energy transfer is ruled out under the assumption that the flow is isothermal. The gas and the liquid phases consist of only one substance (air for gas and salty water for liquid). The solid phase consists of three compounds:

1. the carrier material (fluff fibres), that does not take part to water absorption reactions;
2. the SAP particles;
3. the water absorbed by the SAP and "trapped" inside the particles.

The liquid absorbed by SAP particles has then to be considered as a solid component, which can no longer retrieve its liquid state. Regardless of the reference frame, the mass of fluff fibres and SAP particles inside a REV does not change during time. The only change in the solid mass is due to the amount of water absorbed by the SAP particles. Density of water inside the particles is assumed to be the same as that of the liquid phase. Accordingly, particle density changes during absorption. Similarly, other mechanical properties of the particles change during the absorption reaction, like elastic and shear moduli [10,13,14,45].

The liquid and the gas phases fill together the void (ε) of the composite material (the bulk volume without the solid volume) and it is useful to define a gas and a liquid saturation s, expressed as the ratio between the phase volume and the void volume:

$$\varepsilon^l = \varepsilon s^l, \qquad \varepsilon^g = \varepsilon s^g = \varepsilon(1 - s^l), \qquad \varepsilon^s = 1 - \varepsilon. \tag{2.1}$$

The superscripts l, g and s refer to the phases inside the domain, liquid, gas and solid, respectively. Gas and liquid phases cannot interpenetrate, and they can pass through the boundaries of the system, filling or emptying the voids. In order to have a continuum porous media description, it is necessary to track material particles of the phases during time, while the REV is deforming. In every point of the spatial frame, the three phases coexist and there is a correspondence between the material point of each phase and its position during time. So, the position in the spatial frame ($\boldsymbol{x}$) occupied by a material particle of phase α is a bijective function of time (t) and of the material particle coordinates ($\boldsymbol{X}^\alpha$):

$$\boldsymbol{x} = \boldsymbol{u}^\alpha(\boldsymbol{X}^\alpha, t), \tag{2.2}$$

where $\boldsymbol{u}^\alpha$ is the displacement function for phase α. Due to the one-to-one correspondence between the displacement function and the material points, the Jacobian of the displacement function exists, and it is always positive. Referring to the solid phase displacement, the Jacobian (J^s) represents also the deformation (swelling or shrinkage) of the porous media as the ratio between the current control-space volume ($|\Omega^s|(\boldsymbol{x}, t)$) and the initial one ($|\Omega_0^s|(\boldsymbol{X}^s, 0)$) [4,17]:

$$J^s = \det(\boldsymbol{\nabla u}^s) = \frac{|\Omega^s|(\boldsymbol{x},t)}{|\Omega_0^s|(\boldsymbol{X}^s,0)}. \tag{2.3}$$

Using this approach, it is possible to define the solid velocity as the temporal derivative of the displacement of a fixed solid material particle. Under these assumptions, mass and momentum balances for each phase can be developed in the deforming domain of the continuum porous media.

2.2. BALANCE EQUATIONS

The momentum balance on the liquid phase is a modification of the Darcy's law for unsaturated media:

$$\varepsilon s^l\left(\boldsymbol{v}^l - \boldsymbol{v}^s\right) = -\frac{k_r^l \boldsymbol{k}}{\mu^l} \cdot (\boldsymbol{\nabla} p^l - \rho^l \boldsymbol{g}) = -k_r^l \boldsymbol{K}^l \cdot (\boldsymbol{\nabla} \psi^l - \boldsymbol{e}), \tag{2.4}$$

where $\boldsymbol{v}^l$ and $\boldsymbol{v}^s$ are the liquid and solid phase velocities, respectively, k_r^l is the relative permeability for the liquid phase, $\boldsymbol{k}$ is the permeability tensor of the porous medium, $\boldsymbol{K}^l$ is the hydraulic conductivity tensor, μ^l and ρ^l are the viscosity and the density of the liquid phase, respectively, p^l and ψ^l are the pressure and the pressure head of the liquid phase, respectively, and $\boldsymbol{g}$ and $\boldsymbol{e}$ are the gravity acceleration and the gravity unit vector, respectively. Because of the displacements of the solid phase arising during the swelling process, the liquid flux is defined considering the relative velocity between liquid and solid phases. The hydraulic conductivity tensor is influenced by liquid saturation, through the liquid relative permeability, that is equal to one in a fully saturated porous media.

Stress-free deformation of the solid phase is considered as a result of the absorption process. Accordingly, non-linear terms related to plastic deformation are avoided and the solid strain is only a function of the swelling [4,46]. Furthermore, shear effects are neglected, and the strain has only normal components. Accordingly, the momentum balance on the solid phase reads:

$$\boldsymbol{\nabla} \cdot \boldsymbol{u}^s = d^s := \frac{|\Omega^s|(\boldsymbol{x},t) - |\Omega_0^s|(\boldsymbol{X}^s,0)}{|\Omega_0^s|(\boldsymbol{X}^s,0)} = J^s - 1, \tag{2.5}$$

where d^s represents a scalar volumetric strain defined as a change of the control volume. Using Cartesian coordinate system, if the strain is unidirectional, that is the material is laterally confined and can swell only along one direction, the scalar volumetric strain coincides with the strain in that direction and no approximations are needed [17].

For the gas phase, momentum balance becomes trivial because the gas is considered stagnant and its velocity assumes the same value of the solid phase velocity.

As regards the mass balances, every phase can be treated with the same general multispecies conservation law. Mass exchanges between solid and liquid phases are defined by the absorption chemical reaction. The absorption process is an interfacial reaction, between SAP particles and liquid phase and then it is proportional to contact surface between phases, especially at the beginning of the reaction. It is assumed that all the SAP inside a material point can be reached by liquid, without considering the diffusional processes inside a single particle of SAP. The interfacial area is a function of the liquid saturation inside the porous matrix. In first approximation, the specific wet area could be set equal to the effective saturation, described below. The liquid density at the interface remains the same and approximately equal to the water density (no Donnan effects are considered) [11]. The maximum amount of water that SAP can absorb is related to the chemical potential equilibrium on the interfacial surface between SAP particles and liquid phase and it depends on the salinity of water. Besides, particle size distribution and shape of SAP particles have an influence on maximum swelling extent and absorption rate [47]. For instance, particles with smaller sizes react faster than coarser ones reaching the maximum swelling ratio sooner. Consequently, the overall kinetic constant must express an average along the progress of absorption of the behaviour of the smaller particles which are initially more “reactive” and that of the larger particles which are still “active” at the end of the absorption process. To this end, it was assumed that the overall kinetic coefficient changes during absorption, and linearly decreases with the amount of absorbed liquid. Therefore, the overall absorption rate is modelled with a quadratic law (for a further insight about this topic, the Reader is referred to Appendix A). Regarding the gas phase it is not necessary to consider a mass balance, because it can be obtained by difference from the mass balance of the liquid phase. Developing the general mass equation for the liquid and solid phases, neglecting gravitational effects inside the porous domain and the compressibility of liquid, a Richards-type flow equation and a differential equation for the absorption reaction are obtained. Then, the final PDEs system is:

$$\varepsilon \frac{\partial s^l(\psi^l)}{\partial t} - \boldsymbol{\nabla} \cdot \left[k_r^l \boldsymbol{K^l} \cdot (\boldsymbol{\nabla}\psi^l - \boldsymbol{e})\right] = -\left[\frac{\bar{C}_{SAP_0}^s}{\rho^l J^s} + \varepsilon \frac{\partial s^l}{\partial m_2^s} + s^l \left(\frac{\partial \varepsilon}{\partial m_2^s} + \frac{\varepsilon}{J^s}\frac{\partial J^s}{\partial m_2^s}\right)\right] \frac{\partial m_2^s}{\partial t}, \tag{2.6}$$

$$\frac{\partial m_2^s}{\partial t} = \frac{m_{2max}^s \left(1 - \frac{m_2^s}{m_{2max}^s}\right)^2 a^{sl}(s^l)}{\tau}, \tag{2.7}$$

$$\frac{\partial u^s}{\partial Z} = d^s. \tag{2.8}$$

Following the notation proposed by Diersch et al. (2010) [17] $\bar{C}_{SAP_0}^s$ is the initial solid bulk concentration of SAP, m_2^s is the swelling ratio, defined as mass of absorbed liquid per mass of SAP, m_{2max}^s is the maximum swelling ratio obtainable at a fixed saline concentration, τ is the characteristic time of the absorption reaction, a^{sl} is the saturation-dependent fraction of the solid–liquid interface area and Z is the only direction of the material frame of reference on which swelling occurs. As it can be noted, equation (2.6) merges mass and momentum balances for the liquid phase and equations (2.7) and (2.8) are the mass and momentum balances for the solid phase, respectively. The system is solved for the three primary variables ψ^l, m_2^s and u^s. The confining stress effects do not explicitly appear in (2.7). However, the different stress boundary conditions affect the kinetic parameters (i.e. maximum swelling ratio and kinetic rate). Similarly, the fibres limit the swelling, with an effect on the kinetic parameter.

To solve the system, other constitutive relations are required: porosity and saturated permeability dependences with swelling ratio, saturation dependences with pressure and swelling ratio and relative permeability dependences with saturation.

2.3. CONSTITUTIVE EQUATIONS

In order to solve the PDEs system, relations between the various components must be defined. Using bulk concentrations referred to the material reference frame is the easiest way to represent the system. In the material reference frame, the REV is not deforming, and SAP and fluff bulk concentrations are not changing during time. No water absorbed by SAP particles can leave the gel, so the absorbed liquid bulk concentration is constantly increasing inside the REV. Expression of key constitutive equation is detailed hereinafter.

iii. *DILATION FUNCTION*

The dilation function (J^s) is used as a proportionality coefficient to switch from spatial to material reference frame and vice versa and it is defined as in (2.3). Further calculations (see Appendix B) bring to an expression of the dilation function [17]:

$$J^s(m_2^s) = \frac{1}{1-\varepsilon(m_2^s)}\left(1 - \varepsilon(0) + m_2^s \frac{\bar{C}_{SAP_0}^s}{\rho^l}\right). \tag{2.9}$$

iv. *POROSITY*

The porosity is influenced by the degree of absorption (m_2^s) according to Diersch et al. (2010) [17]:

$$\varepsilon(m_2^s) = \frac{2\varepsilon_0}{1+(m_2^s\varepsilon_1+1)^{\varepsilon_2}}, \tag{2.10}$$

where ε_0, ε_1 and ε_2 are fitting parameters. It must be noticed that this equation considers only the absorption reaction by SAP as a cause for the decreasing of the porosity and any other causes, like collapsing of wetted hydrophilic fibres, are neglected. Moreover, the stress is not explicitly considered in this equation, although the fitting parameters are influenced by the stress state of each composite material.

v. *HYDRAULIC CONDUCTIVITY*

For the hydraulic conductivity, we adopted the following relation:

$$K^l(m_2^s) = \frac{K_0}{\left[1+\left(K_1 d^s(m_2^s)\right)^{K_2}\right]^{1-1/K_2}}, \tag{2.11}$$

where K_0, K_1 and K_2 are fitting parameters. The shape of the implemented function is the van Genuchten model proposed in literature for describing the retention model of porous media [48]. Many evidences show that fibres in composite materials are partially oriented during the production process by the wheel used to press the products. According to Ashari et al., permeability in fibrous sheets along the machine direction is twice the permeability along the other directions [30].

vi. LIQUID SATURATION

The dependency between liquid saturation and liquid pressure is expressed by introducing the capillary pressure (p_c) as a function of liquid pressure head:

$$p_c(s^l) = -p^l(s^l) = -\psi^l(s^l)\rho^l g. \tag{2.12}$$

Then, using the expression for effective saturation due to van Genuchten (1980) [48]:

$$s_e^l := \frac{{s^l}_{max} - s^l}{{s^l}_{max} - {s^l}_{min}} = \begin{cases} \frac{1}{\left[1+|\alpha\psi^l|^n\right]^{(1-1/n)}} & \psi^l < 0 \\ 1 & \psi^l \geq 0 \end{cases}, \tag{2.13}$$

where the effective saturation expresses the amount of liquid inside the void fraction referring to maximum saturation (${s^l}_{max}$) and residual saturation (${s^l}_{min}$). It must be observed that retention models exhibit strong hysteretic behaviour when imbibition and drainage processes are carried out in sequence. This means that it is necessary to use different parameters (α and n) for imbibition and for drainage. Furthermore, to ensure continuity of the saturation variable, it is necessary to introduce coefficients that take into account the saturation value of the current state of the material point [43].

vii. RELATIVE PERMEABILITY

In unsaturated flows in porous media, the wetting and the nonwetting phases are in contact inside the pore space. Due to the interactions between them at the interface, the conductivity for a single phase in an unsaturated media might be different from the case of a saturated porous media. To consider the modifications induced by these contacts, the permeability for a given phase is scaled by a coefficient, the relative permeability, function of the saturation of that phase. Its value is usually in the range between 0 and 1, that correspond to saturation values of 0 and 1, respectively. However, in some occasional cases, the relative permeability might exceed unity, as the permeability for the reference phase is enhanced while it is in contact with the other phase [3].

In the most general case, the relative permeability is an increasing function of the saturation. A method to measure it is to set an experiment in which the different phases flowing inside the same porous matrix at different flow rates. Then, from an evaluation of the volume occupied by the two fluids through scanning images techniques it can be measured the value of saturation inside the domain considered. The ratio between the calculated permeability at a given saturation with the already known absolute permeability gives the value of the relative permeability for the measured saturation [49].

Several models for relative permeability are present in literature [50–52]. In these models is necessary to introduce one or more parameters. The model presented here is a power law of the saturation, with a fitting exponent (δ) [53]:

$$k_r^l = {s_e^l}^{\delta}. \tag{2.14}$$

As it is reported in Tafreshi and Bucher (2013) [53], the exponent is closely related to the pore-size distribution of the media and it tends to smaller values as the distribution is wider. It is also reported that most porous media have a δ coefficient of 4. For fibrous materials it has been observed that the best value for the parameter is in the range between 3 and 4. Following the work of Ashari and Vahedi Tafreshi (2009) [28] and Ashari et al. (2010) [30], who performed numerical simulations to evaluate permeability functions of fibrous materials, in part 1 we set $\delta = 3$. In this work we also aim at understanding the dependence of this assumption on numerical results.

viii. HYSTERESIS

The hysteretic effects of imbibition and drainage cycles were taken into account, following the procedure proposed by Diersch et al. (2011) [43]. The main theoretical retention curves for the drainage (s_d^l) and for the imbibition (s_d^l) represent the maximum and minimum value of saturation for a given pressure head, respectively. The actual value of saturation for each point of the porous matrix depends on its history. The current saturation value is evaluated scaling the two main curves to match the real values. For this purpose, two coefficients are defined for scaling the curves:

$$\begin{aligned} c_d(\psi^l) &= \frac{s^l_{t-1}(\psi^l) - s^l{}_{min}}{s^l_d(\psi^l) - s^l{}_{min}} \\ c_w(\psi^l) &= \frac{s^l{}_{max} - s^l_{t-1}(\psi^l)}{s^l{}_{max} - s^l_w(\psi^l)}, \end{aligned} \tag{2.15}$$

where subscript $(t-1)$ means that the value of the variable is evaluated at the previous time step and the subscripts d and w refer to the main drainage and wetting curves, respectively. Therefore, at the reversing point, when the time derivative of pressure head changes its sign, the theoretical curves are scaled. Thus, the evaluation of the temporal derivative of the pressure head makes it possible to understand whether the process, for the specific material point, is an imbibition ($\partial\psi^l/\partial t > 0$) or a drainage ($\partial\psi^l/\partial t < 0$). Therefore, the current saturation is evaluated as follows:

$$s^l(\psi^l) = \begin{cases} c_d s^l_d(\psi^l) + (1 - c_d)s^l{}_{min}, & \dfrac{\partial\psi^l}{\partial t} < 0 \\ c_w s^l_w(\psi^l) + (1 - c_w)s^l{}_{max}, & \dfrac{\partial\psi^l}{\partial t} > 0 \end{cases}. \tag{2.16}$$

3. EXPERIMENTAL

Different types of composite absorbents have been characterized to determine physical properties and parameters of constitutive equations relevant to modelling. Table 3-1 reports selected properties of the investigated materials in terms of concentrations of the individual components. Four different basis weight of fluff were considered.

The calculation of the initial wet properties of the samples requires calculation of the initial porosity and bulk concentrations. Due to the collapse of fibres occurring during the first wetting of the sample [54], layers composed by fibres reduce their initial thickness at the beginning of an imbibition. Therefore, the reference frame in which void fraction and bulk concentrations must be measured is represented by the already collapsed layer. However, for a correct estimation of the wet thickness, the measurement must be carried out immediately after wetting before any significant water absorption by SAP particles could take place.

The value used to characterize the wet initial properties of the materials was that measured during the hydraulic conductivity test, after 10 s of imbibition. On basis of properties reported in Table 3-1 and the initial wet thickness, initial porosity and component bulk concentrations can be calculated. Initial wet properties are listed in Table 3-2.

Table 3.1. Formulation of composite materials.

Composite label	Fluff basis weight	SFR
OFF1	Low	0
OFF2	High	0
A1	Low	0.70
A2	Low	0.89
A3	Low	1.22
A4	Low	1.67
B1	Medium	0.73
C1	High	0.30
C2	High	0.55

Table 3.2 Initial properties of the wet composite materials.

Composite label	Thickness, h_0 (mm)	Initial porosity, ε_0 (-)
OFF1	2.5	0.90
OFF2	6.8	0.93
A1	3.31	0.886
A2	3.72	0.889
A3	4.22	0.888
A4	4.22	0.868
B1	5.32	0.887
C1	5.67	0.893
C2	6.19	0.885

3.1. POROSITY

Porosity tests were performed according to the following experimental procedure, using the test arrangement outlined in Figure 3-1. A cylindrical sample of 6 cm diameter (d) was compressed at 0.3 psi and immersed into a bath of saline solution for 2 h. The support that holds the sample and ensures its compression consists of two metallic grids, respectively top and bottom, to let the liquid permeate and wet the sample. The sample was placed on a porous glass plate, to enhance homogeneous contact with the liquid. Different salt concentrations were used to characterize sample properties at various swelling ratio (m_2^s). The amount of saline solution used for each sample was about 2 L, far exceeding the quantity that sample pads could absorb. Accordingly, the bulk concentration of salts in water did not change due to absorption by the polymer, and the Donnan effect was avoided [55]. The dry sample weight before the test was recorded (W_1). After the test, the weight of the swollen and wet sample was recorded again (W_2). Then, the sample was drained for 10 minutes using a vacuum pump and blotted with filter paper for 10 minutes, imposing an additional compression at 1.5 psi. Despite the increase of compression, no de-swelling of SAP particles was observed. Finally, the weight of the swollen drained sample was recorded (W_3) and the void fraction of the sample calculated on the basis of the removed volume of saline solution. The test analysis takes into account that a part of saline solution remains chemically bound to the cellulose fibres: an amount of 0.8 g of water absorbed per 1 g of fibres was assumed as reported in literature [55]. The final weights of the samples were compared with their initial weights, to measure the mass of water absorbed by SAP referred to its initial mass.

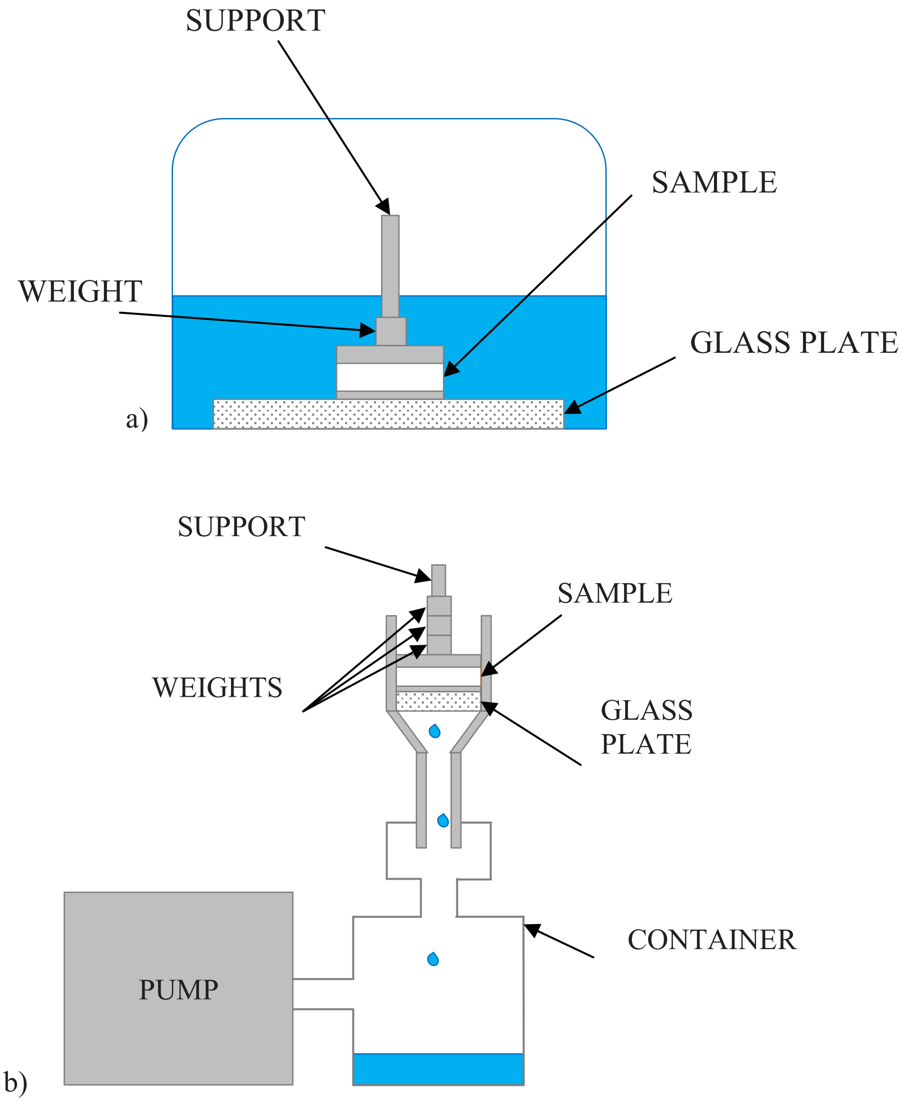

Figure 3.1. Outline of the experimental apparatus for the porosity characterization. a) Bath of saline solution; b) drainage of the sample.

The porosity of the sample (ε) is then calculated and correlated to the swelling ratio (m_2^s):

$$m_2^s = \frac{W_3 - W_1 - 0.8\bar{C}_{FL_0}^s h_0 \pi \frac{d^2}{4}}{\bar{C}_{SAP_0}^s h_0 \pi \frac{d^2}{4}}, \qquad (3.1)$$

$$\varepsilon = \frac{\frac{W_2 - W_3}{\rho^l}}{\frac{W_2 - W_1}{\rho^l} + h_0 \pi \frac{d^2}{4} \sum_i \frac{\bar{C}_{i_0}^s}{\rho_i^s}}. \qquad (3.2)$$

where ρ^s are solid densities and the subscript i refers to either solid phase (fluff and SAP) in the composite material.

Porosity of the composite materials is reported in Figure 3-2 and in Figure 3-3 as a function of swelling ratio for all the samples. The initial porosity was calculated from measurement of the sample thickness, as previously discussed.

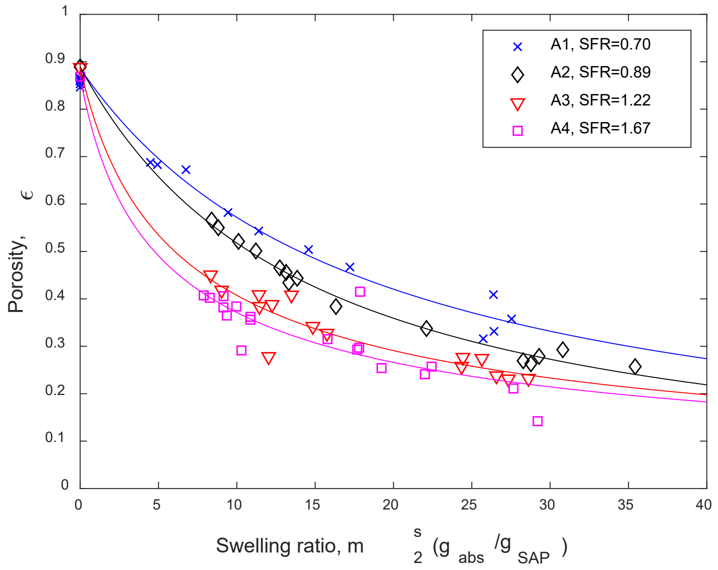

Figure 3.2. Sample porosity at steady state for the samples A1, A2, A3 and A4. Best-fit plots according to equations in Chapter 2 are reported for comparison.

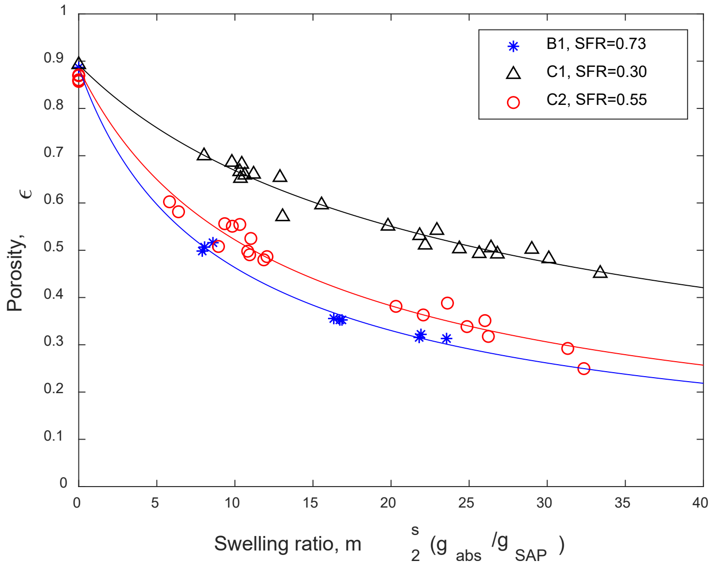

Figure 3.3. Sample porosity at steady state for the samples B1, C1 and C2. Best-fit plots according to equations in Chapter 2 are reported for comparison.

For the all the materials investigated, the porosity spans in a very wide range: nearly 0.9 at first, when the material is dry, the porosity decays to values as small as 0.2 upon swelling of SAP particles. Data points in figure 4 were used to estimate the fitting parameters of the regression model reported in Chapter 2. Best fit parameters are reported in Table 3-3, and best-fit lines are compared with data in Figure 3-2 and in Figure 3-3. The analysis of the results shows that:

- at pre-set amount of fluff used to make the composite material, the increase of SAP content results in a decrease of material porosity for every fluff basis weight;
- samples with similar SFR are described by a similar decrease in porosity with swelling ratio, even though a clear functionality with SFR cannot be recognized.

Table 3.3. Values of the fitting parameter for the porosity model for the investigated materials at steady state conditions.

Composite label	ε_1	ε_2
A1	0.106	1.026
A2	0.126	1.094
A3	0.471	0.696
A4	0.627	0.656
B1	0.269	0.796
C1	0.105	0.713
C2	0.184	0.836

3.2. HYDRAULIC CONDUCTIVITY

Hydraulic conductivity tests were performed according to the following experimental procedure using the test arrangement outlined in Figure 3-4. A cylindrical sample of 6 cm diameter (d), laterally confined and compressed at 0.3 psi, was wetted with a 0.9% saline solution, under a constant hydraulic head of 5 cm ($\Delta\psi^l$) on the top of the sample. The support that holds the sample and ensures its compression consists of two metallic grids to let the liquid permeate and wet the sample. The sample was placed on a metal grid and a mass scale was positioned below, so as to continuously weigh and record the amount of liquid passing through the sample (the amount of liquid through the sample at the time step t is $\Delta W^l{}_t = W^l{}_t - W^l{}_{t-1}$). The mesh of the thin metal grid was coarse, and its resistance to flow was negligible. The thickness of the sample (h) was also monitored and recorded along the test. When the measured thickness reached a constant value, the sample was considered at the steady state and fully swollen. Accordingly, the experimental procedure enables simultaneous measurement of the liquid flux through the composite material and of its thickness as functions of time.

The Darcy equation for permeability in saturated porous media is applied to evaluate the saturated permeability across the sample:

$$K^{l}{}_{t} = \frac{1}{\frac{\Delta\psi^{l}}{h_t}} \frac{(h_t - h_{t-1}) + \Delta W^{l}{}_{t} / \rho^{l} \pi \frac{d^2}{4}}{\Delta t}, \tag{3.3}$$

where the subscripts t and $t-1$ refer to quantities measured at current and previous time step, respectively. It is worth to note that permeability might not be isotropic, as the fibres are most typically oriented along one of the two directions orthogonal to the liquid flux, i.e. the machine-direction along which the fibres are pressed with a wheel during the manufacturing process [30].

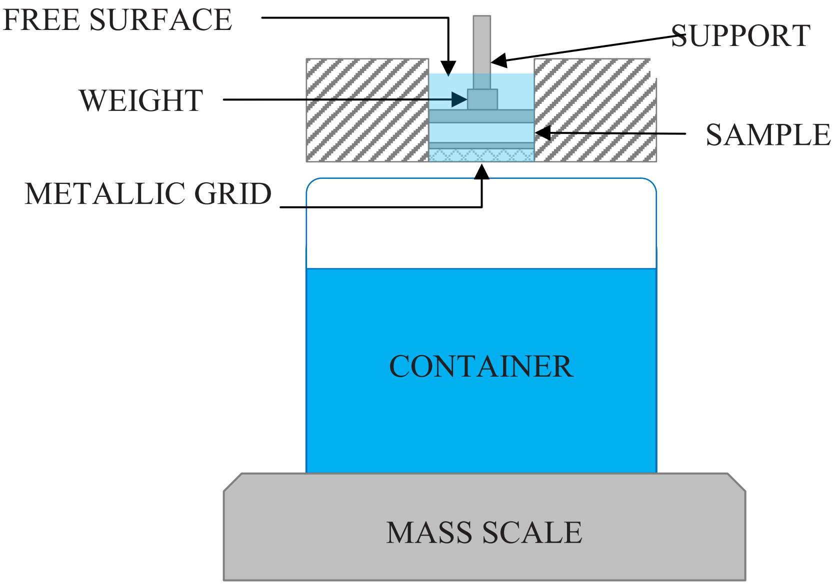

Figure 3.4. Outline of the experimental apparatus for the hydraulic conductivity characterization.

The experimental results obtained by means of these tests can be also used for the kinetic characterization of the composite material. Due to the complete saturation of the sample during the test, the swelling kinetics does not depend on spatial gradients and can be separately determined. Then, the kinetic parameters can be estimated and be exploited together with the porosity model parameters in order to fit the time-resolved dilation profile exhibited by the sample.

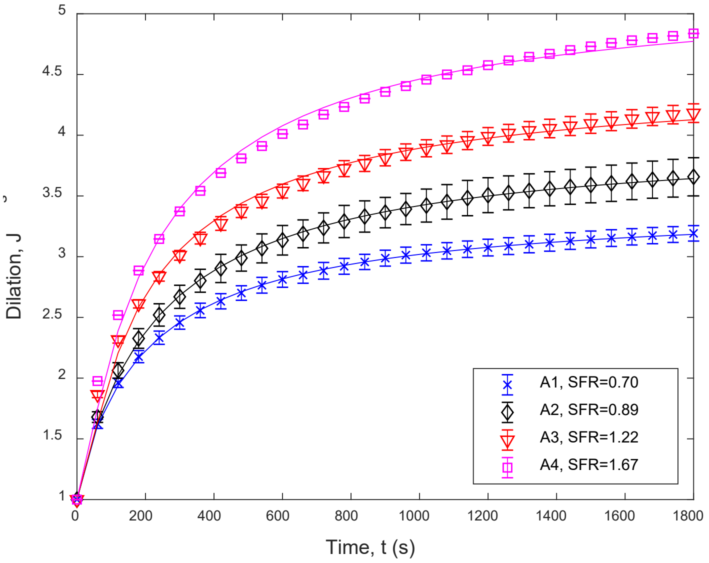

Figure 3.5. Swelling-induced dilation along the test for the samples A1, A2, A3 and A4. Best-fit plots according to equations in Chapter 2 are reported for comparison.

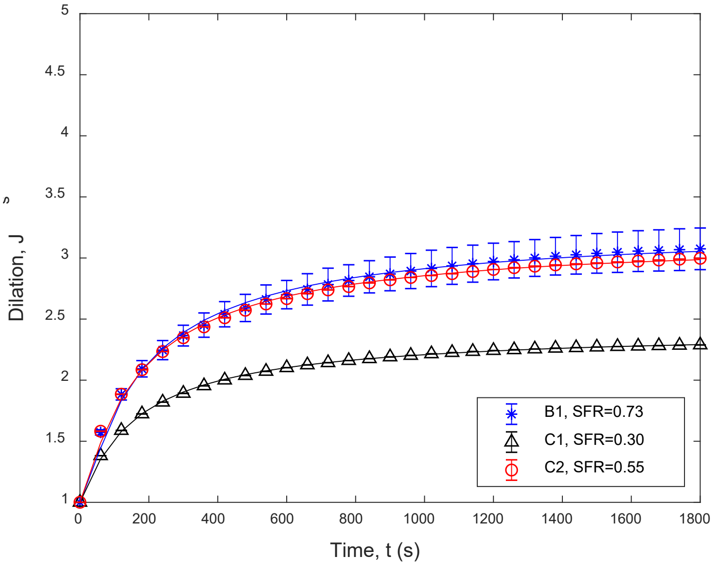

Figure 3.6. Swelling-induced dilation along the test for the samples B1, C1 and C2. Best-fit plots according to equations in Chapter 2 are reported for comparison.

The values of sample thickness measured during the tests and reported as dilation (J^s) are reported in Figure 3-5 and in in Figure 3-6 as a function of time. The time-resolved profiles of J^s were used to fit the two kinetic parameters (τ and m^s_{2max}), in agreement with the dilation equation of the Diersch's Model reported in Chapter 2,once the relation between porosity and swelling ratio is set. At the same time, the hydraulic conductivity can be calculated as a function of time and, in turn, of swelling ratio according to the equation reported in Chapter 2. The best-fit parameters of absorption kinetics and hydraulic conductivity are reported in Table 3-4. It is worth to note that, although the same SAP particles are used in every composite material, different composites show different swelling kinetics. This is probably due to the nature and extent of physical interaction between the fibres and the SAP particles in the composite material [55]. In other words, the confining pressure exerted by the fluff on SAP particles may vary with the different fluff bulk concentrations.

Overall, the fitting kinetic parameters found for the different samples are fairly similar to each other, as one would expect considering that the different composite materials are made of the same components at different concentrations. The averaged values for the kinetic coefficient and the maximum swelling ratio are 5.01 ± 0.43 s and 37.1 ± 2.2 respectively, with a confidence interval of 95%. Figure 3-5 and Figure 3-6 also show the best-fit plots using parameters in Table 3-3. The good agreement between model curves and experimental results confirms the soundness of the model equations.

Analysis of Figure 3-7 and Figure 3-8 indicates that the equation used to fit the hydraulic conductivity data works reasonably well to model the decrease of hydraulic conductivity with volumetric strain, i.e. with swelling ratio, for the different composite materials investigated. Similar to what happens with porosity, the reduction of hydraulic conductivity is more pronounced for composite materials with larger SAP content.

Table 3.4. Values of the fitting parameters for the hydraulic conductivity model and the absorption kinetics (see Chapter 2) for the investigated materials.

Composite label	K_0 **(m/s)**	K_1	K_2	m^s_{2max}	τ **(s)**
OFF1	≈1E-3	–	–	–	–
OFF2	≈1E-3	–	–	–	–
A1	3.0E-04	0.78	2.79	38.6	4.92
A2	2.7E-04	1.15	2.47	42.2	5.22
A3	2.5E-04	1.39	2.59	39.8	4.62
A4	1.5E-04	2.24	2.30	34.1	6.32
B1	2.0E-04	1.02	2.70	34.0	4.72
C1	3.4E-04	1.10	2.30	34.4	4.88
C2	2.9E-04	1.41	2.57	36.8	4.41

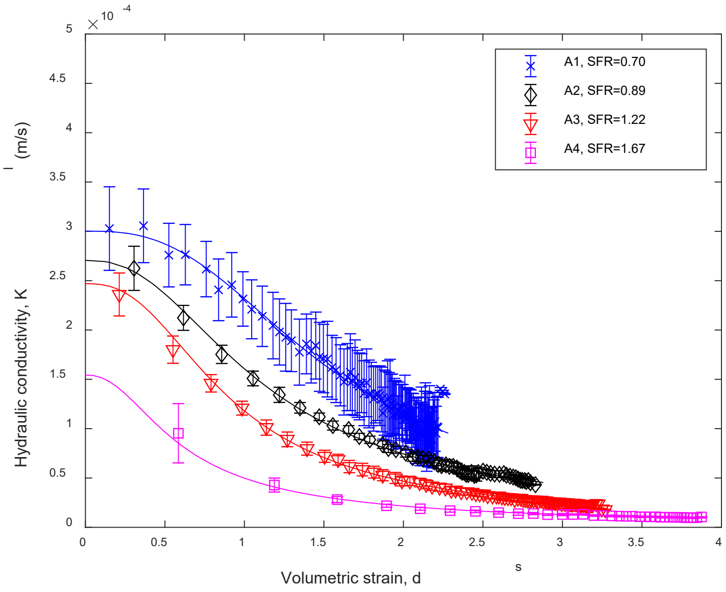

Figure 3.7. Hydraulic conductivity for the samples A1, A2, A3 and A4. Best-fit plots according to equations in Chapter 2 are reported for comparison.

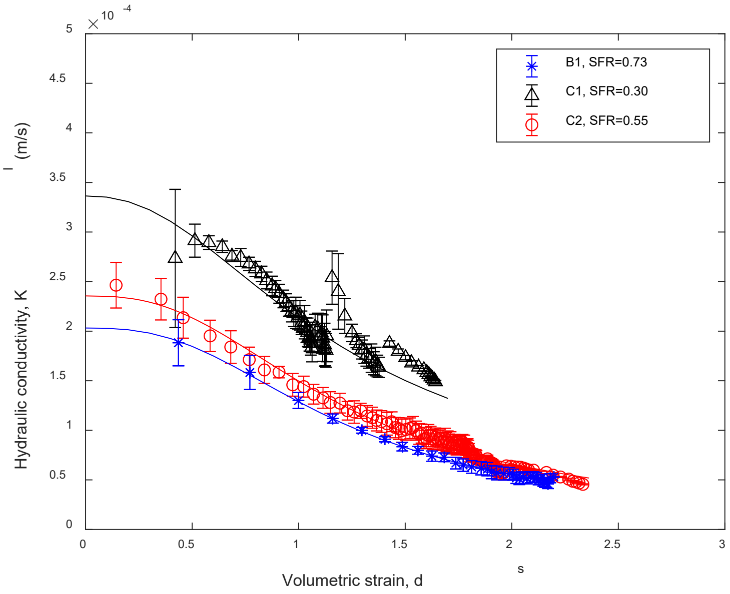

Figure 3.8. Hydraulic conductivity for the samples B1, C1 and C2. Best-fit plots according to equations in Chapter 2 are reported for comparison.

An interesting and useful result is obtained as hydraulic conductivity and porosity are cross-correlated with each other, as shown in Figure 3-9. Inspection of the figure suggests that once hydraulic conductivity is correlated with porosity, data points collapse into a fairly narrow band (with some departure in the range of large porosities where determination of hydraulic conductivity is less accurate) suggesting that, for different combinations of SFR and swelling ratio of SAP particles, hydraulic conductivity of the porous system is inherently related to porosity. The only significant departure is exhibited by sample A4: for this sample, which is characterized by a fairly large value of SFR, early "blockage" of the porous network and lack of hydraulic conductivity is displayed already at porosities in the order of 0.5.

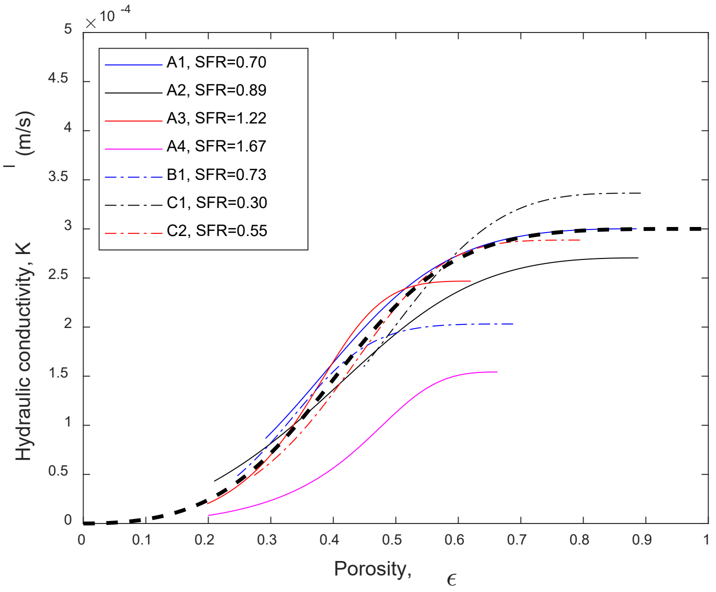

Figure 3.9. Hydraulic properties vs porosity plot for the different composite materials.

Accordingly, a "master curve" relating hydraulic conductivity to porosity has been obtained by statistical inference over all the data, reported in Figure 3-9, expressed by the equation:

$$K^l = \frac{K_0 \varepsilon^2}{\varepsilon^2 + (1-\varepsilon)^{3.5}}, \tag{3.4}$$

where $K_0 = 3.0 \times 10^{-4}\ m/s$. The shape of the implemented function is the LET-correlation proposed in literature for describing the relative permeability of porous media [52], with $\{L, E, T\} = \{2,1,3.5\}$. The hydraulic conductivity depends on the porosity of the system, which in turn depends on the liquid uptake of the sample.

3.3. RETENTION

Pressure–saturation curves were obtained to evaluate the parameters of van Genuchten model, according to the following experimental procedure using the test arrangement outlined in Figure 3-10. A cylindrical sample of 6 cm diameter, laterally confined and compressed at 0.3 psi, was placed on a glass porous plate welded into a glass funnel. The funnel was connected to a liquid reservoir placed on a mass scale. Two saline solutions were used (0.9% and 25% basis weight), yielding widely different values of the swelling ratio. As the plate was moved up and down, a different value of the pressure head was achieved on the upper surface of the glass plate, which kept fluid continuity with the reservoir because of the high capillary forces inside pores. It was assumed that the whole sample laid on the glass plate was at the same pressure head. The amount of liquid exchanged between the reservoir and the sample was measured by the mass scale and imbibition and drainage curves were obtained.

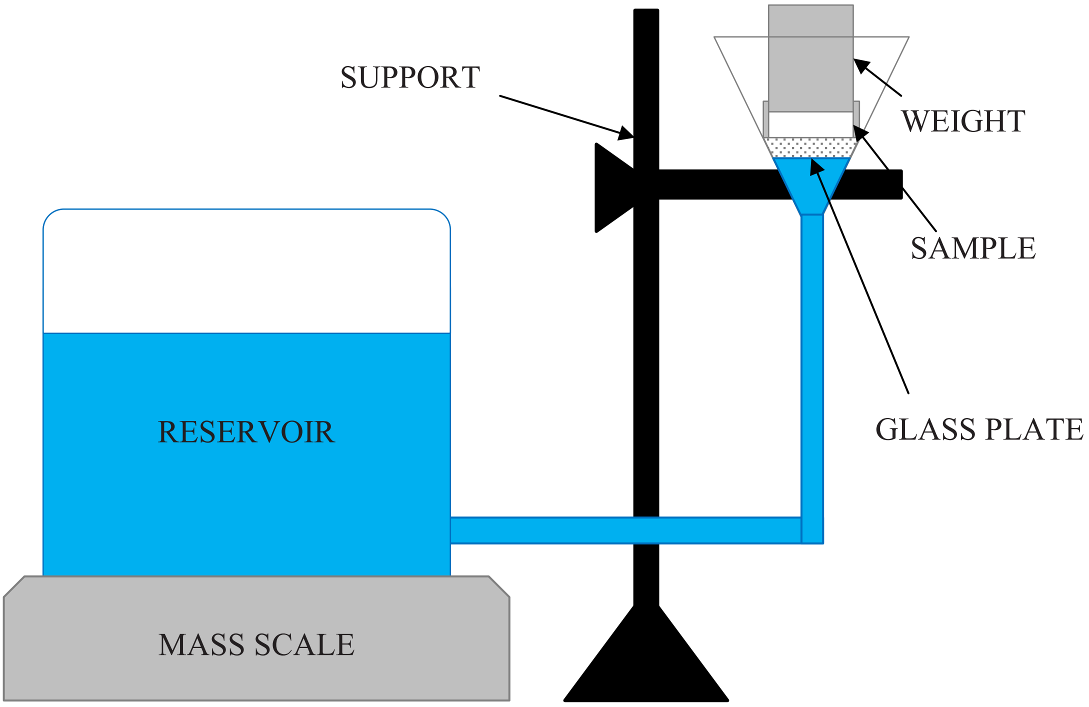

Figure 3.10. Outline of the experimental apparatus for the retention model characterization.

First, the weight of the dry sample was measured (W_1). Then, the sample was kept wet on the glass plate at a constant pressure head of 0 until a steady state established. The amount of brine passed into the sample was recorded by the mass scale, and the weight of the swollen wet sample at 0 pressure head can be measured (W_2). In the first stage of the experiment, the pressure head was varied, and sample weights were recorded while keeping the sample at different levels above the free surface of the liquid reservoir. After the last measurement, the thickness of the sample (h) was measured. Then, it was drained for 10 minutes using a vacuum pump and blotted with filter paper for 10 minutes, adding additional compression at 1.5 psi. Then, it was weighted again (W_3), to get a value of the amount of liquid drained from the sample. In the second stage of the experiment, the drained sample was placed on the glass plate again, to investigate the imbibition behaviour. The plate was gradually brought to the same level as the free surface of the liquid reservoir and weights at every step were recorded, with a procedure similar to that of the first stage.

The amount of liquid in the sample was calculated and correlated with the sample porosity. The latter is calculated according to:

$$\varepsilon = \frac{\frac{W_2 - W_3}{\rho^l}}{h\pi\frac{d^2}{4}}. \tag{3.5}$$

The swelling ratio of the sample was computed from the weight measurement performed after the drying process:

$$m_2^s = \frac{W_3 - W_1 - 0.8\bar{C}^s_{FL_0} h\pi\frac{d^2}{4}}{\bar{C}^s_{SAP_0} h\pi\frac{d^2}{4}}. \tag{3.6}$$

The saturation level was determined as:

$$s^l{}_i - s^l{}_{i-1} = \frac{\frac{W_{i-1} - W_i}{\rho^l}}{\varepsilon h\pi\frac{d^2}{4}}, \tag{3.7}$$

from the measured weight, once the porosity, the bulk volume of the sample and the density of the saline solution was known. Subscripts i and $i-1$ in eq. 6 refer to the current and the previous steps during the evaluation of the saturation curve and W is the weight recorded on the mass scale. Evaluation of saturation curves is a time-consuming process because each step corresponds to a steady state condition. Thus, for a preliminary estimation of the time needed to approach the steady state at every pressure head, saturation curves during time were evaluated. During the drainage process, at low pressure head, the steady state is reached almost immediately, with low data dispersion. As the pressure head decreases, the time necessary to achieve the steady state increases (10-20 min). Conversely, during the imbibition, more time is needed to reach the steady state at each value of the pressure head (15-30 min).

Table 3.5. Values of the fitting parameters for the van Genuchten model (Chapter 2) for the tested samples. Results are averaged on different swelling ratio.

Composite label	**Salinity at $0.9\%_w$**		**Salinity at $25\%_w$**		
	$\boldsymbol{\alpha}$ (m^{-1}) (drying)	$\boldsymbol{\alpha}$ (m^{-1}) (wetting)	$\boldsymbol{\alpha}$ (m^{-1}) (drying)	$\boldsymbol{\alpha}$ (m^{-1}) (wetting)	$\boldsymbol{n}$ (-)
OFF1	3.75	12.95	–	–	4.23
OFF2	3.61	11.95	–	–	3.27
A1	4.85	17.21	4.66	13.10	3.22
A2	4.91	18.30	3.37	13.61	3.12
B1	4.43	13.76	3.76	12.22	3.18
C1	3.45	16.51	4.37	11.73	3.28
C2	4.60	11.07	3.99	11.82	3.03

Figure 3-11, Figure 3-12 and Figure 3-13 show saturation data as a function of pressure head for some of the composite materials investigated. Two brines with different salinity (0.9%$_w$ and 25%$_w$) were used to perform pressure–saturation measurements at very high and very low swelling ratios of SAP particles. Pressure–saturation curves for materials without SAP particles (OFF1 and OFF2) were also scrutinized. As it can be seen in Table 3-5, OFF1 and OFF2 pads have similar fluff base weight as A and D samples blended with SAP particles, respectively. The van Genuchten model (Chapter 2) was used to fit experimental values. The fitting parameters of the model are reported in Table 3-5 and the corresponding curves are plotted in the Figure 3-11, Figure 3-12 and Figure 3-13.

From the analysis of the Figure 3-11, Figure 3-12 and Figure 3-13, it can be observed:

- the curves and the values of the parameters of van Genuchten model for all the composite materials are comparable confirming the validity of the model used;
- despite the expectation [4,17] comparing the results obtained with different salinity, the retention model seems to be only slightly influenced by swelling of SAP particles for all the investigated composite materials. This statement is in contrast with the equation proposed by Diersch for the retention model, in which van Genuchten parameters are expressed as a function of the swelling ratio;
- capillary pressure–saturation curves for composite materials (Figure 3-11 and Figure 3-12) and for materials without SAP particles are very similar (Figure 3-13).

On the whole, it is very likely that fibrous structure of the composite material governs capillary phenomena. As the capillary pressure–saturation curves are strictly related to fluff bulk concentration, no strong differences arise among samples investigated with the same brine (plots of Figure 3-11 and Figure 3-12), despite of the change of SAP content. As a matter of fact, retention model for a fibre made material is significantly different from a granular one: the path of water spreading inside a fibrous material probably follows the fibres network, giving rise to a fingering displacement of liquid [31] and letting the liquid to fill disconnected pores. However, even if a dye is used to trace the fluid in porous medium, it is difficult to associate a saturation level to an intensity of the resulted stain on the AHP and recognize the path of the liquid. It is likely that slight differences to this transport mechanism can occur decreasing brine salinity though the porosity of the composite materials is reduced by the swelling of SAP particles. To sum up, even if the SAP particles reach their maximum size, the fibres probably provide enough connectivity for the porous matrix, strongly contributing to the retention phenomena of the whole composite material.

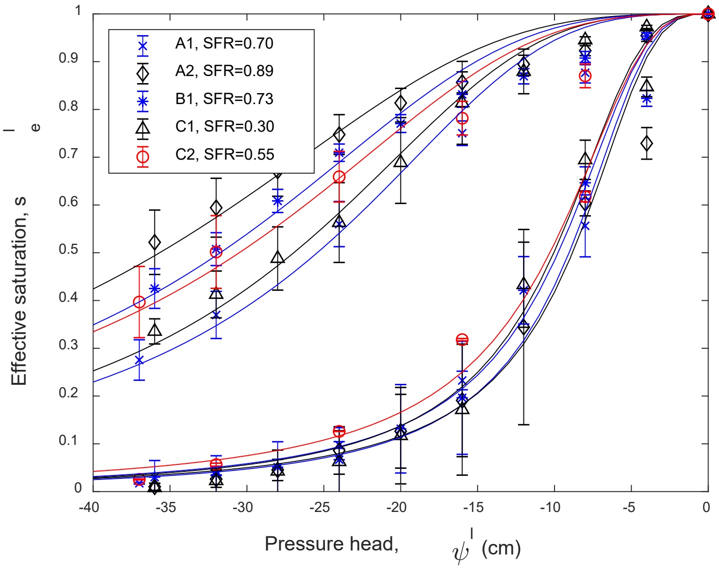

Figure 3.11. The retention pattern for samples with different base formulation. Bars represent standard deviations of the experimental measurements. Solid lines are the best-fit pressure–saturation curves according to the van Genuchten model (Chapter 2). Data points with 0.9%$_w$ salinity.

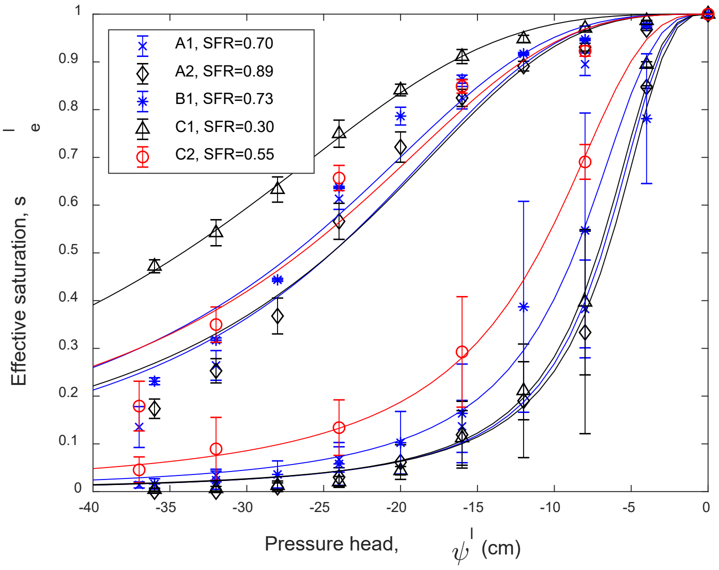

Figure 3.12. The retention pattern for samples with different base formulation. Bars represent standard deviations of the experimental measurements. Solid lines are the best-fit pressure–saturation curves according to the van Genuchten model (Chapter 2). Data points with 25%$_w$ salinity.

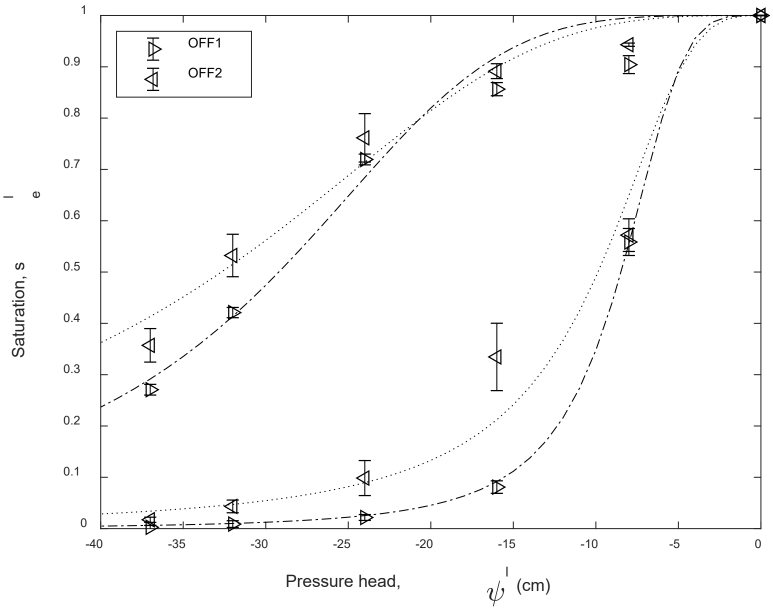

Figure 3.13. The retention pattern for composite materials without SAP (0.9%$_w$ salinity). Bars represent standard deviations of the experimental measurements. Lines are the best-fit pressure–saturation curves according to the van Genuchten model (Chapter 2).

3.4. PERFORMANCE TEST

To evaluate the performance of the materials during cycles of imbibition and drainage, rectangular pads (130 mm X 300 mm) were wet with consecutive gushes with 0.9% saline solution. The set-up of the experiment is shown in the Figure 3-14. The samples were compressed at 2068 Pa (0.3 psi), commonly considered as a typical pressure exerted by the human body on the AHP, with weights placed on a sheet of plexiglass (e.g. Buchholz et al., 2005 [55] applied 0.3, 0.6 and 0.9 psi on their samples, while Bae et al., 2018 [56] consider the pressure of an infant on the AHPs as 0.41 psi). In the middle of the sheet, a hole with a diameter of 37 mm allows to wet the upper surface of the sample. In correspondence of the hole, a plexiglass cylinder is placed and a relatively large amount of saline solution (80 mL) was pumped to wet the sample from above. When the column of water inside the cylinder was emptied, the gush was considered ended. After 5 min of drainage, another gush was carried out in the same condition. The test is concluded after 4 gushes. The acquisition times are defined as the times elapsed after the column of water is emptied, for each gush. They were recorded at each gush. For two different types of composite materials (A1 and D2), samples after every cycle were cut and dissected. The pieces were weighted to map the distribution of water inside the pad. This test was used as a benchmark for the model, comparing experimental data with results from simulations.

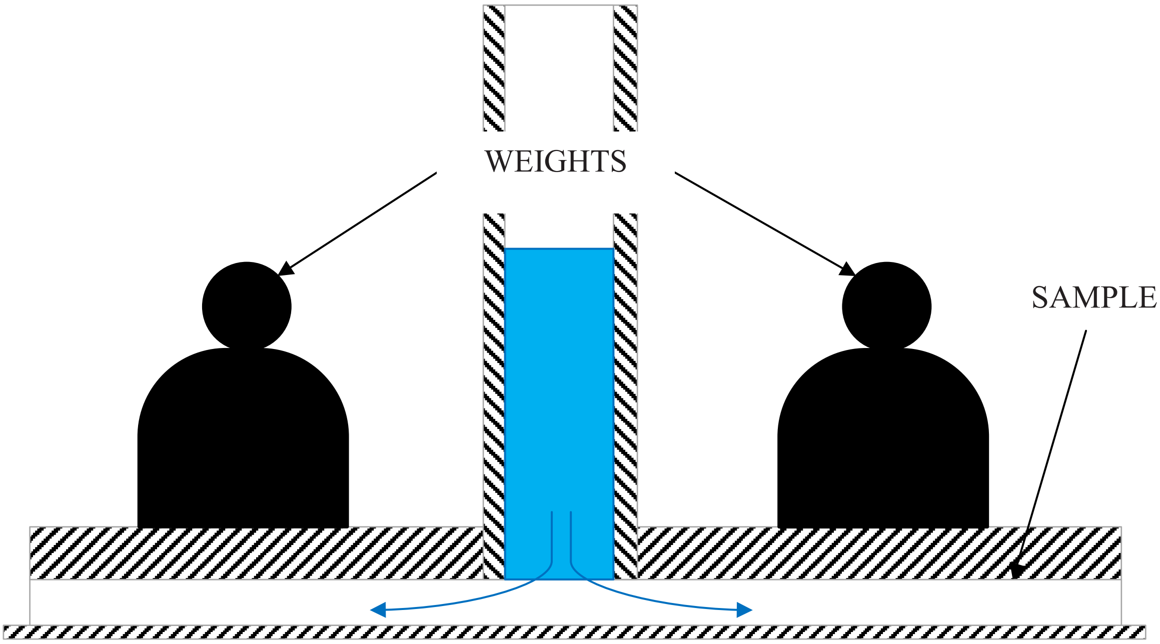

Figure 3.14. Sketch of the experimental apparatus used to evaluate performances of the composite materials.

The acquisition times obtained following the previously described experimental procedure are reported in Table 3-6. Several tests were carried out for each material to increase the reliability of the experimental results. Samples with high SAP content exhibit large variability in terms of acquisition times.

For the sample labelled A4, it was not possible to reproduce 4 gushes of 80 mL each, because of the blockage of the experiment due to the steep decrease of hydraulic conductivity after the first gush. This phenomenon occurs when the polymer particles grow adjacent each other and being deformable can occupy all the available void space, thus, irremediably obstructing the flow of liquid. The results for this composite material will not be considered any further..

Table 3.6. The acquisition times measured for the different composite materials during the four gushes. Acq. time is the experimental averaged acquisition time, while S.D. is the standard deviation of the measurement.

	1st gush		**2nd gush**		**3rd gush**		**4th gush**	
	Acq. time (s)	S.D. (s)	Acq. time (s)	S.D. (s)	Acq. time (s)	S.D. (s)	Acq. time (s)	S.D. (s)
A1	27.0	5.1	183.4	32.9	272.9	36.8	316.7	42.2
A2	31.7	9.3	250.1	23.5	393.1	63.1	463.1	103.4
A3	29.0	1.0	296.3	36.9	827.3	115.9	1073.3	135.9
A4	-	-	-	-	-	-	-	-
B1	19.0	2.5	198.0	32.3	443.8	144.4	560.5	164.6
C1	13.0	1.1	61.1	10.1	92.1	11.0	110.8	10.0
C2	17.3	1.1	119.5	9.0	167.1	16.5	182.5	25.8

The acquisition times increase with the number of the gushes, as expected, due to the decreasing of porosity and permeability of the increasingly swollen composite material. For a given fluff basis weight, an increase in SAP content determines an increase of the acquisition time, for each gush considered. However, the SFR does not seem to be the only relevant parameter, as the A1 and B1 composite materials have almost the same SFR but different acquisition times. Moreover, the larger is the SAP content inside the sample, the higher is the standard deviation of the acquisition times, which are also quite large and corresponds to a blockage of the fluxes. That seems evident for A3 and B1, in which the order of magnitude of the standard deviation and the measured value is comparable. However, from preliminary experiments carried out in the previous Chapter, neither of the two materials nor the A4 have shown a blockage during the hydraulic conductivity test, even though the fluxes are steeply reduced with time. Therefore, the same material shows different hydraulic properties between the two tests because of the different experimental conditions: not only during the hydraulic test is the sample always saturated, but also the head of water is constant in time. That means that also on the surface of the SAP particles the hydraulic pressure is constant with time. Conversely, during the performance test the pressure of the water is continuously changing as the phases of imbibition and drainage follow one another. Moreover, during the imbibition phase the liquid pressure decreases as the water fills the sample, while during the drainage the saturation is below 1 and the pressure head is negative. So, the hydraulic pressure on the surface of the SAP particles in the performance test is lower than the stress pressure exerted by the water during the hydraulic conductivity test, and this effect can bring to unpredicted or inhomogeneous swelling of the particles, and a consequentially decrease in the hydraulic conductivity of the sample.

3.5. COMMENTS ON THE EXPERIMENTAL OUTCOMES

The set up and application of a comprehensive experimental protocol for the characterization of properties and constitutive parameters of absorbent hygiene products (AHP) relevant to their performance have been described. The protocol is based on a combination of experimental methods for the assessment of liquid absorption rate, porosity, hydraulic conductivity, retention model, swelling. The experimental methods are tailored so as to meet the peculiar nature of AHP and overcome some limitations of general-purpose methods for the characterization of porous media. In the end, the performance test was set up to create a benchmark for future simulation and to test the model in unsaturated conditions. Regarding the performance test, a remarkable feature of the experimental results is the increasing standard deviation with increasing SFR, a feature that reflects the larger degree of sample inhomogeneity associated with larger contents of SAP.

Properties of the composite media may be affected by the amount of the single components (extensive properties), or by the relative amount of fluff and SAP, expressed by the polymer-to-fluff ratio SFR (intensive properties). The fluff content in the base formulation dictates the initial thickness of the layer, an extensive property that affects bulk concentrations. The initial thickness of the pad is not affected by SFR. The SFR has a strong effect on the development of porosity and dilation along with imbibition and liquid absorption. The initial value of the porosity is determined by the initial thickness of the sample, but larger SFR bring about a steeper decrease of the porosity and faster and more extensive dilation of the samples. Notably, curves representing different composite materials with similar SFRs can be easily superimposed, underlining the fact that porosity and dilation are both intensive properties related to each other. Hydraulic conductivity depends on liquid absorption and swelling in a way that is critically affected by SFR. A remarkable finding is that, once the hydraulic conductivity is expressed as a function of the porosity of the sample, a single “master curve” is established. This feature suggests that hydraulic conductivity is an inherent property of a porous medium of given porosity, for any combination of sample base formulation and liquid uptake. This is certainly true for the studied material. However, out of the observed range of SFR, there may be conditions in which porosity is more influenced by other variables. The hydraulic conductivity model was effectively validated by comparison of experimental data with results of simulation carried out under saturated conditions. Pressure–saturation curves are barely influenced by the liquid absorption and associated swelling of the SAP particles. Capillary phenomena are essentially governed by the fluff matrix, so that the liquid is driven along fibres before filling empty pores. An important consequence of this phenomenon is that no pore is plugged regardless of the swelling extent of the SAP particles, and that the size of the pores between the fibres and the particles affects capillary phenomena to a very limited extent. Relative permeability was not considered in experimental activities. Following several examples in literature of relative permeability models in fibrous materials [4], a power law of liquid saturation was used. Results of the experimental characterization of composite media provided reliable input parameters and constitutive equations for application to continuum dynamic modelling of AHP imbibition/drainage, reported in Chapter 4.

4. FEM MODELLING

Computations based on the model were performed using the COMSOL Multiphysics® software [57], a FEM solver. The primary variables solved are the pressure head (ψ^l), the swelling ratio (m_2^s) and the displacement (u^s), and they are solved with a segregated scheme. A moving mesh module is implemented, in order to handle the parallel occurrence of solid deformation. In Table 4-1 a sum up of the measured properties for the different samples is reported.

Table 4.1. Model parameters used in the simulations. Samples labelled with the same letter have the same basis weight of fluff, in ascending order of alphabetical order.

		Samples						
Parameter	**Description**	**A1**	**A2**	**A3**	**A4**	**B1**	**C1**	**C2**
α_w	Retention model parameter (pure imbibition curve) (m^{-1})	15.2	16.0	15.6	15.6	13.0	14.1	11.4
α_d	Retention model parameter (pure drainage curve) (m^{-1})	4.8	4.1	4.5	4.5	4.1	3.9	4.3
δ	Relative permeability parameter	3 – 4	3 – 4	3 – 4	3 – 4	3 – 4	3 – 4	3 – 4
ε_0	Initial porosity	0.89	0.89	0.89	0.87	0.89	0.89	0.89
ε_1	Porosity model parameter	0.11	0.13	0.47	0.63	0.27	0.11	0.18
ε_2	Porosity model parameter	1.03	1.09	0.70	0.66	0.80	0.71	0.84
τ	Absorption characteristic time (s)	4.92	5.22	4.62	6.32	4.72	4.88	4.41
h_0	Initial thickness (mm)	3.31	3.72	4.22	4.22	5.32	5.67	6.19
K_0	Hydraulic conductivity parameter (m/s)	3E-4	3E-4	3E-4	3E-4	3E-4	3E-4	3E-4
m^s_{2max}	Maximum swelling ratio	38.6	42.2	39.8	34.1	34.0	34.4	36.8
n	Retention model parameter	3.2	3.1	3.2	3.2	3.2	3.3	3.0
s^l_{max}	Maximum value for saturation	1	1	1	1	1	1	1
s^l_{min}	Minimum value for saturation	0	0	0	0	0	0	0
SFR	SAP/fluff ratio	0.70	0.89	1.22	1.67	0.73	0.30	0.55

4.1. TESTING OF THE HYDRAULIC CONDUCTIVITY MODEL

Permeability and hydraulic conductivity are no doubt the most relevant properties to define the flow dynamics across the porous material. When a single fluid (e.g. water) is considered, conductivity and permeability coincide. If the porous matrix is filled with immiscible non-compenetrating fluids, (e.g. water/oil or water/air), the conductivity related to one of the fluids might be decreased by the interactions with the other, depending on saturation of the pores. In such a composite scheme, predicted flows in a multiphase system are inherently more difficult to compare with experimental results. In order to estimate the quality of the measurements, a preliminary validation of the hydraulic conductivity model in saturated conditions was performed.

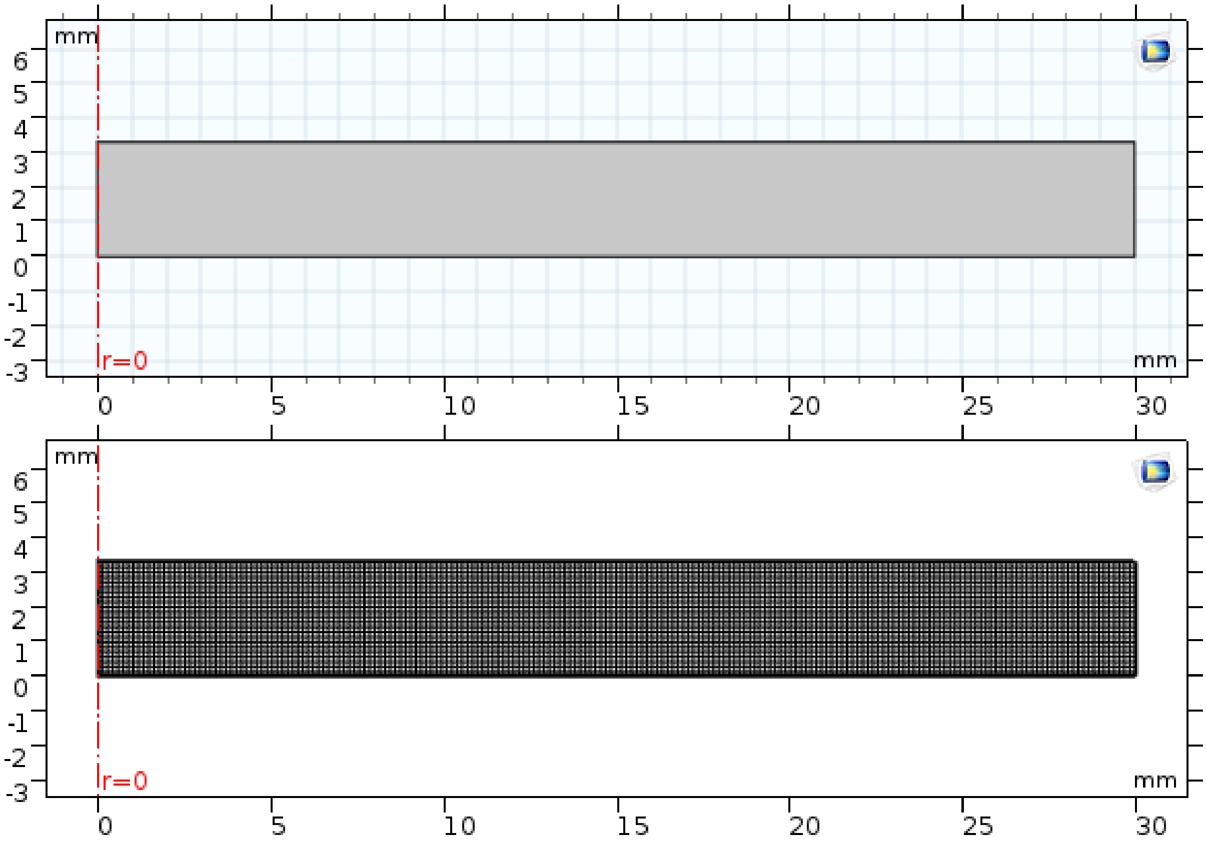

Figure 4.1. The axial symmetric domain and its discretization used to perform simulations of hydraulic conductivity test (Chapter 3). In this image is shown the initial geometry of the A1.

Time dependent simulations in 3D domains were carried out, so as to reproduce the experimental conditions established in the assessment of hydraulic conductivity, described in 3.2. In order to reduce the computational effort, axial symmetry of the computational domain was assumed, as shown in Figure 4-1. The size of the cells of the structured mesh is about 125 mm^2 with a number of elements between 2400 and 4800, depending on the initial thickness of the different composite materials. To handle mesh modifications along the simulation, the Moving Mesh module is used, by defining the displacement of the mesh as reported in (2.8) [57]. Fluxes across the surfaces are calculated through a boundary integral evaluation. The pressure head on the top boundary of the sample was set at the constant value of 5 cm, while it was set at 0 on the bottom boundary. The left boundary is the axis of symmetry, while on the right boundary a no flux condition was set. To reduce the errors in mass balance that can occur using FEM algorithms [25,58], the spatial discretization of the elements is quadratic. The PDEs system is then solved with a direct linear system solver (MUMPS), using a fully coupled approach, simultaneously solving the mesh deformation and the domain variables.

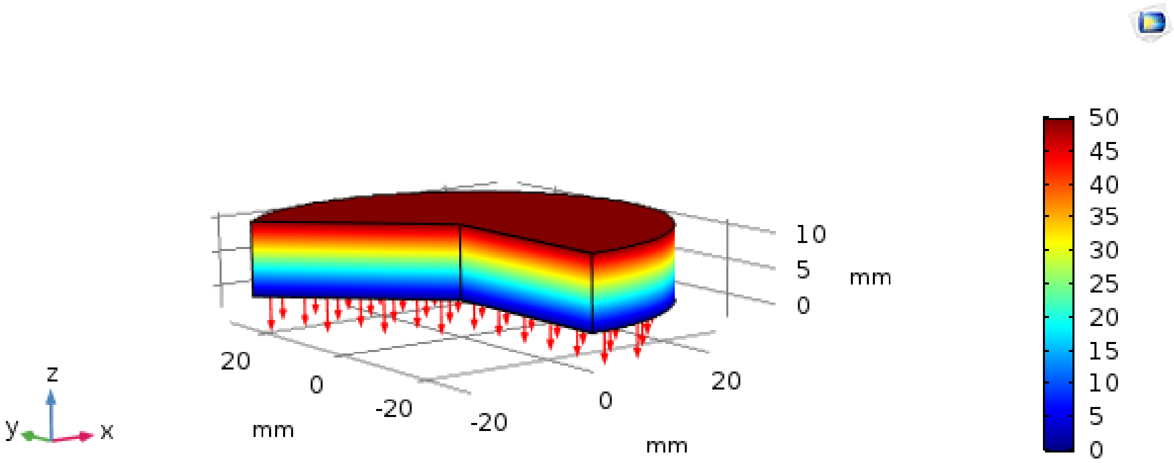

Figure 4.2. Final time step of the numerical simulation of the hydraulic conductivity test (Chapter 3) for A1. In rainbow scale the pressure head is expressed in millimetres. Flows through the sample are shown with red arrows.

The initialization of the pressure head for the points of the domain is linear, from 0 to 5 cm along the vertical axis, in order to have fully saturated condition at the initial time step. With these initial and boundary conditions, the sample remains fully saturated along the simulation, in agreement with the experimental setup.

The predicted fluxes across the sample have been compared with the experimental values. A preliminary check on the accuracy of the evaluation of the fluxes at the boundary was conducted, by recording the difference between inlet and outlet compared with the sink term in the liquid mass balance differential equation (Figure 4-3). The two curves are perfectly superimposed, showing a good accuracy of the numerical solution. In the same figure, the horizontal line represents the null flux across the lateral boundary.

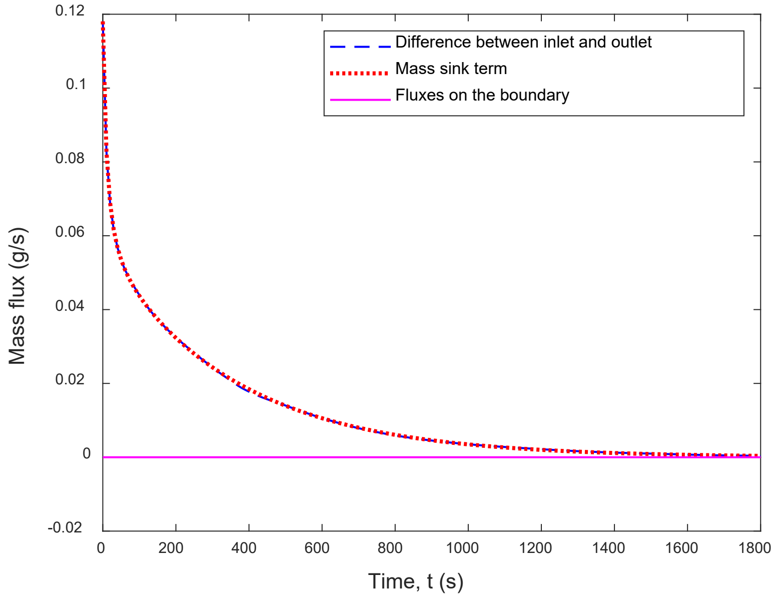

Figure 4.3. Evaluation of fluxes across the A1 sample for the simulation of the hydraulic conductivity test (Chapter 3).

Figure 4-4 and Figure 4-5 reports the computed and experimental values of the mass of liquid flowing across the sample for all the materials tested. The agreement between simulation and experimental data is good, with limited departures observed in the early stage and excellent agreement in the long term.

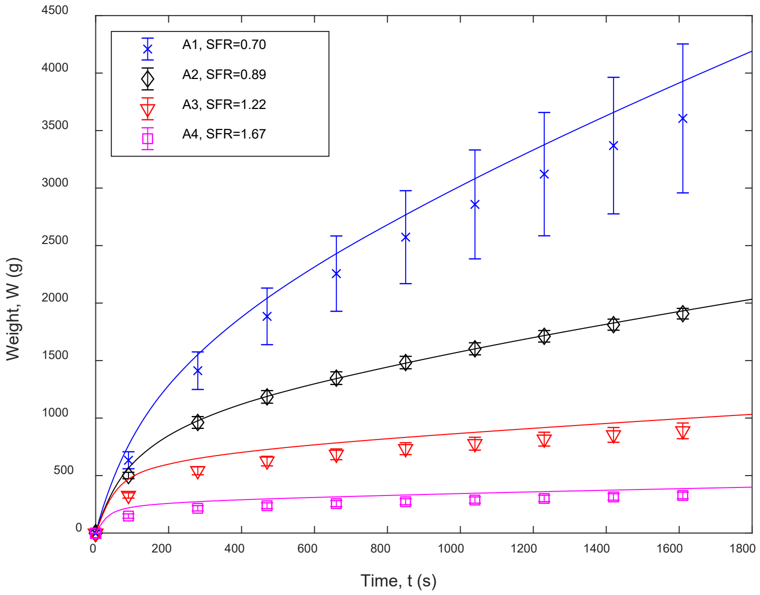

Figure 4.4. Cumulative amount of water flowing across the pad for the samples A1, A2, A3 and A4. Scatter plot refer to experimental data (error bars indicate standard deviation). Solid lines represent results of numerical simulations.

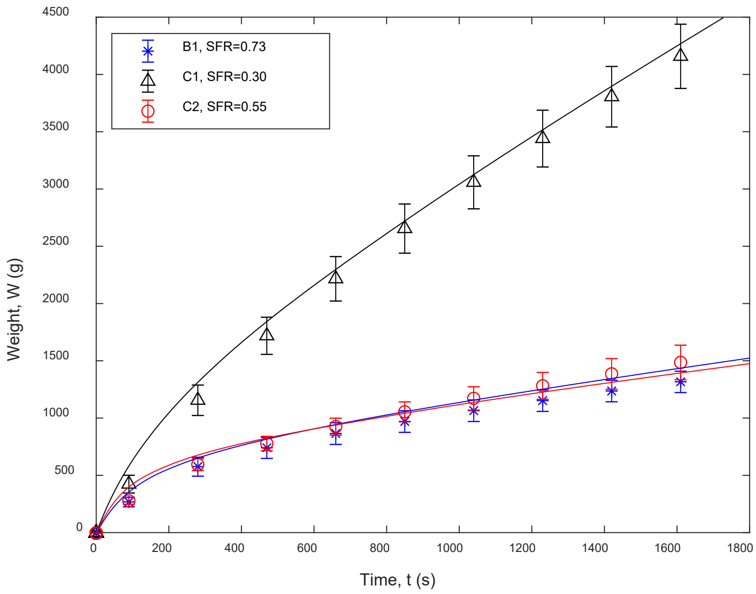

Figure 4.5. Cumulative amount of water flowing across the pad for the samples B1, C1 and C2. Scatter plot refer to experimental data (error bars indicate standard deviation). Solid lines represent results of numerical simulations.

4.2. PERFORMANCE TEST SIMULATION

The domain considered is a 3D domain, representing only a quarter of the whole sample, according to a symmetry argument. The samples investigated have different initial thicknesses (Table 4-1). The initial pressure head value is set at -1 m, to have a very low saturation inside the sample at the first time-step, while the initial swelling ratio was set at 0, in every point of the domain.

Regarding the boundary conditions, no-flow conditions were imposed on the boundaries, except for the circular imbibition zone. On that boundary a Dirichlet condition depending on time was set, to reproduce the weight of the emptying water column above the surface. Due to convergence issues, the pressure head value on the imbibition zone changes with a step function, and the pressure head varies in the first second from the initial condition value (-1 m at the beginning of the first imbibition) to the nominal value (the height of the water column after 1 s). Moreover, the Dirichlet condition depends on time: the pressure head is calculated subtracting from the weight of the water column the mass of water inside the sample at every time step. Finally, this boundary condition automatically switches in a no-flow condition when the water column is empty, that means at pressure head of 0.

The mesh represented in Figure 4-6 is initially compressed and the quality of the mesh at the beginning of the simulation is intentionally smaller than the highest possible one. In this way, during the dilation of the sample, the quality of the mesh increases without going under an imposed threshold value, and the simulation appears to be relatively stable. Regeneration of the mesh was avoided, with a consistent decrease of computational effort. The elements are generated by extrusion from the horizontal surface, on which a triangular mesh was used. On the thickness dimension, the number of elements were varied from to 3 to 5, to maintain a proper quality of the mesh during the whole simulation, depending on the maximum dilation expected from the sample.

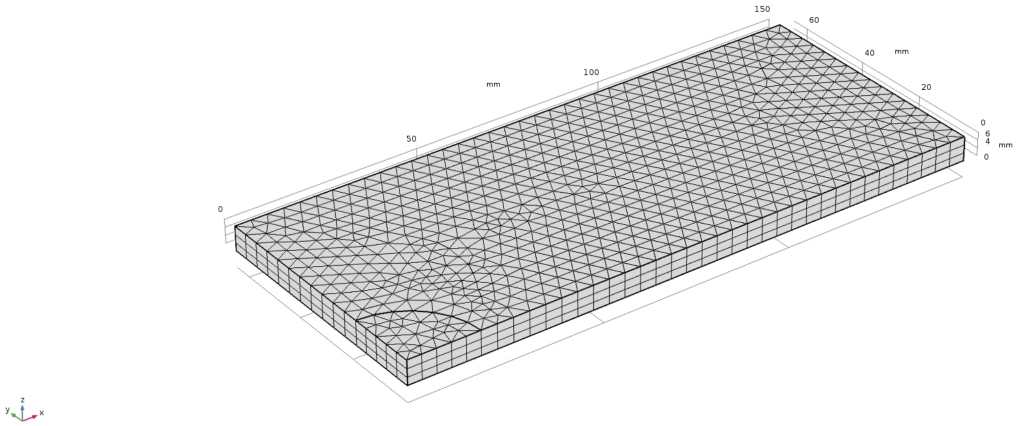

Figure 4.6. The mesh used during the numerical simulations of the performance test (Chapter 3). Elements on the z-axis are generated by extrusion from the triangular mesh on the top horizontal plane.

4.3. SIMULATION RESULTS

Figure 4-7 reports the acquisition times computed from the simulation model referred to the sequence of gushes. Computations were performed with two values (3 and 4) of the exponent of the relative permeability sub-model. Results from model computations are compared with acquisition times obtained in experiments.

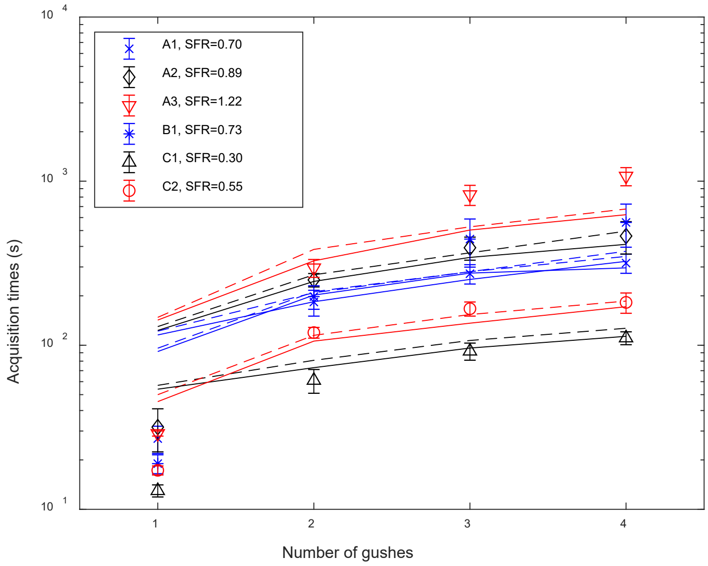

Figure 4.7. Comparison of the experimental and the numerical results for the performance test (Chapter 3), varying the relative permeability model (Chapter 2). The solid and the dashed lines refer to $\delta = 3$ *and* $\delta = 4$*, respectively.*

The acquisition times for the first gush for each composite material varied between 10 and 40 s, with no significant differences between the investigated materials. However, numerical results of the simulations did not predict the values for the acquisition times at the first gush. Different speculations can be done to justify the discrepancy between numerical and real tests for the first gush. A certain grade of uncertainty might be related to the assumption made in measuring the initial thickness and the initial properties of the sample: the numerical simulations consider as the initial condition a wet and not swollen composite material, in which the thickness and the hydraulic properties (porosity and conductivity) are far smaller than those of the dry initial sample. Another possible reason to explain this discrepancy is that for the first gush finite-size scaling effects have to be included in the model to appropriately represent a very small layer (geometrically thin) as a continuum. The acquisition times provided by the simulations for the subsequent gushes show a good agreement with the experimental test. It should be noted that the prediction is considerably less accurate for those materials that showed great variability during the experiments (A3 and B1).

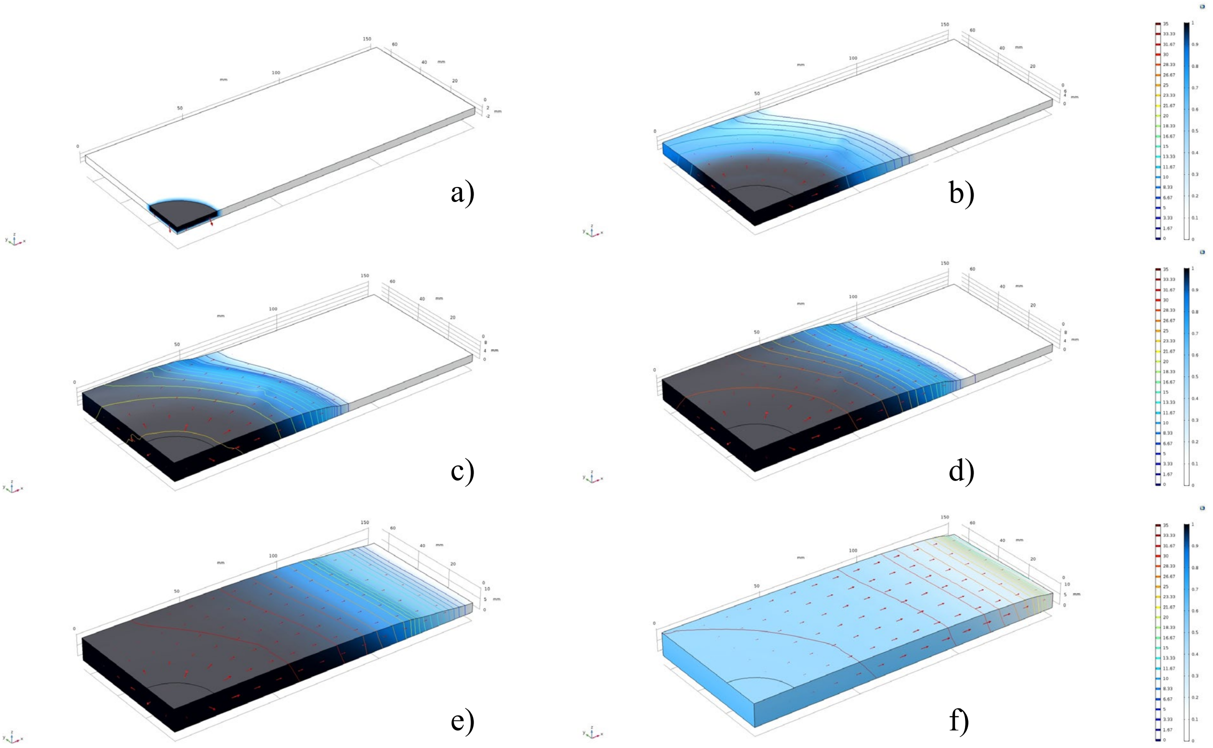

Figure 4.8. Snapshots from numerical simulation of the performance test (Chapter 3) of the A1. Saturation is expressed in shadows of blue and the contours represent the swelling ratio. a) After 1 s from the start of the first gush; b) End of the first gush; c) After 100 s from the start of the second gush; d) After 150 s from the start of the third gush; e) After 350 s from the start of the fourth gush; f) After 1000 s the end of the fourth gush.

Simulation results obtained with different exponents of the Brooks and Corey ($\delta = 3$ and $\delta = 4$) are compared in Table 4-2. Altogether results suggest that the model is fairly insensitive to this parameter of the relative permeability model.

Table 4.2. Simulated acquisition times for two different exponents of the Brooks and Corey model of the relative permeability (Chapter 2).

	$\boldsymbol{\delta = 3}$						$\boldsymbol{\delta = 4}$					
	A1	**A2**	**A3**	**B1**	**C1**	**C2**	**A1**	**A2**	**A3**	**B1**	**C1**	**C2**
1st gush (s)	116	123	142	92	54	45	122	130	148	96	57	50
2nd gush (s)	184	245	327	202	73	106	209	269	384	212	81	115
3rd gush (s)	252	343	504	275	96	136	281	366	527	281	107	154
4th gush (s)	325	412	625	296	113	172	348	496	677	374	127	186

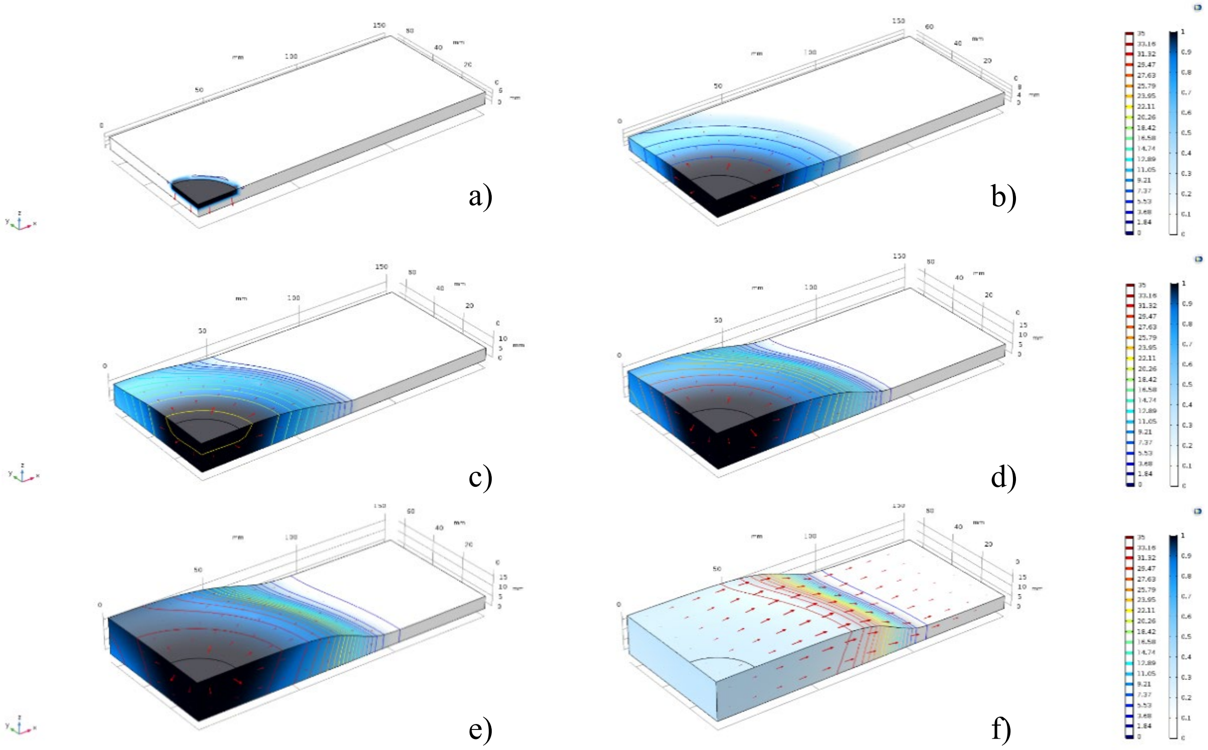

Figure 4.9. Snapshots from numerical simulation of the performance test (Chapter 3) of the C2. Saturation is expressed in shadows of blue and the contours represent the swelling ratio. a) After 1 s from the start of the first gush; b) End of the first gush; c) After 100 s from the start of the second gush; d) After 150 s from the start of the third gush; e) After 350 s from the start of the fourth gush; f) After 1000 s the end of the fourth gush.

In Figure 4-8 and in Figure 4-9, snapshots from the simulation of the thinnest and the thickest sample (A1 and C2, respectively) are reported, in order to better understand the phenomenology of imbibition. At $t = 1\ s$ (a), the liquid has not reached yet the bottom of both the samples and the main direction of the flow is vertical. At the end of the first imbibition (b), the inner circular zone is completely saturated, and the flow direction has gained a radial component. Moreover, the swelling ratio in the inner zone is between 25–35% of its maximum value and the domain does not appear strongly deformed. More the gushes, higher the swelling ratio and deformation of the inner zone of the sample (c–e). One thousand seconds after the fourth gush (f) the saturation of the inner zone is reduced, and the deformation is increased significantly. However, the A1 and C2 samples show significant differences in both final shape and residual saturation. The A1 sample surface is homogeneous flat, as an effect of the homogeneous swelling ratio trough the sample. The residual saturation is also quite large (more than 0.5) in the whole sample, and only a narrow zone nearest the opposite border from the imbibition zone (roughly 2 cm) is still absorbing liquid 1000 s after the end of the fourth imbibition. Conversely, the C2 sample surface exhibits a typical waveform, defining two zones with different average swelling ratio. Furthermore, the farthest portion from the inner zone of sample C2, wider (roughly 10 cm long) than that observed for sample A1, did not take part in the absorption process.

Distribution of liquid inside the samples was considered in order to further validate the model and compare simulated results with the experimental data. At every imbibition, the samples were cut, and the pieces were weighted. The measured weights were compared with the values from the simulations. Every quarter of the sample was divided in twelve pieces (one cut along the shorter dimension and 5 cuts along the longer dimension). As it can be observed from the figure, the pieces obtained have not the same dimensions. Only those parts far from the longest edge have been taken into consideration to avoid some possible boundary effects. Then, the resulting pieces have rectangular shape: 5 pieces of 3x2 cm^2 and 1 piece of 3x5 cm^2, as shown in Figure 4-10.

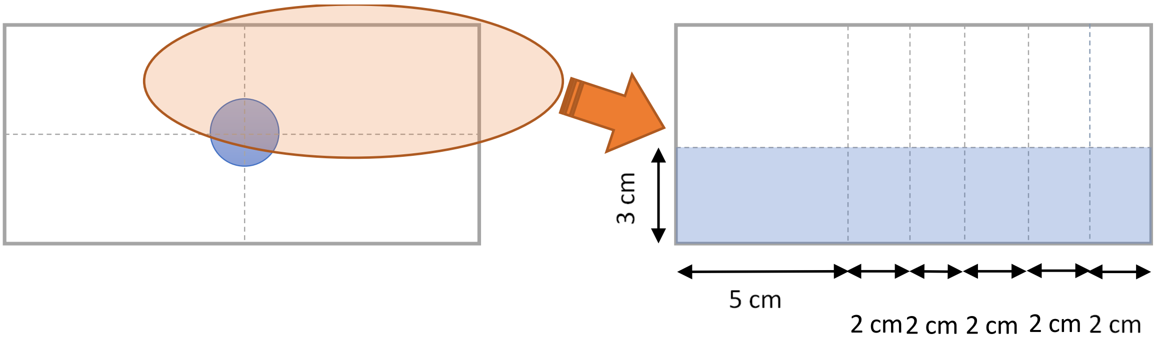

Figure 4.10. Sketch for the cuts done on the samples after the gushes during the performance test (Chapter 3). Only the weights of the blue rectangular pieces were considered in order to have a comparison between simulated and experimental results.

The basis weight of every piece was evaluated and compared with the predicted one by the simulation. The comparison is shown in Figure 4-12**,** in which the averages of four pieces from the different quarters of a single sample are reported. First, a good agreement with experimental measurement was achieved in terms of basis weight immediately under the imbibition zone (i.e. in the centre of the sample) and very far from it (i.e. near the edges of the samples). However, transitions between the highly wet zones and the almost dry ones are not properly predicted. Along the transition zones, the predicted values of the basis weight by numerical simulations are always lower than the measured ones, for every gush. As for the acquisition times, also the concentration profiles are slightly influenced by the value of the relative permeability. It can be pointed out that a reduction in relative permeability (a higher value of δ) generates steeper concentration profiles.

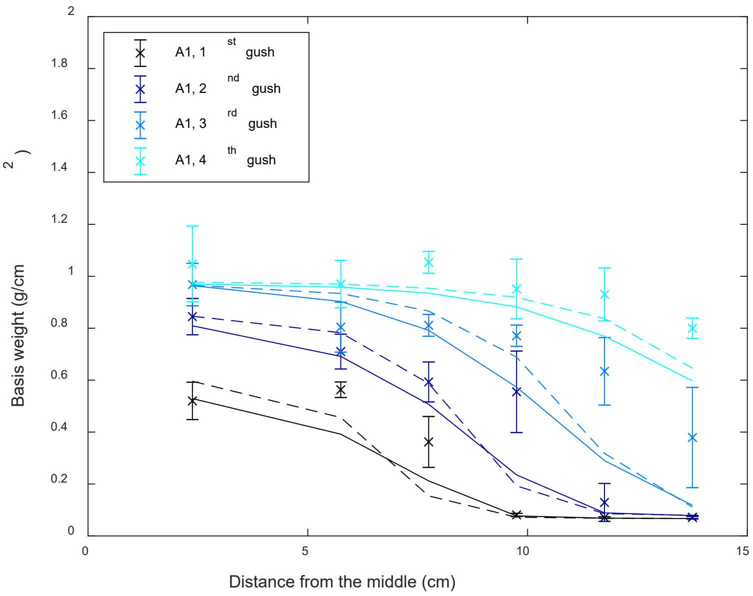

Figure 4.11. Comparison of the basis weights of the sample A1 after the gushes in the performance test. Solid and dashed lines represent simulation results with δ=3 and δ=4, respectively.

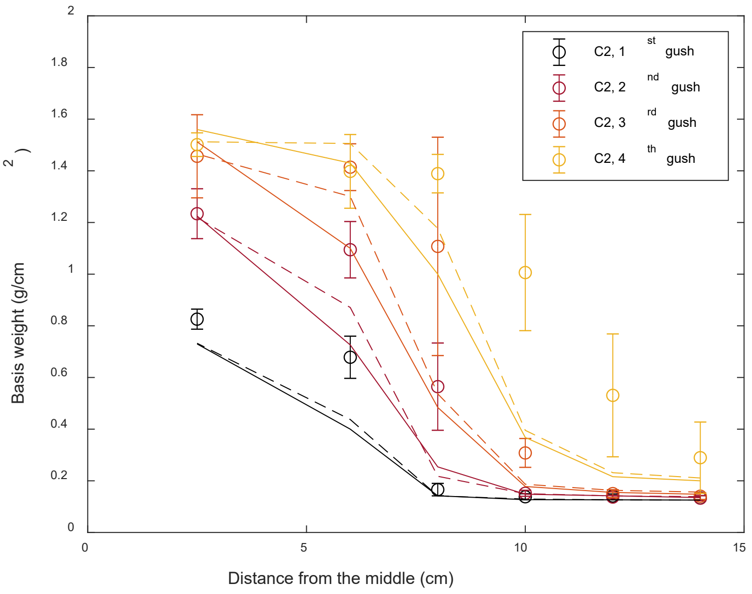

Figure 4.12. Comparison of the basis weights of the sample C2 after the gushes in the performance test. Solid and dashed lines represent simulation results with δ=3 and δ=4, respectively.

4.4. SCALED ACQUISITION TIMES

To achieve a deeper comprehension of the results presented in the current and the previous chapter it is essential to elaborate them further, with the view to capturing a general trend in our products. Whether this operation was successful, the simulations would be able to forecast the properties of hypothetical materials, not yet commercialized or even produced.

First, it is of great importance considering the amount of product consumed during the performance test, for each gush. For this purpose, the “overall product consumption” is defined as the ratio of the amount of water inside the sample and the maximum amount of absorbable water by the SAP particles inside the sample. In this sense, values of the overall product consumption above 1 means that the swelling ratio is at its maximum in every point of the sample, and there is some water remained in the pores of the material. On the other hand, values of consumption below 1 point out that part of the product left the sample and was not involved in the phenomenon of absorption. Considering only this variable, the overall consumption of an optimal product should approach unity at the expected average usage of the product (in this work, the average usage of the product was set at 320 mL of absorbed liquid), in order to exploit all the SAP inside it. Then, the product that shows higher absorbance rate would be preferable. Considering the Figure 4-7,and the acquisition times of a single series (A1–3 or C1–2), it is noted that an increase in the SAP content causes a generical decreasing of the transport properties of the materials. On the opposite, the lowest acquisition times are obtained for those material with the highest content of fibres. Taking this into consideration, the same results of Figure 4-7 are further elaborated in Figure 4-13, in which the acquisition rate of the products is compared with the overall consumption of the product for each gush.

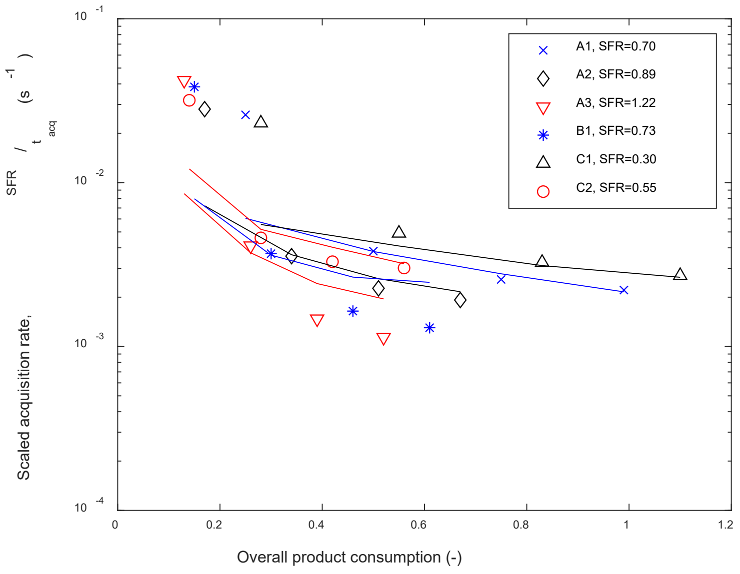

Figure 4.13. Comparison of the experimental and the numerical results for the performance test. The acquisition rate $(t_{acq}{}^{-1})$ *of each gush is compared to the overall product consumption.*

When the acquisition rate is multiplied by SFR, a general trend of the materials can be observed. Most of the values obtained from simulations and experiments fall into the band between 1E-2 and 1E-3 s^{-1}, while the scaled acquisition rates of the first gushes for the experiments are above

1E-2 s^{-1}. Moreover, not only are the samples A3 and B1, as previously noted, the least accurately simulated samples, but they are also the slowest to be imbibed, with scaled acquisition rates around or even below 1E-3 s^{-1}. Thus, especially for A3, it is possible to say that early blockage arises due to the high content of SAP particles. The reason why the blockage does not occur during the hydraulic conductivity experiment must be found in the different saturation conditions of the performance test: while the fully saturated hydraulic conductivity experiment the water exerts a constant hydraulic pressure on the surface of the SAP particles, during the performance test the stress on the surface of the particles is never constant and the swelling of the particles might be enhanced during the drainage phase. This could explain the unexpected decrease of the hydraulic conductivity during the performance test.

4.5. FINITE-SIZE SCALING EFFECTS

It clearly appears that the first gush dynamics is systematically mispredicted for each sample. As it can be observed from Figure 4-7 and Figure 4-13, for each material, the simulated acquisition time for the first gush is around 100 s longer than the time observed in the experiments. Moreover, all the composite materials show a similar behaviour for the first gush, suggesting that the hydraulic conductivity at the beginning of the test is far larger than the conductivity expressed by the equation of the model.

The departure between computed and experimental results in early imbibition is an inherent consequence of the continuum approach to the simulation of flow in the composite porous system and may be understood in the light of finite-size scaling of percolation systems.

Referring to Stauffer and Aharony (2018) [59], the properties of percolative systems (any porous system in which the permeability is non-zero is percolative) depend on a specific correlation length (ξ). Particularly, the conductivity (Σ) of the system is independent of the size of the sample (L) only for domains larger than ξ, that might be seen as the dimension of the above-mentioned REV. For smaller dimensions, a behavior based on the power law between conductivity and sample size is expected, with a negative exponent. Therefore, a large increase in conductivity is expected for very small domains. Thus, the relation is:

$$\Sigma \propto \begin{cases} L^{-\nu}, & L < \xi \\ \xi^{-\nu}, & L \geq \xi \end{cases} \tag{4.1}$$

Recalling the balance equations developed in the second chapter, in the hypothesis of the locally null liquid uptake gradient, it is possible to estimate the length in which the pressure gradient, which is the driven force of the imbibition, is fully developed. This could reasonably be considered as the minimum length needed to appreciate the transport phenomena, and then it might be accepted as an estimation of the REV size. On the other hand, the dilated thickness of the sample might serve as a domain size. The implementation of this enhancing term is then reduced to an estimation of the value for the exponent of the power law. Finally, the hydraulic conductivity function is expressed as:

$$K_{eq}^{l} = K^{l}\left[1 + \left(\frac{L}{\xi}\right)^{-\nu}\right] \tag{4.2}$$

where K_{eq}^{l} is the equivalent conductivity.

Hristopulos (2003) [60] applied similar principles to express the equivalent conductivity of relatively small porous blocks. Flow domains of finite extent belong to the pre-asymptotic regime, in which the ergodic hypothesis is not valid. In fact, for these very small domains, not all the spatial arrangements permitted by the statistical ensemble are included. Conversely, in a relevant sample, all the values of conductivity statistically allowed by the ensemble are expressed and the equivalent conductivity of the sample is the averaged conductivity of the ensemble. In this scheme, the low conductivities statistically have a more significant impact than the high conductivity values, since they can create bottlenecks for the flow. Therefore, reducing the size of the sample, i.e. reducing the fluctuations of the conductivity field, generates an increase in the equivalent sample conductivity. Hristopulos (2003) [60] investigated the relation between the equivalent sample conductivity and the averaged ensemble conductivity through Monte Carlo simulation, considering a domain of a variable size ($L/\xi \in \{10,25,50\}$).

Equation (2.4) may be conceptually considered in the following form:

$$\frac{\partial \psi^{l}}{\partial t} + \mathfrak{D}\frac{\partial^{2}\psi^{l}}{\partial x^{2}} = \sigma\psi^{l} \tag{4.3}$$

where:

$$\mathfrak{D} = \frac{K_{eq}^{l}}{\varepsilon\alpha_{w}} \tag{4.4}$$

$$\sigma = \frac{\bar{C}_{SAP_0}^{s}}{\tau\varepsilon\rho^{l}J^{s}}\left(1 - \frac{m_{2}^{s}}{m_{2_{max}}^{s}}\right)^{2} \tag{4.5}$$

Neglecting the sink term, it is possible to define a characteristic length:

$$L = \sqrt{\mathfrak{D}t} = \sqrt{\frac{K_{eq}^{l}}{\varepsilon \alpha_w} t} \tag{4.6}$$

in which the distance of penetration is proportional to the square root of the imbibition time, similarly to the solution of the Lucas-Washburn equation. Once the material characteristic length (ξ) and the exponent of the power law (ν) are known, the equations (4.2) and (4.6) can be implemented for the first gush. In the following, the acquisition times for two materials (A1 and C2) are calculated introducing the enhancing term on conductivity at the first gush. In this first attempt, $\nu = 3$ while ξ was fitted.

As it is reported in Table 4.3, the material characteristic length is around 3 cm. This can be considered as an estimation of the unit cell size of the investigated materials. The acquisition time for the first gush is correctly predicted, as it is shown in Figure 4.14. However, the acquisition times for the following gushes are changed as well: A1 shows an increased velocity for all the gushes, whilst C1 acquisition times for the 2nd, 3rd and 4th gush do not undergo significant variations.

Table 4.3. Simulated acquisition times obtained implementing the finite-size scaling theory. The fitted characteristic lengths are reported.

	ξ	ν	**1st gush**	**2nd gush**	**3rd gush**	**4th gush**
A1	3.2 cm	3	26.7 s	131 s	200 s	277 s
C2	2.6 cm	3	18.5 s	96.2 s	155 s	201 s

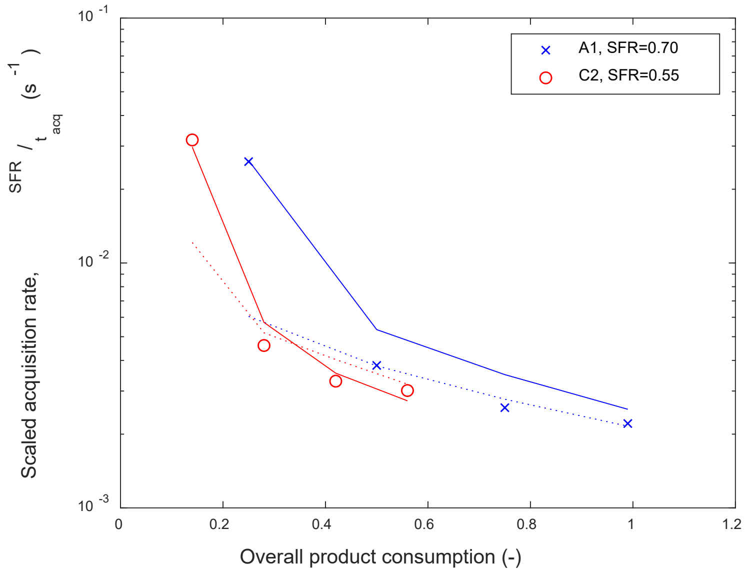

Figure 4.14 Comparison of the experimental and the numerical results for the performance test using the finite-size scaling theory. The dotted lines are the previous simulation results, the solid lines are the results obtained implementing the finite-size scaling theory.

4.6. ANALYSIS OF FLOW AND ABSORPTION TIME-SCALES

An assessment of the time scales relevant to liquid flow and absorption is performed with the aim of evaluating how water absorption and swelling of SAP compete with convective transport of the liquid phase across the porous medium. To this end, the initial flow conditions were calculated for the various composite materials. The initial velocity of the fluid for a saturated media (v_0^l) is calculated as follows:

$$v_0^l = -K_0\left(\frac{\psi_0^l}{h_0}\right), \tag{4.3}$$

where gravitational effects inside the porous media are neglected. Then, for any of the three dimensions of the sample, it is possible to define a characteristic time for the convective flow (L_i/v_0^l), defined as the time for the liquid to flow along the i direction and reach the opposite boundary, where L_i is the length of the considered i dimension. The ratio between the characteristic absorption time scale and the flow time-scale is reported in Table 4-3. According to the definition, values greater than 1 imply that absorption occurs after the completion of the liquid displacement along the considered direction and, accordingly, particle swelling barely influences liquid flow. On the contrary, values smaller than 1 indicate that rapid SAP particle swelling strongly affects liquid flow along the considered direction, resulting in incomplete exploitation of the absorption potential of the sample in a partially saturated domain.

Table 4.4. List of dimensionless numbers to estimate the flow in the samples at the beginning of the first imbibition.

Composite label	**Initial liquid velocity, v_0^l (mm/s)**	**τ (s)**	$\frac{v_0^l}{h_0}\tau$	$\frac{v_0^l}{L_x}\tau$	$\frac{v_0^l}{L_y}\tau$
A1	10.6	4.92	15.8	0.8	0.3
A2	8.4	5.22	11.8	0.7	0.3
A3	4.9	4.62	5.4	0.3	0.2
A4	2.8	6.32	4.2	0.3	0.1
B1	4.2	4.72	3.7	0.3	0.1
C1	6.0	4.88	5.2	0.5	0.2
C2	5.2	4.41	3.7	0.4	0.2

Data reported in Table 4-3 indicate that flow along the z axis is not influenced by particle swelling. In this sense we could imagine that absorption starts once the material is fully saturated. Moreover, if at any time the saturation is the same along the thickness dimension, it would be possible to average the hydraulic properties along that dimension. On the contrary, flow along the planar directions and absorption have to be solved at the same time. Correspondingly, the early stage of the process could be considered a two-dimensional process along the planar directions (L_x, L_y) with saturation and hydraulic properties that are uniform along the vertical axis. Dilation of the sample and decrease in the hydraulic conductivity upon imbibition bring about a reduction of the dimensionless number $v^l\tau/h_0$. Correspondingly, the flow along the z axis is hindered and non-uniform hydraulic properties establish across the sample, restoring the 3D character of the absorption and flow pattern.

4.7. COMMENTS ON THE FEM SIMULATIONS' OUTCOMES

The model has been tested against results of an experimental campaign performed in realistic conditions (a set of four subsequent gushes) with a set of AHP samples of different SAP/fluff mass ratio. The comparison has been performed in terms of liquid acquisition time and spatial distribution of the liquid across the sample at selected times during the performance test.

The comparison between experimental and numerical data shows good agreement and supports the validity of the proposed model. Simulated acquisition times are well predicted for the second, the third and the fourth gush. Prediction of the first acquisition time for all the composites is less accurate, a feature that can be explained in the light of percolation theory as a consequence of enhanced hydraulic properties due to finite size scaling effects. Also, the computed distribution of liquid at selected locations in the sample compares well with the experimental results, confirming the soundness of the model to predict the development of the absorption and flow patterns in the composite medium, with a clear path to possible improvements in the simulation of the early imbibition stage. Improvements in the simulation of the early imbibition stage implementing the finite size scaling effects for the first gush have been obtained and indicate a clear and feasible path toward further model development and optimization. Altogether, the model used in the present study, together with the companion experimental characterization procedure described in Chapter 3, provide powerful and effective tools to improve design of AHPs.

5. DEM MODELLING

A numerical study based on the Discrete Element Method (DEM) was carried out with the aim of predicting the morphological properties of the swelling porous materials. The determination of the flow properties of a swelling porous medium is requirement in order to advantageously resolve the velocity field of the fluid and consequently to design the most effective product. However, experimental campaigns are often time-consuming processes and due to the large number of properties experiments are hardly on active plan for many companies in this sector. Numerical simulations may be seen as numerical experiments, in which many details of the sample are represented. This methodology allows to estimate the effects of the single variables, which in lab experiments are difficult to isolate. Thus, numerical simulation are often effectively exploited when the accuracy of the lab equipment is not sufficient.

Here, a multi-scale approach was adopted, generating a realistic porous domain at the grain scale in a representative elementary volume (REV), in order to calculate spatial averaged properties (porosity, components bulk densities, permeability), depending on the water uptake, to be used in a macroscale simulation. The implemented software is YADE-DEM, in which cellulose fibres and SAP particles are represented as connected cylinders and spheres, respectively. The study aims at determining the length scale of the REV and the flow properties of materials with varying SAP–fluff ratio (SFR), at different swelling values. The numerical results are also compared to experimental outcomes previously obtained with the same class of composite materials.

5.1. MODEL DESCRIPTION

The model framework is a Discrete Element Method (DEM) model in which the two phases, SAP particles and fluff, are treated as granular phases. While the SAP phase is actually a granular phase, the same cannot be said for the fluff phase, which is composed by a very intricated fibrous net. Thus, it is necessary to model a granular phase which represent the bulk properties of the fluff.

Heyden (2000) [23] has studied the mechanical properties of fluff exploited in SKA products through numerical simulations in which a periodic cubic domain made of cellulose fibres is studied. Many parameters have been investigated, such as the fibres bulk density or the interactions between the fibres, and the results are shown in terms of stiffnesses and Poisson ratios of the ensemble. Before all, the first real result is the determination of the Representative Elementary Volume of the system. She has found that a cubic domain with dimension equal to 1.2 the length of the fibre, whose length was set at 1.0 mm, is enough to adequately describe the whole material. Among the long list of results obtained in Heyden (2000) [23], in the present model the properties of the fluff phase considered are reported in Table 5-1.

Table 5.1. Values extracted from Heyden (2000) [23] *and exploited in the present work.*

Cell size (mm)	**Number of fibres per cell**	**Cross section area of the fibre (µm^2)**	**Porosity**	**Interactions among fibres**
1	250	250	0.92–0.96	1

The interactions among fibres is an estimation of the number of connections between two fibres, thus a value of 1 means that every fibre interacts with one other. Heyden (2000) [23] obtained for a cell a stiffness of 200 kPa and a Poisson coefficient of 0.25. These parameters have been used in the present model, after having performed a sensitivity analysis on them.

Regarding the size of the pseudo-particles of fluff to be used in this granular model, it has needed an optimization, as a result of a compromise between numerical simulation accuracy and computational efforts. Since computer resources are limited, it is preferable to analyse as large a fluff particle as possible, in order to reduce the number of elements in the simulations. At some point, however, the results are affected if the pseudo-particles are too large compared with the SAP particles and the simulated domains. On the other hand, the ideal case in which fluff is represented with a continuous phase corresponds to infinitesimal particles. Moreover, if the particles are small, the interstitials among the pseudo-particles will also be minimized

The shape of the particles used in the AHPs is irregular, because of their manufacturing, in which a bigger polymer block is ground. Moreover, an irregular shape guarantees a high surface-volume ratio that is proportional to the absorption rate [10]. In a DEM model an irregular particle can be represented as a clump of spherical particles. Nevertheless, a spherical shape for all the particles has been considered in the present model, as a starting point. Furthermore, in order to avoid any statistical effects related to the distribution of diameters, all the SAP particles have the same size, in their dry state.

The stiffness of SAP particles decreases with the liquid uptake [13]. While a dry SAP particle is conventionally represented as a sugar-like granule, and so it is hard, during the water absorption the mechanical properties change, and they become softer and softer. That is why this material is also called Absorbent Gelling Material (AGM). The stiffness and the shear modulus are connected through the Poisson ratio in the following form:

$$E = 2(1+\nu)G, \tag{5.1}$$

where G is the shear modulus and ν is the Poisson ratio.

In the work of Sweijen et al. (2017) [20], the shear modulus was related to the liquid uptake with the following equation:

$$G = \frac{\beta}{{m_2^s}^{\frac{1}{3}}}, \tag{5.2}$$

where m_2^s is the liquid uptake (or the swelling ratio), expressed as mass of liquid absorbed per mass of polymer, and β is related to the shear modulus at the maximum swelling extent and it depends on the specific polymer. This formulation is valid only when the particles have already absorbed an amount of liquid and they are no longer in the glassy state. The values used by Sweijen et al. (2017) [20] to express β is:

$$\beta = \frac{G_e}{{m_{2max}^s}^{\frac{1}{3}}}, \tag{5.3}$$

where G_e is the value of the shear modulus at its maximum liquid uptake (m_{2max}^s). Sweijen et al. (2017) [20] considered $G_e = 7.1$ kPa and $m_{2max}^s = 50\ \mathrm{g_{abs}/g_{SAP}}$. The Poisson ratio used here is $\nu_{SAP} = 0.5$, typical of materials which keep their volume nevertheless the deformations

In order to dynamically represent the liquid uptake, Sweijen et al. (2017) [19] developed the following equation in terms of radial coordinates:

$$\frac{\partial\theta(r,t)}{\partial t} = \frac{D}{r^2}\frac{\partial}{\partial r}\left(r^2\frac{\partial\theta(r,t)}{\partial r}\right) \tag{5.4}$$

for $0 < r < R(t)$ and $t > 0$, where θ is the absorption capacity of the polymer, D is the constant diffusion coefficient and R is the current radius of the SAP particle, which is swelling. In his Ph.D. thesis, Sweijen varied the diffusion coefficient between 10^{-6} and 10^{-3} cm^2/min [41].

Nevertheless, to speed up the simulation experiment, the diffusion coefficient was increased ad libitum. Due to the high uptake rate, the forces acting on the particles would be enormous, threatening critically the simulation stability. However, as the described model a representation of a quasi-static phenomenon, it is fair to dissipate kinetic energy of particles. In YADE, this is made on each of the velocity components, introducing the damping factor (λ_d), which is dimensionless and acts on forces. The form used in the DEM software to calculate the damping acting on the forces is the following one:

$$\frac{(\Delta \boldsymbol{F})_{di}}{\boldsymbol{F}_i} = -\lambda_d \operatorname{sgn}\left[\boldsymbol{F}_i \left(\dot{u}_i^- + \frac{\overset{\circ}{\ddot{\boldsymbol{u}}}_i \Delta t}{2}\right)\right], \tag{5.5}$$

where subscript i represents one of the three the directions considered while subscript d stands for "damping", the superscripts − and ° means previous and current timestep, respectively, $\boldsymbol{F}$ is the force at current time step, u is the displacement vector and Δt is the timestep. This artifice brings stability to the simulation, without compromise the quality of the study. Moreover, it is necessary to introduce a dissipation, as the considered force exerted by the particles in this study is only elastic. For more information regarding the usage of the damping factor in DEM simulations, the reader is referred to the website of the YADE software, where a large bibliography is quoted [61].

5.2. GENERAL SCHEME OF THE SIMULATIONS

Two clouds of particles are generated in a parallelepiped domain, a box with a square cross-section. The size of the cross-section area is the characteristic length of the REV considered, while the other dimension of the domain is parallel to the gravity force and is much longer than the characteristic length. A large domain is necessary to generate two clouds of particles initially not in contact. The number of the spheres is calculated in order to have a determined basis weight of the compounds, that means a specific amount of material per surface. In manufactory of AHPs, in fact, basis weights are the quantities used to produce materials with different bulk concentrations of their compounds. The production of the AHPs also, in which fluff fibres and SAP particles are vigorously mixed and then pressed by a wheel, is quite similar to the process used in the present work to generate the virtual samples.

A schematic flowchart of the simulation is reported in Figure 5-1. The particles fall driven by gravity and they deposit at the bottom of the domain. Once the unbalanced force (the ratio between the average of the body forces by the average of the contact forces) of the particles ensemble is below 0.001, the deposition is considered completed and the result is an uncompressed granular material, with SAP particles and fluff pseudo-particles mixed. Even though the clouds of particles are randomly generated, it is possible to assign a seed number in order to have the same initial clouds of particles and then the same initial mixing. After the deposition, a compression phase starts. At this point, a plate with no thickness is generated above the particles. While it moves downward, it compresses the granular bed below. The compression is calculated as the ratio between the sum of the forces acting on the plate and the cross-section area of the domain. At the desired value of compression, the plate stops and the initial thickness and porosity of the sample are registered.

At the end of the compression, the SAP particles are allowed to swell, in a very controlled way. During the swelling of the SAP particles, the size of the whole sample is blocked by the domain walls and the plate above the granular bed, as shown in Figure 5-2. Then, the volumetric growth of the particles increases the sum of the forces exerted on the plate above, increasing the compression value of the sample. The swelling is conventionally stopped when the liquid uptake is increased by 1g/g. Then, the plate slowly moves upward to relax the sample and to bring back the compression value to the initial value. Therefore, the plate stops and a new swelling step starts with the same procedure. The algorithm goes on until the maximum uptake of the particle is obtained. For each absorption level, the porosity and the thickness of the granular bed is registered. The results are shown in plots comparing these two quantities with the uptake of the liquid by SAP particles.

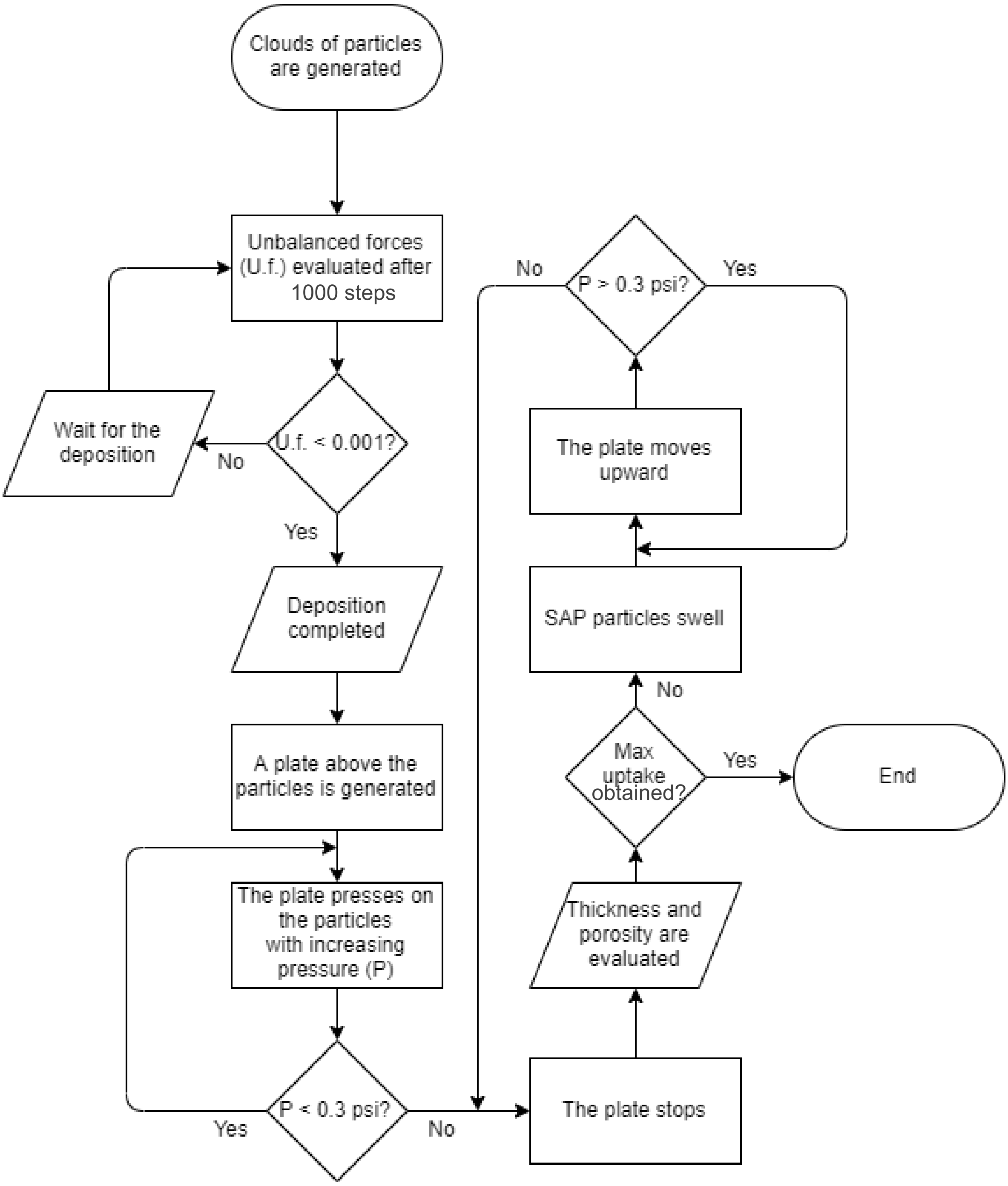

Figure 5.1 Flowchart of the algorithm used in the simulations.

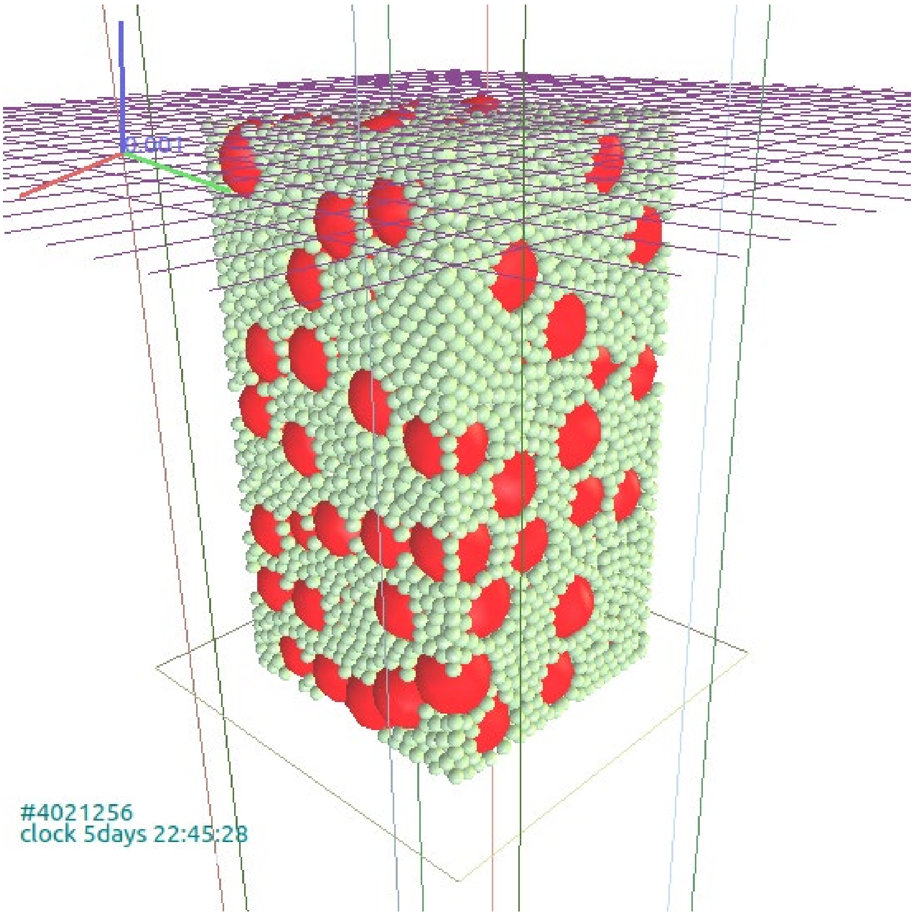

Figure 5.2 A generic simulated sample. The green particles are the fluff pseudo-particles, the red ones are the SAP particles. The partially swollen sample is confined in a rigid open box (4 walls and a bottom surface) and a moving plate above it.

5.3. PRELIMINARY SIMULATIONS ON FLUFF PSEUDO-PARTICLES

Before going deeply into the simulations, the fluff pseudo-particles must be better defined, in terms of diameter, porosity and stiffness. It is worth to note that the only effect of the pseudo-particle porosity is on the density of the pseudo-particle itself, that is the value of the fibre density multiplied for the value of porosity. The property which acts as a bottleneck for the whole experimental campaign is the particle diameter. As mentioned above, fluff pseudo-particle dimensions require optimization to reach a compromise between accuracy and calculation efforts. That means that a large number of small pseudo-particles might be a good representation of a continuous phase, but the calculations to solve all the interactions between them will most likely be computationally unaffordable. Moreover, if interstitials are present between fluff pseudo-particles, the whole fluff phase (i.e., the portion of the domain not occupied by SAP particles) must consider them into the particle porosity calculations, in order to obtain the correct target porosity for the phase. In the end, a sensitivity analysis on the stiffness is done, to figure out the effects of it on the thickness of the sample.

i. POROSITY OF FLUFF

Heyden (2010) [23] reported that varying the bulk density, and so the porosity, for a given value of the interaction between fibres, has an effect on the Young modulus of the sample. For instance, considering a conventional interaction fibre $s_{FL} = 1$ and a stiffness of $E_{FL} = 200$ kPa, the correspondent porosity is $\varepsilon = 0.92 - 0.96$. In a granular pack, the sum of the voids between the particles represent the void fraction of the bed. If the particles are considered porous, with a porosity of ε_{FL}, the equivalent porosity of the granular pack (ε_{eq}) is calculated as:

$$\varepsilon_{eq} = \eta + (1 - \eta)\varepsilon_{FL}, \tag{5.6}$$

where η is the porosity of the granular pack.

Rearranging this equation, if the equivalent porosity of the granular pack is set, the porosity of the single particle is then calculated as:

$$\varepsilon_{FL} = \frac{(\varepsilon_{eq} - \eta)}{1 - \eta}. \tag{5.7}$$

If we consider the tightest pack of particles, and so the face-centred cubic (FCC) structure, it has a porosity of $\eta \approx 0.36$. Although particles in DEM can overlap, for this value of the porosity of the granular pack, we can obtain an estimation of the maximum value acceptable for the fluff pseudo-particle porosity. If $\varepsilon_{eq} = 0.94$, we obtain:

$$\varepsilon_{FL}|_{\eta \approx 0.36} \approx 0.9. \tag{5.8}$$

From this value, it is possible to assign the proper density at the fluff pseudo-particle (ρ_{FL}), knowing the density of the fibre (ρ_f):

$$\rho_{FL} = \varepsilon_{FL}\rho_f. \tag{5.9}$$

Consequently, the number of the pseudo-particles generated at the beginning of the simulation is easily calculated from the fluff basis weight of the material, once the diameter of the pseudo-particle and the domain dimensions are set.

ii. FLUFF PSEUDO-PARTICLE SIZE

In a domain with a cross-section area of 3 mm^2, three simulations at fixed SAP–fluff ratio (SFR) and variable pseudo-particle diameter have been done. The other properties, porosity and stiffness of pseudo-particles, were kept constant. The investigated SFR was 1, while the basis weight of the entire material was 200 g/m^2. The used parameters are listed in Table 5-2. Regarding the number of elements used in these 3 simulations, each time the diameter is halved, the number of particles increases by a factor of 8. The number of generated elements is listed in Table 5-2, for each value of the pseudo-particle size. Considering that the calculation time is proportional to the interactions between the particles, the calculation efforts rapidly grow with the number of the elements.

Table 5.2. Parameters used in the simulations for the estimation of the fluff pseudo-particle diameter.

Global basis weight (g/m^2)	SFR	Fluff pseudo-particle porosity	Initial SAP particle radius (µm)	Fluff pseudo-particle radius (µm)	Number of SAP particles	Number of fluff pseudo-particles
200	1	0.9	150	300	39	36
200	1	0.9	150	150	39	290
200	1	0.9	150	100	39	979
200	1	0.9	150	75	39	2320

The porosity and thickness of the composite are compared with the liquid uptake in the graphs reported in Figure 5-4. As it can be observed, while the porosity immediately decreases with the liquid uptake, the thickness has a slightly different behaviour: for very low swelling extents, the thickness remains almost constant, then it increases linearly for higher values of swelling. That is not unrealistic, as the SAP particles firstly try to occupy the void space of the porous material, and only after, when they are not able to do it anymore, they push the weight above the sample and displace the boundary of the domain. In doing this, the SAP particles, which were isolated initially, often interact each other, creating a connected phase, which is theoretically able to carry the stress of the weight above the sample.

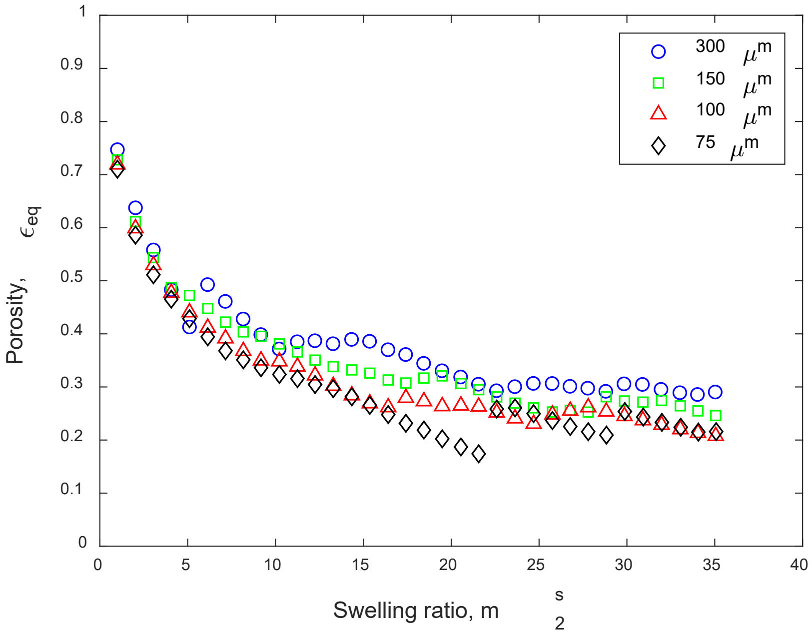

Figure 5.3. Results of the simulations of a sample with the properties reported in Table 5-2. The decrement in porosity against the swelling ratio is reported.

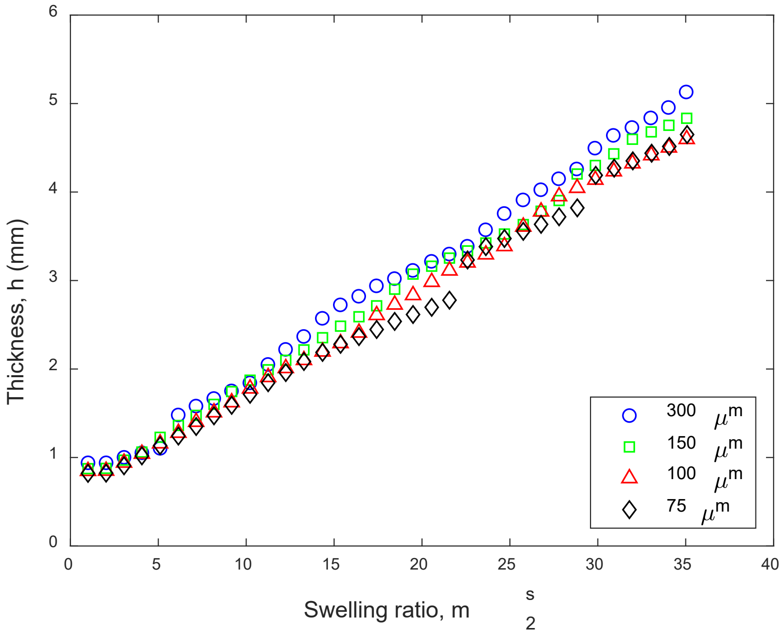

Figure 5.4. Results of the simulations of a sample with the properties reported in Table 5-2. The increment in thickness against the swelling ratio is reported.

Considering only the linear regime after the first little increment of SAP particles volume, it can be mathematically described measuring the slope and the y-intercept of the thickness function. In Table 5-3 these values are reported. A correlation can be noticed between the investigated diameters and the coefficients obtained. Plotting the coefficients with the fluff pseudo-particle diameter, it is possible to linearly extrapolate the ideal values for those coefficients at null diameter, as presented in Figure 5-5. The ideal growth of the virtual sample is a valuable information to determine the quality of the discretization of the sample. Thus, the ideal thickness should grow linearly with the following law:

$$h = 0.115\ \text{mm} * m_2^s + 0.48\ \text{mm} \tag{5.10}$$

Table 5.3. List of the coefficients of the linear fitting of the increasing thickness for different diameters of fluff pseudo-particles. The error with respect the ideal case is reported as well.

Fluff pseudo-particle radius (μm)	*a* (μm)	*b* (μm)	Estimated error
300	128	614	16 %
150	122	604	12 %
100	118	547	6 %
75	119	471	2 %
0 (ideal)	115	480	-

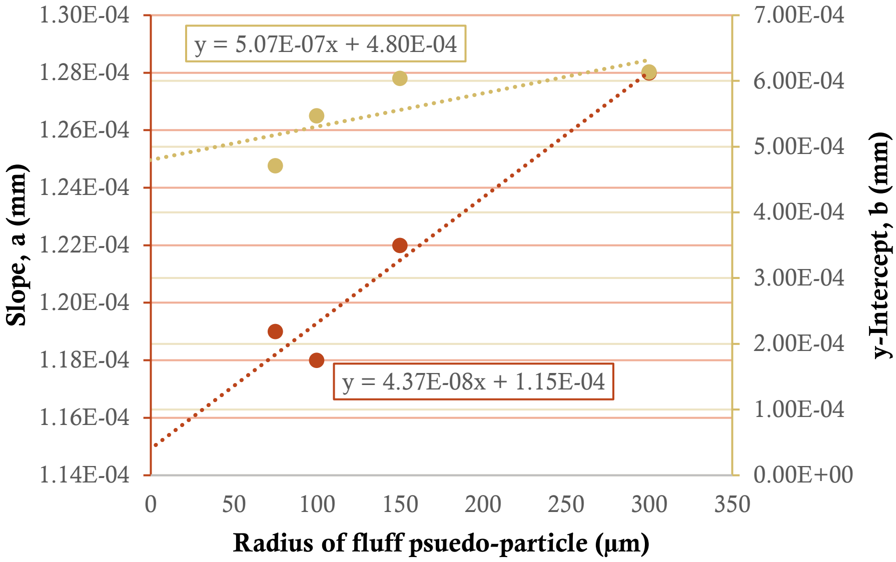

Figure 5.5. Coefficients of the linear fitting of the increasing thickness for different diameters of fluff pseudo-particles.

Consequently, an estimation of the error was taken for each diameter, as reported in Table 5-3. A good balance was found using the pseudo-particles with 100 μm of radius, which guarantees an error below the 10% on the thickness estimations. This size was kept constant for the following simulations.

iii. YOUNG'S MODULUS

A sensitivity analysis on the fluff elasticity was conducted. The Young's modulus has been varied around the previously set value of 200 kPa and the porosity and the thickness of the sample is reported. The cross-section area of the domain was kept constant at the value of 9 mm^2. The results are collected in the plots in Figure 5-6 and in Figure 5-7.

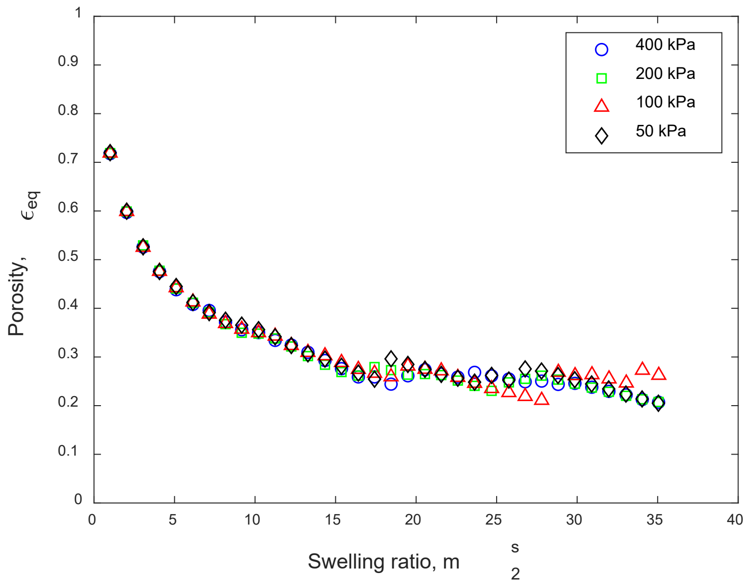

Figure 5.6. Plot of the decreasing porosity for samples with different Young's modulus of the fluff pseudo-particles.

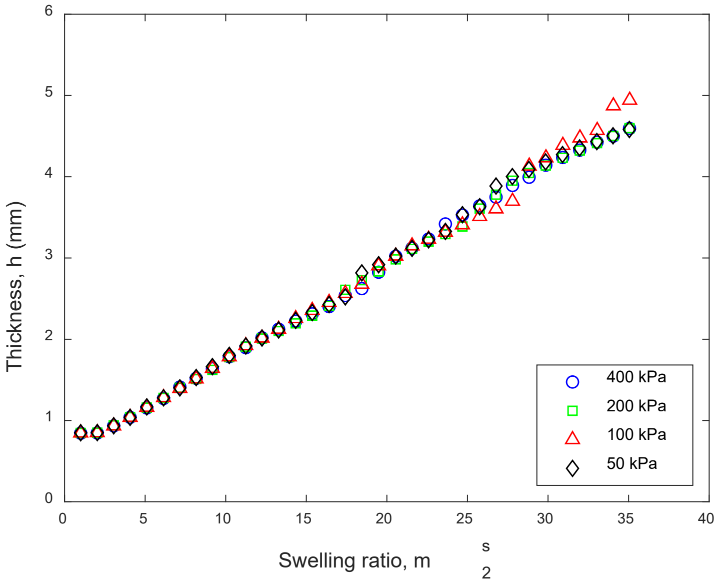

Figure 5.7. Plot of the increasing thickness for samples with different Young's modulus of the fluff pseudo-particles.

In the range of the investigated values, no sensible variations were observed. In this way, since there is a general convincement that fluff elastic modulus is around 200 kPa [23], it is possible to sustain that an error on that value has not a great influence on the overall measurements.

iv. REV ESTIMATIONS

The simulations done up to this point should not be considered as the realistic representation of a larger object, even though the properties implemented in it are the same. This is due to the small domain considered, which might not be statistically enough to describe a larger sample. Thus, it is necessary to define the smallest possible REV, in order to have consistent measurements with the lowest computational effort.

The area considered in the previous simulations is a square of side 3 mm. In the following ones, the side dimension is increased and the porosity and thickness of the sample are evaluated. Again, through the comparison of the linear trend of the increasing thickness, it is possible to choose the size that minimizes the error. In Figure 5-8 and in Figure 5-9 the results of four simulations with different domains are plotted. The porosities and the thicknesses of the investigated samples are compared with the liquid uptake of the SAP particles. No great differences emerge from this comparison. In Table 5-4 the domain side length and the coefficient of the linear increment of the sample are listed.

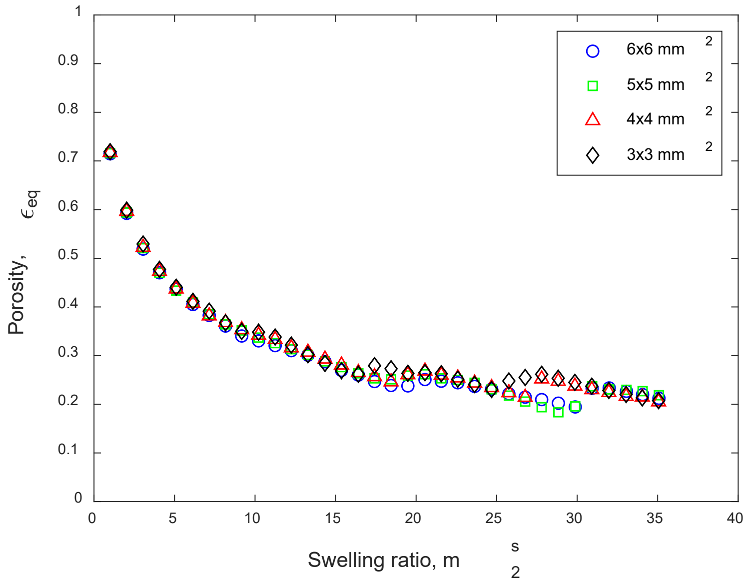

Figure 5.8. Plot of the increasing thickness for samples with different domain size.

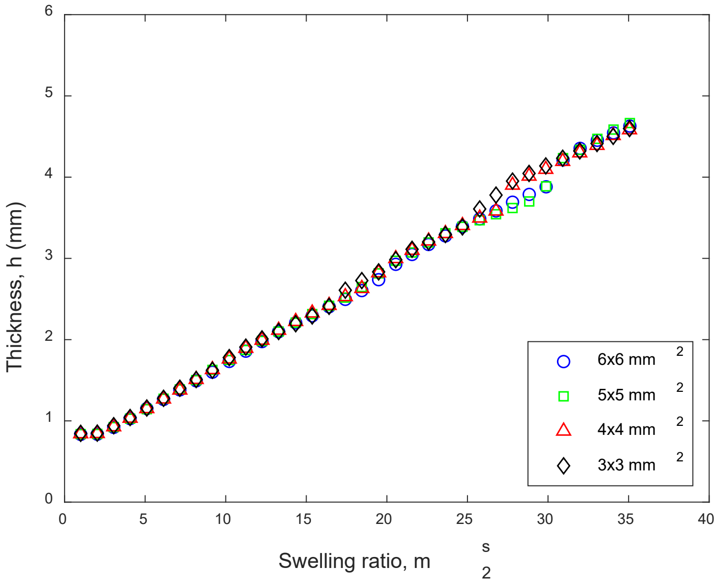

Figure 5.9. Plot of the increasing thickness for samples with different domain size.

Table 5.4. List of the coefficients of the linear fitting of the increasing thickness for different domain size. The error with respect the ideal case is reported as well.

L (mm)	1/L (mm^{-1})	*a* (µm)	*b* (µm)	Error
3	0.33	118	545	3.9 %
4	0.25	117	550	3.4 %
5	0.20	116	548	2.6 %
6	0.17	116	529	1.8 %
→∞	→0	113	527	-

Again, the ideal thickness should grow linearly with the following law:

$$h = 0.113 \text{ mm} * m_2^s + 0.527 \text{ mm}. \tag{5.11}$$

All the domain sizes considered bring to almost the same result in terms of thickness and porosity values. The error done in considering a finite size for the domain is always under 5% the interpolated one for infinite lengths. For the following simulations, it has been set the size of 4 mm per 4 mm, immediately larger than the minimum considered in the REV evaluation.

5.4. SIMULATION OF REALISTIC ABSORBENT LAYERS

Once all the parameters are defined, it is possible to compare the simulation results with the experimental values, to validate the model against the experiments. Some of the previously analysed absorbent pads, whose properties are defined in Chapter 3 were considered as a benchmark. In Figure 5-10 and in Figure 5-11 the variable porosity and thickness are plotted against the liquid uptake of the SAP particles, respectively. The basis weights and the initial thickness and porosity of these composite materials are reported in Table 5-5. Not all the investigated samples have been tested, but only the lightest (A1, A2, A3 and A4), in order to keep low computational effort.

Table 5.5. Properties of the different composite materials considered as a benchmark.

Label	SFR	Initial thickness	Initial porosity
A1	0.67	3.31	0.886
A2	0.89	3.72	0.889
A3	1.22	4.22	0.888
A4	1.67	4.22	0.868

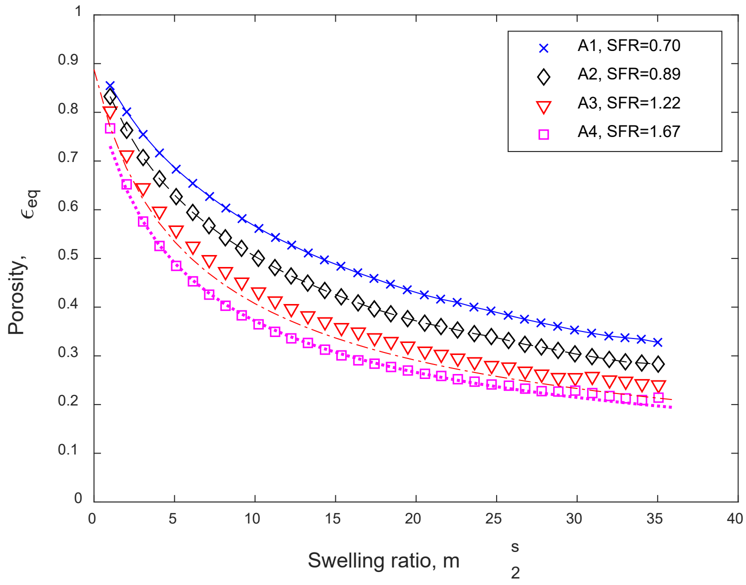

Figure 5.10. Comparison of the porosity values obtained from DEM and experiments, for the investigated samples listed in Table 5-5. The fluff pseudo-porosity for these simulations is $\varepsilon_{FL} = 0.90$.

The model developed so far give an accurate prediction of the experiments. As it can be observed form the plots of porosity and thickness in Figure 5-10 and in Figure 5-11, the two properties are both well estimated. At the highest swelling extent, the curves of porosity obtained from the DEM simulations reach a common value, around 0.20.3. A similar threshold was observed also in the experiments, whose results are exposed in Chapter 3. The results reported in this Chapter were obtained after one or two days of simulation, run on a Dell Precision T7500, having a quad core CPU (Intel® Xeon® E5620 @ 2.40GHz) and a RAM of 8 GB.

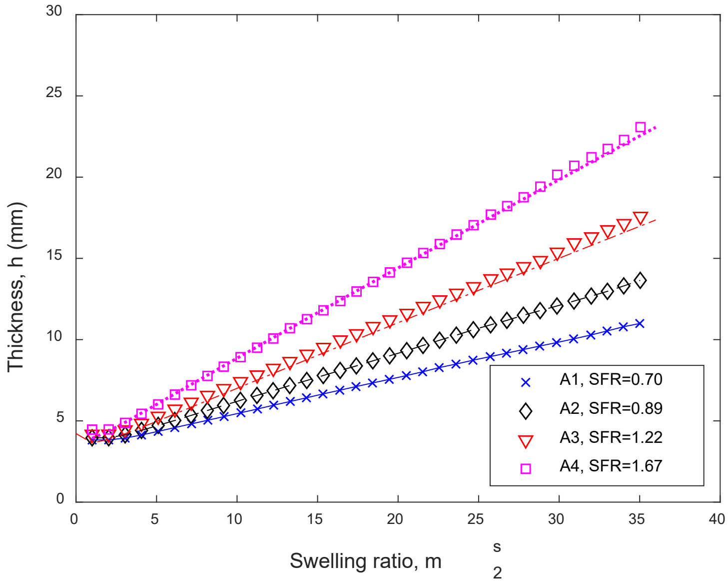

Figure 5.11. Comparison of the thickness values obtained from DEM and experiments, for the investigated samples listed in Table 5-5. The fluff pseudo-porosity for these simulations is $\varepsilon_{FL} = 0.90$.

5.5. COMMENTS ON THE DEM SIMULATIONS OUTCOMES

A DEM model of absorption in swelling porous media relevant to absorbent hygiene products is presented. The sample is described as a granular bed of two different granular matters: the super absorbent polymer (SAP) particles and the fluff pseudo-particles. Only uniform distributions are considered, for each phase. The water absorption of SAP particle is simulated increasing the size and decreasing the elastic modulus of the grains. The fluff pseudo-particles do not change in size or in mechanical properties during the absorption of liquid. The compression of the simulated samples is imposed and mimics the conventional body weight on absorbent products. The porosity and the thickness of the swollen samples are evaluated against the liquid uptake.

The parameters needed for the DEM modelling were taken from both literature and preliminary simulations. The intrinsic porosity for the fluff pseudo-particles has been estimated on the base of geometric considerations. A sensibility analysis on the size and the stiffness of the fluff pseudo-particles has been done. The size of the domain considered and the estimation of the representative element volume have been previously evaluated as well.

The model has been tested against experimental results. The investigated samples have different compositions of SAP and fluff and express different changes in porosity and thickness. For all the four investigated samples, a remarkable agreement between the experiments and the DEM results is achieved. Further estimations and comparisons on many more samples are required to confirm the predictability of the model.

Altogether, the model developed in the present study has the potential to effectively predict the volume averaged properties of porous swelling media and may lead to a deeper knowledge of morphological modifications occurring in similarly soft and swelling materials.

6. SUMMARY AND PERSPECTIVES

6.1. SUMMARY

This thesis describes both an experimental and a modelling method to investigate absorbent swelling porous media relevant to absorbent hygiene products (AHP). An experimental protocol and an existing model of continuum, previously presented in literature, have been adapted to address the specifications of the products subject of study, namely:

1. The cellulose fluff as a carrier material of the super absorbent polymer (SAP) particles;
2. The variable ratio between the two major compounds (SFR), the SAP particles and the fluff;
3. The hydraulic properties (porosity, permeability, retention) depending on the swelling extent of the SAP particles;
4. The need to predict both steady-state conditions (i.e. the liquid concentrations profiles inside the samples) and dynamical properties of the samples (i.e. the flow rate of liquid entering the sample).

A grain-scale model, specifically the discrete element model (DEM), has been applied in an original approach, to forecast volume averaged properties of the examined samples, namely the porosity and the swelling extent. This study shows the applicability of the continuum approach in modelling layers of AHP and of the discrete approach in determining material properties. The aim throughout this research is to study processes that occur in layers of fibres and swelling particles, to offer a better insight on the phenomena occurring in a so complex system and to optimize the industrial design of the finished product.

In Chapter 2, the mathematical model is presented and adapted to the current study requirements. The main differences with the model borrowed from literature regard the kinetics expression of liquid absorption by SAP particles and some of the closure equations. A remarkable correspondence has been found with experimental results when a second order kinetics was employed. This was explained as an effect of the different initial absorption rate of the particles, due to their different sizes. The adoption of such kinetics equation brings homogeneity even to the maximum measured swelling extent, set at 37 g/g. The shape of the hydraulic conductivity equation has been modified with respect to the reference study, in order to properly represent the investigated products, while reducing the number of the fitting parameters.

The experimental protocols have been treated in Chapter 3. From the results obtained in this section, part of the model presented in the previous Chapter was adapted, as has been discussed for the kinetics equation and for permeability. It was shown that the SFR strongly determines the intensive properties (porosity and hydraulic conductivity), while the extensive properties, such as the swelling dependent thickness, are trivially determined by both the bulk concentrations of compounds taken separately. The range of SFR considered in the present experimental campaign is 0.3–1.67. Porosity values never goes below 0.2, even for the highest swelling extent. The initial hydraulic conductivity value is around 3 10^{-4} m/s and it decreases rapidly with the absorption. Gel-blocking effects have been observed in the hydraulic conductivity test for SFR equal to 1 or more. A notable correlation between porosity and hydraulic conductivity has resulted from each investigated sample, despite the different swelling extent. This remarkable feature gives a deeper understanding on phenomena occurring at the pore scale level, bringing the study of AHPs closer to that of other porous media. The retention model evaluated for these products does not align with the results found in literature addressing bed of swelling particles. It has been found that the main wetting and drainage curves have no dependencies on the liquid uptake of the SAP particles. The unexpected observations have been motived as an effect of the fibrous matrix occupying the void space of the material, attenuating the influences of the reduction of porosity on the retention model.

The simulations described in Chapter 4 have been performed with a continuum approach, in saturated or unsaturated conditions. The comparison with the experimental results has been constantly taken into account throughout the Chapter. By and large, the flow rate of the investigated samples is correctly predicted for already swollen samples. The prediction appears poorer in the case of a dry sample as initial condition. The introduction of the finite-size scaling feature has been proposed, to overcome these inconsistencies and give further scientific tools to investigate these complex systems. On the other hand, the general concordance of liquid concentrations inside the samples between numerical and lab experiments is certainly a remarkable result, though the modelling parameters must be tuned in future to increase the predictability of the liquid distribution. However, the liquid distribution itself may be affected by the finite-size scaling models.

Finally, a grain-scale model has been developed in Chapter 5. The main feature of the model is the approximation of the fluff phase with porous particles. The model employed considers only one particle size for each phase, 150 μm for SAP particles and 100 μm for fluff pseudo-particles. Mechanical properties of the compounds together with the domain and particle sizes may be easily changed, to have an appropriate and realistic representation of the investigated sample. In this Chapter, a simulation scheme has been provided, in order to virtually represent the absorbing phenomena. Several preliminary simulations have been performed to determine the optimal sizes of fluff particles and domain. A representative elementary volume (REV) with dimension of 4 mm^2 has been considered enough for investigating on morphological properties of the bed of particles. The porosity and the dilation dependencies with the swelling ratio for 4 investigated materials have been evaluated and the model successes in predicting porosity and thickness dependencies with liquid uptake.

6.2. PERSPECTIVES

Macro-scale models allow to predict the general aspects of complex phenomena. In this thesis, lab experiments and two modelling approaches, a continuum model and a grain-scale model, were employed. Despite of the convincing results, further researches are needed to address various aspects about the physics of these products.

For example, the hydraulic conductivity of the samples was assumed to be isotropic. However, it is reported in literature that the orientation of the fibres may drastically change the permeability tensor. This is very likely to happen during manufacturing of the fibrous layers. An experimental apparatus that investigate the flow rate in the planar directions is not an easy to build device for swelling objects. In this sense, numerical simulations may bring a deeper perception about the sample properties. Performing simulations on a macro-scale, the permeability tensor might be tuned on the experimental results, e.g. the liquid profile inside the sample. Furthermore, the swelling of the particles may influence the direction of the flow, as well.

Another aspect to be investigated is the relative permeability model to use for this class of fibrous and swelling materials. In the present study, the very simple Brooks and Corey model was used. The choice of the best model should be driven by appropriated lab experimental results, and so new tests need to be considered. Again, having a macro-scale model might be incredibly helpful in order to determine first attempt values, guiding the lab activities.

Moreover, the master-curve binding the porosity and the permeability values should be better-defined. First, the plateau of permeability for the highest values of porosity must be explained. Second, the role of SAP/fluff ratio has to be clarified and quantitatively determined. In this case, the grain-scale approach, here used only for the porosity and thickness evaluations, may be further employed, to get probably useful geometrical parameters of the virtual ensemble, e.g. coordination numbers of SAP particles or the constitution of clusters of SAP particles.

The mathematical model itself should also be extended. For example, the feature of the finite-size scale has to be quantitatively determined and validated experimentally. In addition, also the role of the probability density function of the sizes of the SAP particles must be taken into account and quantified. On the other hand, the dependence of the retention model's parameters on the swelling degree of the SAP particles should disappear from balance equations, at least for materials with fluff as carrier material.

Finally, different shapes and size distributions of the particles may be used in the grain-scale simulations. To this end, the creation of virtual clumps of spheres seems to be the best solution in terms of numerical stability and simulation speed. The simulation results here presented demonstrate the versatility of a grain-scale method, which can be successfully employed also for non-granular phases.

APPENDIX A

THE ABSORPTION KINETIC REACTION

In the review of Zohuriaan-Mehr and Kabiri (2008) [10] the swelling particles are assumed to absorb water with a linear kinetics. However, the kinetics equation used here (2.7) is a second-order kinetics. Zohuriaan-Mehr and Kabiri (2008) [10] also reported that particles with smaller size have a larger swelling rate, due to the higher ratio of interfacial surface and volume of the particle. The (2.7) was the best fit equation for capturing the dilation trends and having a homogeneous maximum swelling ratio among the samples. Here, the form of the absorption equation for particles of different size is derived.

Assuming that the characteristic time is linearly proportional with the size of the SAP particle:

$$\tau \propto l \Longrightarrow \tau = \frac{l}{a}, \tag{A.1}$$

where l is the size of the particle and $1/a$ is a proportionality constant. For the particles with size l_i the kinetics equation in saturated conditions becomes:

$$\frac{\partial m_{2_i}^s}{\partial t} = \frac{a}{l_i}\left(1 - \frac{m_{2_i}^s}{m_{2_{max}}^s}\right). \tag{A.2}$$

Considering $\mathrm{PDF}(l)$ the probability density function (PDF) of the particle size, the overall kinetics observed averaged among all the sizes is:

$$\frac{\partial m_2^s}{\partial t} = \int_0^{\rightarrow +\infty} \frac{\partial m_{2_i}^s}{\partial t} \mathrm{PDF}(l)\, dl = \int_0^{\rightarrow +\infty} \frac{a}{l_i}\left(1 - \frac{m_{2_i}^s}{m_{2_{max}}^s}\right) \mathrm{PDF}(l)\, dl. \tag{A.3}$$

For a single class of particle, it is possible to derive the swelling extent at any time:

$$m_{2_i}^s = 1 - \exp\left(-\frac{at/l_i}{m_{2_{max}}^s}\right). \tag{A.4}$$

Merging (A.3) and (A.4), the following expression for the swelling rate is obtained:

$$\frac{\partial m_2^s}{\partial t} = \int_0^{\rightarrow +\infty} \frac{a}{l} \exp\left(-\frac{at/l}{m_{2_{max}}^s}\right) \mathrm{PDF}(l)\, dl. \tag{A.5}$$

Integrating on time, the following expression represent the overall swelling degree with time:

$$m_2^s(t_f) = \int_0^{t_f} \int_0^{\to +\infty} \frac{a}{l} \exp\left(-\frac{at/l}{m_{2max}^s}\right) \mathrm{PDF}(l)\, dl\, dt. \tag{A.6}$$

Once the PDF of the size of the particles is known, (A.6) may be solved numerically, to estimate the overall kinetic reaction, in which the absorption characteristic time may be expressed as the following:

$$\tau = \frac{1}{a} \int_0^{\to +\infty} l\mathrm{PDF}(l)\, dl. \tag{A.7}$$

Then, the exponent of the kinetic equation (2.7) is the only parameter to be fitted with the experimental results. In this thesis, a noticeable agreement was found with a second-order kinetics, for all the investigated samples.

Equation (A.6) may be solved numerically, converting the integral in a summation:

$$m_2^s(t_f) = \sum_{i=0}^{f-1} (t_{i+1} - t_i) \int_0^{\to +\infty} \frac{a}{l} \exp\left(-\frac{at_i/l}{m_{2max}^s}\right) \mathrm{PDF}(l)\, dl. \tag{A.8}$$

APPENDIX B

THE DILATION FUNCTION

It is appropriate giving an insight on the dilation equation (2.9) presented in Chapter 2. Following the study of Diersch et al. (2010) [17], the balance of mass on the solid phase in an REV in the spatial frame is the following:

$$m^s = m^s_{FL} + m^s_{SAP} + m^s_2 m_{SAP}, \tag{B.1}$$

recalling the definition of m^s_2 given in Chapter 2. The volumes are additive as well and their balance is:

$$V^s = V^s_{FL} + V^s_{SAP} + m^s_2 \frac{m_{SAP}}{\rho^l}. \tag{B.2}$$

The bulk concentration of the components in the REV is simply the ratio of the quantities defined in (B.1) and (B.2). To pass from the reference (undeformed, initial) frame to the deformed one, or in other words, to pass from a material frame to a spatial frame, it is possible using the Jacobian as follows:

$$\bar{C}^s_i = \frac{1}{J^s} \bar{C}^s_{i\,0}, \tag{B.3}$$

where i indicates one of the three solid components, the subscript 0 is referred to the undeformed material frame and the dash upon the variable indicates bulk concentrations. Thus, it is possible to write in the spatial frame a general balance for the volume of the solid phase with variables defined in the material frame:

$$V^s = \frac{V}{J^s}\left[\frac{\bar{C}^s_{FL_0}}{\rho^s_{FL_0}} + \frac{\bar{C}^s_{SAP_0}}{\rho^s_{SAP_0}}\left(1 + m^s_2 \frac{\rho^s_{SAP_0}}{\rho^l}\right)\right]. \tag{B.4}$$

Considering that $V^s/V = 1 - \varepsilon$, we can derive:

$$J^s = \frac{1}{1-\varepsilon}\left[\frac{\bar{C}^s_{FL_0}}{\rho^s_{FL_0}} + \frac{\bar{C}^s_{SAP_0}}{\rho^s_{SAP_0}}\left(1 + m^s_2 \frac{\rho^s_{SAP_0}}{\rho^l}\right)\right]. \tag{B.5}$$

In a similar way, at the initial dry state, when no liquid is absorbed and $m^s_2 = 0$:

$$1-\varepsilon_0=\frac{\bar{C}^s_{FL_0}}{\rho^s_{FL_0}}+\frac{\bar{C}^s_{SAP_0}}{\rho^s_{SAP_0}}\,. \tag{B.6}$$

Merging the equations (B.5) and (B.6), it is possible to obtain the equation (2.9), here reported for the sake of clarity:

$$J^s=\frac{1}{1-\varepsilon}\left(1-\varepsilon_0+m^s_2\frac{\bar{C}^s_{SAP_0}}{\rho^l}\right). \tag{B.7}$$

APPENDIX C

FEATURES OF COMSOL®

Some of the technical aspects of the model implementation in COMSOL® software are hereafter described. For a further insight, the Reader is referred to COMSOL® Multiphysics Reference Manual [57].

i. TIME DEPENDENT BOUNDARY CONDITION

In order to avoid numerical issues, the pressure head on the wet boundary condition is set at the initial value of -1 m. On the contrary, the experimental method referred to in Chapter 3 describes a controlled imbibition, with a determined flow rate. Therefore, the pressure head on the boundary must immediately change its value from the initial pressure head of the entire domain to the ramp resembling the experimental imbibition. This is done introducing a step function for the first simulated second. Furthermore, the forming column of water resting on the sample is absorbed by it in the same time. The current height of the column, and so the pressure head on the boundary condition, can be expressed in the following form:

$$\psi^l_{bound_e}(t) = \psi^l_0 - \mathrm{step}(t)\left[\psi^l_0 - \psi^l_{bound}(t)\right], \tag{C.1}$$

where $\psi^l_{bound_e}(t)$ is the effective value of the pressure head on the wet boundary at any time during the imbibition phase, ψ^l_0 is the initial pressure head for the overall domain, $\mathrm{step}(t)$ is a step function that goes form 0 to 1 in 1 s and $\psi^l_{bound}(t)$ is the realistic height of the water column at any time. Moreover, the last term is calculated subtracting from the amount of water poured onto the sample the water inside the sample. While the first term of the subtraction is calculated with a ramp that mimics the experimental flow rate, the second one derives from an integral evaluation of water inside sample, both the liquid in the void space and the liquid absorbed by SAP, as expressed in the following:

$$\psi^l_{bound}(t) = \mathrm{ramp}(t)\psi^l_{bound_{max}} - \frac{1}{A_{bound}}\int_{\Omega^s}\left(\varepsilon s^l + m^s_2 \bar{C}^s_{SAP_0}/J^s \rho^l\right) d\Omega^s, \tag{C.2}$$

where $\mathrm{ramp}(t)$ is a ramp function in time, that linearly goes from 0 to 1 in the desired time interval, $\psi^l_{bound_{max}}$ is the theoretical maximum elevation of the column, considering the whole amount of water poured in the sample in a single imbibition, and A_{bound} is the area of the boundary.

On the other hand, during the drainage phases, a no-flux condition is imposed on the boundary:

$$\nabla\psi_{bound}^{l} = \mathbf{0}. \tag{C.3}$$

ii. THE MOVING MESH

The moving mesh in COMSOL® is handled through a specific module, the Moving Mesh Module (ALE, Arbitrary Lagrangian-Eulerian) [57]. In it, the spatial coordinate of the nodes of the mesh are treated as variables and evaluated together with all the other primary variables. Even though the displacement depends on variables that the model solves, if an expression is provided to describe the displacement, the evaluation does not contribute to the Jacobian matrix, which can cause convergence difficulties. The boundary conditions are expressed in terms of displacement or velocity for each direction.

iii. THE SOLVER

The solver may use two approaches to solve the nonlinear system of equations: the Fully Coupled and the Segregated approach. The Fully Coupled approach forms a single large system of equations that solve for all of the unknowns and includes all of the couplings between the unknowns at once, within a single iteration. On the other hand, the Segregated approach subdivides the problem up into two or more “Segregated Steps”, which are smaller than the full system of equations that are formed with the Fully Coupled approach. Each “Segregated Step” is solved sequentially within a single iteration, and thus less memory is required.

Regardless of the approach to solving nonlinear problems, the solution is approached by iteration. That is, the Fully Coupled or Segregated approach is called repeatedly, and gradually converges to the solution of the nonlinear problem. Since the Fully Coupled approach includes all coupling terms between the unknowns, it often converges more robustly and in less iterations as compared to the Segregated approach. However, each iteration will require relatively more memory and time to solve, so the Segregated approach can be faster overall.

For our purposes, the Segregated scheme was implemented, which is highly suggested for 3D models. In addition to the steps generated by default, another step was added to evaluate quantities relevant to the hysteretic model. At every iteration, the coefficients defined in (2.15) are evaluated from numerical results of the previous step. Once defined the coefficients for the first step ($c_d = 0$ and $c_w = 1$ for an initially dry sample), the others are then evaluated from the solved fields at every time step.

Finally, a stop condition was added to the solver, to change the boundary condition from a Dirichlet type (wet boundary) to a Neumann type (no-flux boundary). The stop condition acts due to a triggering event. In this case the event is the achieving of the amount of water poured into to the sample, evaluated from an integral calculation on the whole domain.

APPENDIX D

THE DEM IN YADE

Here, the main features of the DEM algorithm of the open-source software YADE exploited for the simulations in Chapter 5 are explained. An accurate description of the whole software, from the coding to the post-processing of the results, is available on the website reported in the References [61].

The particles are treated as soft spheres. A contact is defined as an overlapping of domains between particles. When contacts occur, the particles may deform at the contact point. The local deformation is assumed to be linearly elastic. For the contact of two different particles i and j, the effective properties of the contact mechanism are evaluated: effective Young's modulus $E_{ij} = \left(\frac{1-\nu_i^2}{E_i} + \frac{1-\nu_i^2}{E_j}\right)^{-1}$, the harmonic mean of particle radii $r_{ij} = \frac{r_i r_j}{r_i + r_j}$, the average shear modulus $G_{ij} = \frac{G_i + G_j}{2}$ and the average Poisson ratio $\nu_{ij} = \frac{\nu_i + \nu_j}{2}$.

The detection of the impacts is done through the "sweep and prune" method. This algorithm operates on axis-aligned bounding boxes, which overlap if and only if they overlap along all axes. The "sweep and prune" have roughly $O(n \log n)$ complexity, where n is number of particles [61].

An upper limit to the size of the time step is imposed, to ensure numerical stability. The displacement of the particles during one step is reduced due to this limitation. This constraint avoids the particles to move further than the neighbouring grid cell during one step.

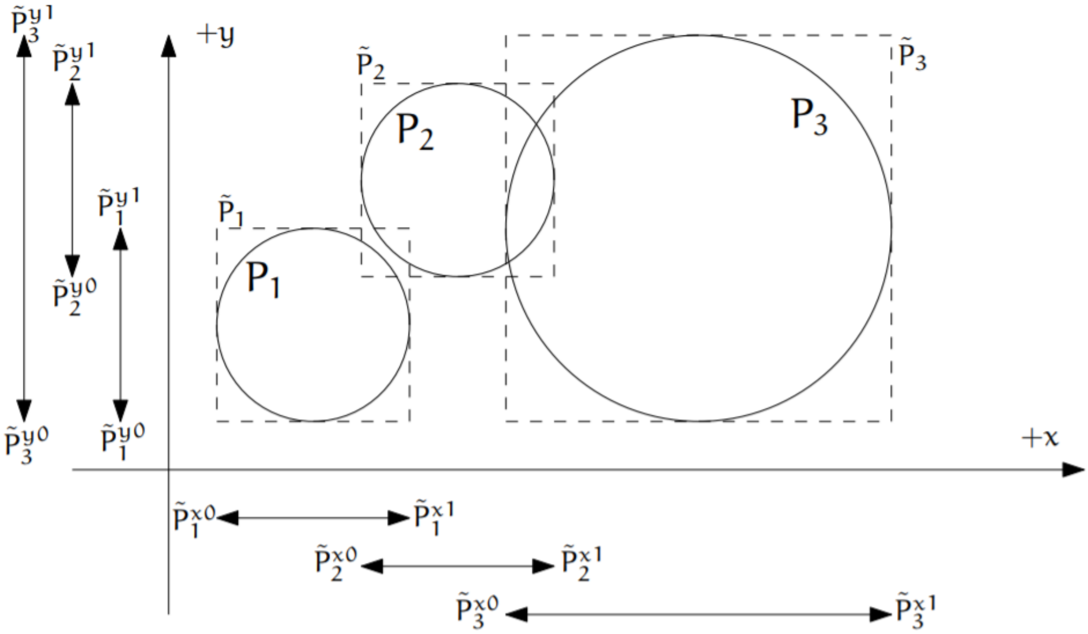

Figure D-0.1. Sweep and prune algorithm, shown in 2D. Despite the intersection of the bounding box around particles, only the second and the third particles are in contact. Image from Šmilauer and Chareyre (2015) [61].

A collision between particles is defined as an overlapping of their domains. In order to simplify the detection of collision, the software first looks for overlapping of bounding boxes, as it is shown in Figure D-1. Only the particles belonging to overlapping bounding box are further considered for the next steps, in which the collisions are finally detected.

Once the objects involved in collisions are sorted through geometric evaluations, it is necessary to determine the forces acting on them, introducing physical properties related to their constituent materials. The evaluation of forces occurs at each time step, and the acceleration of the particles is then calculated. Two general interactions are considered: normal and shear (tangent) interactions. Commonly, in DEM algorithms this is handled through the introduction of a normal and a shear stiffness. The normal force is then calculated as:

$$f_{ij}^{n} = -k_{ij}^{n}\left(\delta_{ij}^{n}\right)^{\frac{3}{2}}, \tag{D.1}$$

$$k_{ij}^{n} = \frac{4}{3} E_{ij}\sqrt{r_{ij}}, \tag{D.2}$$

where k_{ij}^{n} is the contact stiffness in the normal direction and δ_{ij}^{n} is the displacement due to the deformation. In the tangential direction, the elastic force at a given time step, $\left(\boldsymbol{f}_{\boldsymbol{ij}}^{\boldsymbol{t}}\right)^{t+\Delta t}$**,** depends on its old value and the current relative tangential velocity:

$$\left(\boldsymbol{f}_{\boldsymbol{ij}}^{\boldsymbol{t}}\right)^{t+\Delta t} = \left(\boldsymbol{f}_{\boldsymbol{ij}}^{\boldsymbol{t}}\right)^{t} + k_{ij}^{t}\dot{\boldsymbol{d}}_{\boldsymbol{ij}}^{\boldsymbol{t}}\Delta t, \tag{D.3}$$

in which $\dot{\boldsymbol{d}}_{\boldsymbol{ij}}^{\boldsymbol{t}}$ is the relative tangential velocity. The contact stiffness in tangential direction has the following expression:

$$k_{ij}^{t} = \frac{4\sqrt{r_{ij}}G_{ij}}{2-\nu_{ij}}\left(\delta_{ij}^{n}\right)^{0.5}. \tag{D.4}$$

Particle sliding may occur if the tangential force surpasses a threshold value, usually related to the friction angle (ϕ_{fr}):

$$\left\|\boldsymbol{f}_{\boldsymbol{ij}}^{\boldsymbol{t}}\right\| < f_{ij}^{n} \tan \phi_{fr}. \tag{D.5}$$

Once the forces are determined, the software evaluate the acceleration of each particle and move the particle in the time step accordingly. After the motion of the particles, a new maximum time step is estimated, and the algorithm is repeated. In Figure D-2 is summarized the just described algorithm.

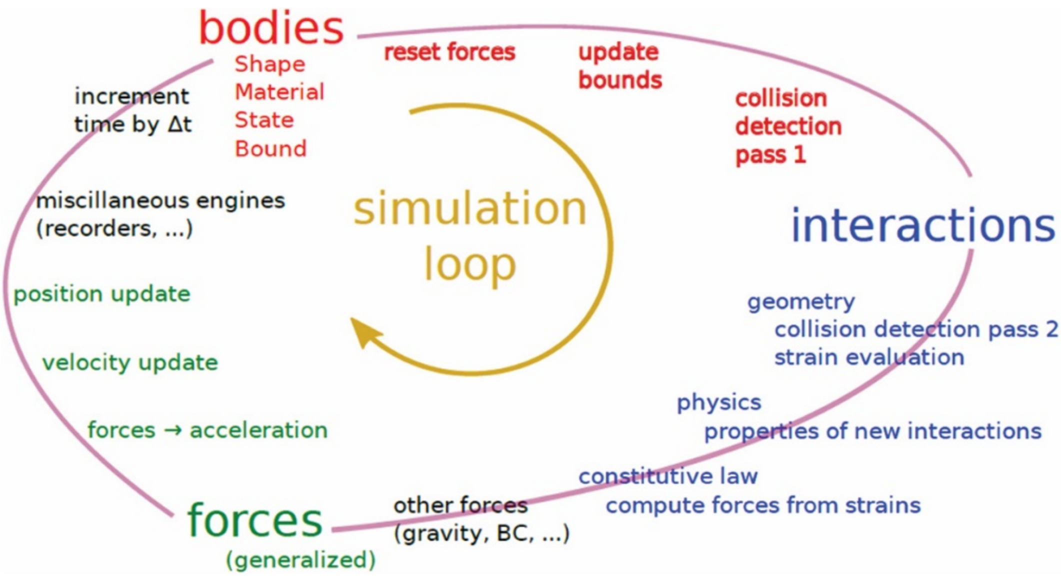

Figure D-0.2. A schematic description of the simulation loop of YADE-DEM open-source software. The image is taken from [61].

In the description of the simulation scheme in Chapter 5, the denomination "unbalanced force" has been used. This is the ratio of maximum contact force and maximum per-body force, or the average of the body forces divided per the average of the contact forces. This is a measure of stability and it is computed through a specific module of the software.

REFERENCES

[1] H.P.G. Darcy, Les Fontaines publiques de la ville de Dijon. Exposition et application des principes à suivre et des formules à employer dans les questions de distribution d'eau, etc, V. Dalamont, 1856.

[2] W.G. Gray, C.T. Miller, Introduction to the thermodynamically constrained averaging theory for porous medium systems, Springer, 2014.

[3] J. Bear, Dynamics of fluids in porous media, Courier Corporation, 2013.

[4] R. Masoodi, K.M. Pillai, Wicking in porous materials: traditional and modern modeling approaches, 1st ed., CRC Press, Boca Raton, 2012.

[5] G.A. Narsilio, O. Buzzi, S. Fityus, T.S. Yun, D.W. Smith, Upscaling of Navier–Stokes equations in porous media: Theoretical, numerical and experimental approach, Comput. Geotech. 36 (2009) 1200–1206. https://doi.org/10.1016/J.COMPGEO.2009.05.006.

[6] V. Joekar-Niasar, S.M. Hassanizadeh, Pore-Network Modeling of Wicking: A Two-Phase Flow Approach, in: R. Masoodi, K.M. Pillai (Eds.), Wicking Porous Mater. Tradit. Mod. Model. Approaches, CRC Press, 2013: pp. 237–262.

[7] M.G. Schaap, M.L. Porter, Simulating Fluid Wicking into Porous Media with the Lattice Boltzmann Method, in: R. Masoodi, K.M. Pillai (Eds.), Wicking Porous Mater. Tradit. Mod. Model. Approaches, CRC Press, 2013: pp. 327–353.

[8] H.-J. Vogel, J. Tölke, V.P. Schulz, M. Krafczyk, K. Roth, Comparison of a lattice-Boltzmann model, a full-morphology model, and a pore network model for determining capillary pressure–saturation relationships, Vadose Zo. J. 4 (2005) 380–388.

[9] T. Sweijen, H. Aslannejad, S.M. Hassanizadeh, Capillary pressure–saturation relationships for porous granular materials: Pore morphology method vs. pore unit assembly method, Adv. Water Resour. 107 (2017) 22–31. https://doi.org/10.1016/j.advwatres.2017.06.001.

[10] M.J. Zohuriaan-Mehr, K. Kabiri, Superabsorbent polymer materials: a review, Iran. Polym. J. 17 (2008) 451.

[11] J.M. Huyghe, J.D. Janssen, Quadriphasic mechanics of swelling incompressible porous media, Int. J. Eng. Sci. 35 (1997) 793–802. https://doi.org/10.1016/S0020-7225(96)00119-X.

[12] F.L. Buchholz, A.T. Graham, Modern superabsorbent polymer technology, 1st ed., Wiley-VCH, New York, 1997.

[13] A. Knaebel, S.R. Rebre, F. Lequeux, Determination of the elastic modulus of superabsorbent gel beads, Polym. Gels Networks. 5 (1997) 107–121. https://doi.org/10.1016/S0966-7822(96)00034-2.

[14] K. Kabiri, H. Omidian, S.A. Hashemi, M.J. Zohuriaan-Mehr, Synthesis of fast-swelling superabsorbent hydrogels: effect of crosslinker type and concentration on porosity and absorption rate, Eur. Polym. J. 39 (2003) 1341–1348. https://doi.org/10.1016/S0014-3057(02)00391-9.

[15] H. Omidian, S.A. Hashemi, P.G. Sammes, I. Meldrum, A model for the swelling of superabsorbent polymers, Polymer (Guildf). 39 (1998) 6697–6704. https://doi.org/10.1016/S0032-3861(98)00095-0.

[16] L.P. Esteves, Superabsorbent polymers: On their interaction with water and pore fluid, Cem. Concr. Compos. 33 (2011) 717–724. https://doi.org/10.1016/J.CEMCONCOMP.2011.04.006.

[17] H.-J.G. Diersch, V. Clausnitzer, V. Myrnyy, R. Rosati, M. Schmidt, H. Beruda, B.J. Ehrnsperger, R. Virgilio, Modeling Unsaturated Flow in Absorbent Swelling Porous Media: Part 1. Theory, Transp. Porous Media. 83 (2010) 437–464. https://doi.org/10.1007/s11242-009-9454-6.

[18] T. Sweijen, E. Nikooee, S.M. Hassanizadeh, B. Chareyre, The Effects of Swelling and Porosity Change on Capillarity: DEM Coupled with a Pore-Unit Assembly Method, Transp. Porous Media. 113 (2016) 207–226. https://doi.org/10.1007/s11242-016-0689-8.

[19] T. Sweijen, C.J. van Duijn, S.M. Hassanizadeh, A model for diffusion of water into a swelling particle with a free boundary: Application to a super absorbent polymer particle, Chem. Eng. Sci. 172 (2017) 407–413. https://doi.org/10.1016/j.ces.2017.06.045.

[20] T. Sweijen, B. Chareyre, S.M. Hassanizadeh, N.K. Karadimitriou, Grain-scale modelling of swelling granular materials; application to super absorbent polymers, Powder Technol. 318 (2017) 411–422. https://doi.org/10.1016/j.powtec.2017.06.015.

[21] P.A. Cundall, O.D.L. Strack, A discrete numerical model for granular assemblies, Geotechnique. 29 (1979) 47–65.

[22] C.F. Dahl, Process of manufactoring cellulose from wood, US296935A, 1884.

[23] S. Heyden, Network Modelling for the Evaluation of Mechanical Properties of Cellulose Fluff, 2000.

[24] C. Hirsch, Numerical computation of internal and external flows: The fundamentals of computational fluid dynamics, Elsevier, 2007.

[25] H.-J.G. Diersch, P. Perrochet, On the primary variable switching technique for simulating unsaturated–saturated flows, Adv. Water Resour. 23 (1999) 271–301. https://doi.org/10.1016/S0309-1708(98)00057-8.

[26] M.A. Celia, P.C. Reeves, L.A. Ferrand, Recent advances in pore scale models for multiphase flow in porous media, Rev. Geophys. 33 (1995) 1049–1057. https://doi.org/10.1029/95RG00248.

[27] M.A. Tahir, H. Vahedi Tafreshi, Influence of fiber orientation on the transverse permeability of fibrous media, Phys. Fluids. 21 (2009) 083604. https://doi.org/10.1063/1.3211192.

[28] A. Ashari, H. Vahedi Tafreshi, A two-scale modeling of motion-induced fluid release from thin fibrous porous media, Chem. Eng. Sci. 64 (2009) 2067–2075. https://doi.org/10.1016/j.ces.2009.01.048.

[29] A. Ashari, H. Vahedi Tafreshi, General capillary pressure and relative permeability expressions for through-plane fluid transport in thin fibrous sheets, Colloids Surfaces A Physicochem. Eng. Asp. 346 (2009) 114–122. https://doi.org/10.1016/J.COLSURFA.2009.06.001.

[30] A. Ashari, T.M. Bucher, H. Vahedi Tafreshi, M.A. Tahir, M.S.A. Rahman, Modeling fluid spread in thin fibrous sheets: Effects of fiber orientation, Int. J. Heat Mass Transf. 53 (2010) 1750–1758. https://doi.org/10.1016/J.IJHEATMASSTRANSFER.2010.01.015.

[31] H. Aslannejad, S.M. Hassanizadeh, Study of Hydraulic Properties of Uncoated Paper: Image Analysis and Pore-Scale Modeling, Transp. Porous Media. (2017). https://doi.org/10.1007/s11242-017-0909-x.

[32] M.A.F. Zarandi, K.M. Pillai, A.S. Kimmel, Spontaneous imbibition of liquids in glass-fiber wicks. Part I: Usefulness of a sharp-front approach, AIChE J. 64 (2018) 294–305. https://doi.org/10.1002/aic.15965.

[33] M.A. F. Zarandi, K.M. Pillai, Spontaneous imbibition of liquid in glass fiber wicks, Part II: Validation of a diffuse-front model, AIChE J. 64 (2018) 306–315. https://doi.org/10.1002/aic.15856.

[34] M. Landeryou, I. Eames, A. Cottenden, Infiltration into inclined fibrous sheets, J. Fluid Mech. 529 (2005) 173–193. https://doi.org/10.1017/S0022112005003356.

[35] A.H. Tavangarrad, B. Mohebbi, S.M. Hassanizadeh, R. Rosati, J. Claussen, B. Blümich, Continuum-Scale Modeling of Liquid Redistribution in a Stack of Thin Hydrophilic Fibrous Layers, Transp. Porous Media. 122 (2018) 203–219. https://doi.org/10.1007/s11242-018-0999-0.

[36] D.S. Clague, R.J. Phillips, A numerical calculation of the hydraulic permeability of three-dimensional disordered fibrous media, Phys. Fluids. 9 (1997) 1562–1572. https://doi.org/10.1063/1.869278.

[37] C. Qin, S.M. Hassanizadeh, Multiphase flow through multilayers of thin porous media: General balance equations and constitutive relationships for a solid–gas–liquid three-phase system, Int. J. Heat Mass Transf. 70 (2014) 693–708. https://doi.org/10.1016/J.IJHEATMASSTRANSFER.2013.11.059.

[38] C. Qin, S.M. Hassanizadeh, A new approach to modelling water flooding in a polymer electrolyte fuel cell, Int. J. Hydrogen Energy. 40 (2015) 3348–3358. https://doi.org/10.1016/J.IJHYDENE.2015.01.035.

[39] R. Masoodi, K.M. Pillai, Single-phase flow (sharp-interface) models for wicking, Wicking Porous Mater. Tradit. Mod. Model. Approaches. (2012) 97–130.

[40] R. Lenormand, E. Touboul, C. Zarcone, Numerical models and experiments on immiscible displacements in porous media, J. Fluid Mech. 189 (1988) 165–187. https://doi.org/10.1017/S0022112088000953.

[41] T. Sweijen, A grain-scale study of unsaturated flow in highly swelling granular materials, Universiteit Utrecht, 2017. https://dspace.library.uu.nl/bitstream/handle/1874/356767/Sweijen.pdf?sequence=1&isAllowed=y.

[42] D. Kunhappan, B. Harthong, B. Chareyre, G. Balarac, P.J.J. Dumont, Numerical modeling of high aspect ratio flexible fibers in inertial flows, Phys. Fluids. 29 (2017) 093302. https://doi.org/10.1063/1.5001514.

[43] H.-J.G. Diersch, V. Clausnitzer, V. Myrnyy, R. Rosati, M. Schmidt, H. Beruda, B.J. Ehrnsperger, R. Virgilio, Modeling Unsaturated Flow in Absorbent Swelling Porous Media: Part 2. Numerical Simulation, Transp. Porous Media. 86 (2011) 753–776. https://doi.org/10.1007/s11242-010-

9650-4.

[44] H.-J.G. Diersch, FEFLOW finite element subsurface flow and transport simulation system, Inst. Water Resour. Plan. Syst. Res., Berlin. (2005).

[45] E. Nikooee, T. Sweijen, S.M. Hassanizadeh, Determination of the relationship among capillary pressure, saturation and interfacial area: a pore unit assembly approach, E3S Web Conf. 9 (2016) 02002. https://doi.org/10.1051/e3sconf/20160902002.

[46] O. Coussy, Mechanics of porous continua, Wiley, 1995.

[47] O. Sohn, D. Kim, Theoretical and experimental investigation of the swelling behavior of sodium polyacrylate superabsorbent particles, J. Appl. Polym. Sci. 87 (2003) 252–257. https://doi.org/10.1002/app.11360.

[48] M.T. van Genuchten, A closed-form equation for predicting the hydraulic conductivity of unsaturated soils, Soil Sci. Soc. Am. J. 44 (1980) 892–898.

[49] K.M. Pillai, K. Hooman, An introduction to modeling flows in porous media, in: R. Masoodi, K.M. Pillai (Eds.), Wicking Porous Mater. Tradit. Mod. Model. Approaches, 2012: pp. 55–96.

[50] M.T. van Genuchten, P.J. Wierenga, Mass transfer studies in sorbing porous media I. Analytical solutions, Soil Sci. Soc. Am. J. 40 (1976) 473–480.

[51] R.H. Brooks, A.T. Corey, Properties of porous media affecting fluid flow, J. Irrig. Drain. Div. 92 (1966) 61–90.

[52] F. Lomeland, E. Ebeltoft, W.H. Thomas, A new versatile relative permeability correlation, in: Int. Symp. Soc. Core Anal. Toronto, Canada, 2005.

[53] H.V. Tafreshi, T.M. Bucher, Modeling fluid absorption in anisotropic fibrous porous media, in: Wicking Porous Mater., Boca Raton: CRC Press, 2013: pp. 131–159.

[54] U. Hirn, R. Schennach, Comprehensive analysis of individual pulp fiber bonds quantifies the mechanisms of fiber bonding in paper, Sci. Rep. 5 (2015) 10503. https://doi.org/10.1038/srep10503.

[55] F.L. Buchholz, S.R. Pesce, C.L. Powell, Deswelling stresses and reduced swelling of superabsorbent polymer in composites of fiber and superabsorbent polymers, J. Appl. Polym. Sci. 98 (2005) 2493–2507. https://doi.org/10.1002/app.21963.

[56] J. Bae, H. Kwon, J. Kim, Safety Evaluation of Absorbent Hygiene Pads: A Review on Assessment Framework and Test Methods, Sustainability. 10 (2018) 4146. https://doi.org/10.3390/su10114146.

[57] COMSOL Multiphysics Reference Manual, version 5.3, (2018). www.comsol.com.

[58] H.-J.G. Diersch, P. Perrochet, On the primary variable swiching technique for simulating unsatured-satured flows, Adv. Water Resour. 23; 23 (1999) 271–301.

[59] D. Stauffer, A. Aharony, Introduction to percolation theory, Taylor & Francis, 2018.

[60] D.T. Hristopulos, Renormalization group methods in subsurface hydrology: overview and applications in hydraulic conductivity upscaling, Adv. Water Resour. 26 (2003) 1279–1308. https://doi.org/10.1016/S0309-1708(03)00103-9.

[61] V. Šmilauer, B. Chareyre, DEM Formulation, in: Yade Doc. 2nd Ed., 2015. https://doi.org/10.5281/zenodo.34044.